ANALYTICAL AND EXPERIMENTAL STUDY OF THE EFFECTS OF WING-BODY AERODYNAMIC INTERACTION ON SPACE SHUTTLE SUBSONIC FLUTTER

Richard R. Chipman and Frank J. Rauch

Prepared by
GRUMMAN AEROSPACE CORPORATION
Bethpage, N.Y. 11714
for Langley Research Center

NATIONAL AERONAUTICS AND SPACE ADMINISTRATION • WASHINGTON, D. C. • JANUARY 1975

1. Report No. NASA CR-2488	2. Government Accession No.	3. Recipient's Catalog No.
4. Title and Subtitle ANALYTICAL AND EXPERIMENTAL STUDY OF THE EFFECTS OF WING-BODY AERODYNAMIC INTER-ACTION ON SPACE SHUTTLE SUBSONIC FLUTTER		5. Report Date JANUARY 1975
		6. Performing Organization Code
7. Author(s) Richard R. Chipman and Frank J. Rauch		8. Performing Organization Report No.
9. Performing Organization Name and Address Grumman Aerospace Corporation Bethpage, NY 11714		10. Work Unit No. 506-17-32-03
		11. Contract or Grant No. NAS1-10635-18
12. Sponsoring Agency Name and Address National Aeronautics and Space Administration Washington, D.C. 20546		13. Type of Report and Period Covered Contractor Report
		14. Sponsoring Agency Code

15. Supplementary Notes

Final report.

16. Abstract

 To determine the effect on flutter of the aerodynamic interaction between the Space Shuttle bodies and wing, 1/80th-scale semispan models of the orbiter wing, the complete Shuttle and intermediate component combinations were tested in the NASA Langley Research Center 26-inch Transonic Blowdown Wind Tunnel. Using the doublet-lattice method combined with slender body theory to calculate unsteady aerodynamic forces, subsonic flutter speeds were computed for comparison.

 Using calculated complete-vehicle modes, flutter-speed trends were computed for the full-scale vehicle at an altitude of 15,200 meters and a Mach number of 0.6. Consistent with findings of the model studies, analysis showed the Shuttle to have the same flut-flutter speed as an isolated cantilevered wing.

17. Key Words (Suggested by Author(s)) Space Shuttle Flutter Calculated Subsonic Flutter Speeds Calculated Full-scale Flutter Spds 1/80-scale Semispan Model	18. Distribution Statement Unclassified - Unlimited STAR Category 32
19. Security Classif. (of this report) Unclassified	20. Security Classif. (of this page) Unclassified	21. No. of Pages 73	22. Price* $4.25

*For sale by the National Technical Information Service, Springfield, Virginia 22151

ANALYTICAL AND EXPERIMENTAL STUDY OF THE EFFECTS.
OF WING-BODY AERODYNAMIC INTERACTION ON
SPACE SHUTTLE SUBSONIC FLUTTER

By Richard R. Chipman and Frank J. Rauch

SUMMARY

To determine the effect on flutter of the aerodynamic interaction be-
tween the Space Shuttle bodies and wing, 1/80th-scale semispan models of the
orbiter wing, the complete Shuttle and intermediate component combinations
were tested in the NASA Langley Research Center 26-inch Transonic Blowdown Wind
Tunnel. Using the doublet-lattice method combined with slender body theory to
calculate unsteady aerodynamic forces, subsonic flutter speeds were computed
for comparison.

Aerodynamic interaction was found by test and analysis to raise the
flutter speed in some configurations while lowering it in others, such that
the flutter speed of the complete Shuttle at M = 0.7 was the same as that of a
cantilevered isolated wing. Although at Mach numbers not greater than 0.7, pre-
dicted speeds correlated to within 6% of those measured, rapid deterioration
of the agreement occurred at higher subsonic Mach numbers, especially on the
more complicated configurations. Steady-state pressure distributions were also
measured and computed, revealing similar trends.

Using calculated complete-vehicle modes, flutter-speed trends were com-
puted for the full-scale vehicle at an altitude of 15,200 meters and a Mach
number of 0.6. Consistent with findings of the model studies, analysis showed
the Shuttle to have the same flutter speed as an isolated cantilevered wing.

INTRODUCTION

The flutter characteristics of an aircraft component can be affected
by aerodynamic interaction between it and other proximate components. Classic
examples, when both components are lifting surfaces, are T-tail flutter
(Ref. 1) and wing-tail flutter (Ref. 2). To predict subsonic aerodynamic
forces arising in such configurations, the kernel-function method of Watkins
(Ref. 3) and the doublet-lattice method of Rodden (Ref. 4) and of Stark (Ref. 5)

were developed and extended to handle multiple planar and nonplanar surfaces. The success obtained in applying these theories to wing-tail configurations is recorded by Sensburg (Ref. 6), Mykytow (Ref. 7), and Triplett (Ref. 8). Similarly, Chipman used the doublet-lattice flutter analysis method to correlate successfully with wind tunnel data for pairs of closely spaced wings such as might be found on the fly-back-booster Space Shuttle configurations (Ref. 9).

The aerodynamic forces arising from the interaction between bodies and lifting surfaces can also be significant. In the steady-state case, methods for computing these forces were developed by Woodward (Ref. 10) and Hess (Ref. 11). Rodden and Giesing (Ref. 12) have combined slender-body theory with the doublet-lattice method to solve the unsteady problem in subsonic flow.

The current Space Shuttle concept features four large, flexible bodies: the orbiter fuselage, the external tank (ET), and the two solid-rocket boosters (SRB's). The proximity of these bodies to the orbiter wing admits the possibility of a change in vehicle flutter boundary as a result of aerodynamic interaction. Consequently, a two-phase study was initiated to obtain analytical and experimental confirmation of this contention. Reference 13 reports the first phase of this work: A preliminary design - the Grumman G III - of the parallel-burn, Space Shuttle concept was analyzed using Rodden's method (Ref. 12) to determine the anticipated effect of wing-body aerodynamic interaction on flutter. This report describes the second phase: Comparisons of experimentally and analytically determined wing-body interaction flutter effects are made subsonically for a model of a recent design to assess the applicability of Rodden's method to the Space Shuttle.

In the present study, 1/80th-scale semispan models of the Shuttle were tested for flutter in the Mach number range 0.6 to 1.4. Additionally, steady-state pressures were measured on the wing. Results were correlated with flutter speeds and pressures predicted using Rodden's doublet-lattice/interaction-panel method. Various combinations of vehicle components - wing alone; wing and orbiter fuselage; wing, fuselage and external tank; and complete Shuttle - were studied.

Because the analyses of Phase I indicated that forces arising from body flexibility did not appreciably alter the Space Shuttle flutter speed, the model bodies in the present investigation were designed to be rigid. Except for two configurations in which flexible SRB attachments were used, only the wing was flexible.

A final check of interaction flutter effects on the current Shuttle was made by calculating flutter speeds using calculated full-scale vehicle modes which included flexibility on all the bodies.

b_r	Reference semichord = 0.0572 m
c	Local chord
C_L	Lift coefficient
C_{L_α}	Life curve slope
C_{M_α}	Moment curve slope
C_P	Pressure coefficient
ΔC_P	Coefficient of the net pressure difference across a surface or body
$\left\{ \Delta C_{P,B} \right\}$	Net pressure coefficient distribution on the slender body elements
$\left\{ \Delta C_{P,I} \right\}$	Net pressure coefficient distribution on the interaction panels
$\left\{ \Delta C_{P,W} \right\}$	Net pressure coefficient distribution on the wing panels
$\left[D_{II} \right]$	Downwash on the interaction panel collocation points caused by unit pressures on the interaction panels
$\left[D_{IW} \right]$	Downwash on the interaction panel collocation points caused by unit pressures on the wing panels
$\left[D_{WI} \right]$	Downwash on the wing collocation points caused by unit pressures on the interaction panels
$\left[D_{WW} \right]$	Downwash on the wing collocation points caused by unit pressures on the wing panels
ET	External tank
f	Frequency
$\left[F_{I,B} \right]$	Downwash on the interaction panel collocation points due to unit pressures on the slender body elements
$\left[F_{W,B} \right]$	Downwash on the wing collocation points due to unit pressures on the slender body elements

h   Modal deflection

k   Reduced frequency $= b\omega/U_\infty$

M   Mach number

m_W Mass of exposed wing $= 0.0525$ kg

q   Dynamic pressure

R_O Slender body radius

s   Exposed semispan

SRB   Solid rocket booster

U_∞ Free stream velocity

V_f Flutter speed

v_W Volume of frustum of a cone encompassing the exposed wing $= 0.00133$ m^3

V-g-f   Velocity-damping-frequency

$\{W_I\}$ Prescribed downwash at the interaction panel collocation points

$\{W_W\}$ Prescribed downwash at the wing collocation points

x   Streamwise coordinate

Δx Distance that the center pressure lies aft of the local leading edge

y   Spanwise coordinate

z   Vertical coordinate

α Angle of attack or incidence

α_B Body incidence

α_W Wing incidence

σ Ratio of air density in tunnel to that at sea level

μ Mass density ratio $= \dfrac{m_W}{\rho_{SL} v_W}$

ρ_{SL} Density of air at sea level

ω Circular frequency

ω_r Reference frequency $= 470$ Hz

$(\;)'$ Derivative in x direction

$(\;)''$ Second derivative in x direction

TEST APPARATUS

Models

Semispan models of the current Shuttle design shown in Figure 1 were built for flutter testing. They consisted of rigid fairing replicas of the orbiter half-fuselage, the half external-tank (ET), and the solid rocket booster (SRB) in proper proximity to a flexible orbiter wing. As can be seen in Figure 2, the wing is a double delta with an inner-panel leading-edge sweep of 79°, an outer-panel sweep of 45°, and an aspect ratio of 2.1. The crank in the leading edge occurs at a station 25% of the distance from the root to the tip. The wing model consisted of aluminum spanwise-tapered core plates with cutouts, designed to match the torsion-to-bending frequency ratio of the full-scale wing.

Figure 3 shows the wing in various stages of assembly. On the core, balsa wood was affixed and shaved to a 12% maximum thickness airfoil shape representative of the Shuttle. Wing camber and twist were not modelled; the model section was made symmetrical. To eliminate structural coupling, the rigid geometrically scaled fairings representing the fuselage, ET, and SRB components were fastened rigidly to a splitter plate located at the mid-vehicle plane. This assembly is shown in Figure 4. A second splitter plate was made which could be located at the wing root when the body fairings were removed to study flutter of the isolated wing end-plated at its root.

Two sets of flexible connectors were fabricated, each of which could be substituted for the rigid fasteners linking the SRB to the ET. With these flexures, SRB pitch and heave modes could be attained. One of the sets was

designed such that the frequencies of these modes in model scale were equal to those of SRB pitch and vertical bending of the nominal Shuttle design. With the second set, the frequencies were chosen to be closer to wing torsion so that the likelihood of interaction would be greater. Table I summarizes the frequencies of these and the primary wing modes.

A rigid wing with 38 pressure taps was constructed to measure steady-state pressures. Provisions were made on the mounting plate to pitch each configuration either 0° of -3°. With pressure data from each of these two angles of attack, the primary effects of wing thickness could be removed by subtraction of the two pressure distributions.

Instrumentation on Models

Each flexible wing was instrumented with strain gages which, through their response to bending and torsional motions, were used to detect the onset of flutter and to measure flutter frequency. Additional gages were mounted on the SRB flexures to detect SRB excitation.

The pressure taps of the rigid pressure wing were connected to transducers that measured the difference between the manifold pressure and the pressure on the wing surface.

Wind Tunnel

Flutter and pressure tests were conducted in the NASA Langley Research Center 26-inch Transonic Blowdown Wind Tunnel for a Mach number range of 0.6 to 1.4. During the flutter runs, an oscillograph was used to record the following items:

- Output of model strain gage and magnetic coil circuits
- Total test section pressure (P_o)
- Settling chamber temperature (T_o)
- Static test section pressure (P_s)
- Reference trace used in determining P_o, P_s and T_o trace deflection
- Movie camera correlation trace.

A high speed movie camera was used to obtain a visual record of model behavior during each flutter run.

6

For each pressure run, the following information was placed on magnetic tape:

- Output of pressure gage circuits that record wing pressure data
- Total test section pressure (P_O)
- Static test section pressure (P_S)
- Temperature (T_O)
- Manifold pressure (P_M).

TEST PROCEDURES AND DATA REDUCTION

Vibration Survey

Prior to wind-tunnel testing, each wing model was subjected to a vibration survey. Modal shapes, frequencies and damping coefficients were determined for one model, and the subsequent models were checked for likeness of frequencies and damping coefficients. Noncontacting excitation and measurement systems were utilized to assure distortion-free mode shapes and frequencies. The output of a noncontacting inductance-type pickup was conditioned, and displayed on a vacuum tube voltmeter and oscillograph to extract mode shapes and damping data. During the survey, the models were rigidly clamped at the root to simulate the tunnel installation.

Shown in Figure 5 are the locations of the concentrated mass points and the points at which the modal data were measured. Table II gives the coordinates of these points and the calculated masses. Figure 6 presents the measured mode shape data in tabular and graphic form.

Similarly, for each set of flexible attachments, modal data were measured on the SRB for the two lowest frequency modes. These modes are presented in Figure 7. Because of the inherent flexibility of the SRB model, the modes include a significant amount of bending as well as the intended pitching and heaving motions. The frequencies of these and the measured wing modes are summarized in Table I.

Flutter Tests

Before each tunnel run, the models to be used were visually examined for signs of damage due to previous runs. In addition, after being installed in the tunnel, the wing model was excited, and oscilloscograph records of the strain gage outputs were monitored to check frequencies and dampings of the first four modes.

On the basis of the results of previous runs, a desired tunnel operating "path" was selected for the run. This path was followed until either the tunnel air supply was exhausted or flutter was detected visually. Several runs following different paths were made on each configuration to determine a boundary of flutter speed vs Mach number.

As shown in Table III, flutter boundaries were determined for six configurations: the isolated wing endplated at its root, the orbiter (wing and fuselage), the orbiter and external tank, the full-up Shuttle (orbiter, tank and SRB) with rigid interstage attachments, the full-up Shuttle with the nominal flexible attachments and the full-up Shuttle with a second set of flexible attachments.

Flutter points were initially determined from the oscillograph records and visual observations during the run, and then either confirmed or adjusted by subsequent examination of the movie data. The flutter point was taken as the point during the run where the model circuit traces indicated a frequency regularity and/or significant increase in the model vibrational amplitude. Tunnel data converted to the parameters Mach number, air density ratio, and dynamic pressures are presented in Table IV.

For each flutter point (or significant stable point), the Mach number and dynamic pressure are presented in Figure 8. In addition to the data presented in Table IV, several non-flutter points during each run were studied to determine the tunnel path taken. These paths are plotted in Figure 8 and help define the suggested flutter boundaries indicated.

Pressure Tests

After the rigid pressure wing was installed in the wind tunnel together with appropriate body models, the pressure lines were connected to transducers and calibration was performed.

During each run, the tunnel was programmed to quickly attain a pre-chosen combination of Mach number and dynamic pressure. So that the flow would have time to stabilize, this point was maintained for 3 seconds before any data were collected. Pressure was sampled five times at each orifice and then a constant Mach number path was followed to a second, higher dynamic pressure at which the pause and sampling were repeated. The data were stored on magnetic tape and later reduced by digital computer.

For each of the three configurations noted in Table III, pressure measurements were made at $M = 0.6, 0.8, 1.0$ and 1.2, once for the vehicle at an angle of attack equal to 0° and once for the vehicle at a -3° angle of attack. The data were automatically plotted as chordwise distributions of C_p at both the upper and lower surfaces at each of the four spanwise stations, $y/s = 0.1, 0.4, 0.7$ and 0.9. Only the subsonic data were further reduced and studied for this report.

After inspecting the data and eliminating points where gages were either clogged, damaged, or otherwise unreliable, it was determined that data on the outer portion of the upper wing surface were largely unusable but that the lower surface data were acceptable at most locations.

To determine a pressure difference across the wing due to the angle of attack, one would normally subtract the lower surface pressure from the upper surface pressure measured at the angle of attack, and from this increment subtract a similar increment measured at zero incidence. This computation can be expressed:

$$\Delta C_p (\alpha) = (C_{p,u}(\alpha) - C_{p,\ell}(\alpha)) - (C_{p,u}(o) - C_{p,\ell}(o))$$

where $\Delta C_p (\alpha)$ is the pressure difference at angle of attack,

$C_{p,u}$ is the pressure coefficient on the upper surface,

and $C_{p,\ell}$ is the pressure coefficient on the lower surface.

Since the outer upper-surface pressures were unreliable, an alternate procedure was used for $y/s = 0.7$ and 0.9 and checked at $y/s = 0.4$. If a flow obeys the assumptions of linear potential theory, the effect that a small angle of wing incidence has on pressure is equal and opposite on opposite sides of a thin airfoil - even in the presence of geometric asymmetries. Thus, one could determine the total pressure difference at angle of attack by the calculation:

$$\Delta C_p (\alpha) = (C_{p,u}(\alpha) - C_{p,u}(o)) - (C_{p,\ell}(\alpha) - C_{p,\ell}(o))$$

$$\cong -2 (C_{p,\ell}(\alpha) - C_{p,\ell}(o)).$$

The validity of this procedure can be appraised by inspecting Figure 9, which shows that the angle of attack produces very similar measured pressure changes on the upper and lower surfaces at the inboard chord where $y/s = 0.4$. Since the inner chord ($y/s = 0.1$) is close to the reflection plane and the bodies, viscous effects would be expected to be larger here than on the outer chords. Consequently, the pressure difference was computed directly for this chord and use was not made of the above approximation. The resultant pressure distributions are shown in Figures 22 through 25 and discussed in a subsequent section.

9

Aerodynamic Idealization

Using the doublet lattice method of Ref. 12, aerodynamic influence coefficients were calculated at various subsonic Mach numbers for the configurations studied. As depicted in Figure 10, the aerodynamic idealization consisted of panels of doublets modeling the wing and the idealized surfaces of the bodies in the vicinity of the wing - where interaction effects would be expected to be largest - and of axial doublets representing the bodies themselves.

The strengths of the axial doublets were determined separately, using slender body theory:

$$\left\{ \Delta C_{p,B} \right\} = 2\pi \left\{ R_o\,{}'h{}' + \frac{R_o}{2}h{}'' - \frac{k^2}{2b_r{}^2}R_o h \right\} + 2\pi\frac{k}{b}i\left\{ R_o\,{}'h + R_o h{}' \right\}, \quad (1)$$

while the strengths of the body surface doublets were determined jointly with the wing doublets. To introduce coupling between the two solutions, the boundary conditions to be satisfied by panel doublets were modified by the downwash created by the axial doublets:

$$\left\{ \begin{array}{c} \Delta C_{p,w} \\ \\ \Delta C_{p,I} \end{array} \right\} = \left[\begin{array}{cc} D_{w,w} & D_{w,I} \\ \\ D_{I,w} & D_{I,I} \end{array} \right]^{-1} \left(\left\{ \begin{array}{c} W_w \\ \\ W_I \end{array} \right\} - \left[\begin{array}{c} F_{w,B} \\ \\ F_{I,B} \end{array} \right] \left\{ \Delta C_{p,B} \right\} \right) \quad (2)$$

Ignoring the orbiter fin for the purposes of this study, only the wing, the orbiter fuselage, the external tank and the solid-rocket booster were modeled.

Vehicle Idealization Studies

Wing. - To determine a suitable aerodynamic grid for the analyses, pressure distributions were calculated for several idealizations of the Shuttle wing double-delta platform as shown in Figure 11. Pressures, spanwise lift distributions, and generalized aerodynamic forces were calculated for a zero-frequency pitch mode corresponding to a wing incidence of one radian at $M = 0.7$. Additionally, a control surface rotation mode was studied.

As can be seen in Figure 12, grids 1 and 2 give unsatisfactory pressure calculations on the highly swept inner wing panels. Whereas erratic pressures arise from these idealizations, grid 3 results in smooth distributions.

Chordwise and spanwise variations in the number of boxes in grid 3 were performed as indicated in Figure 11. A major geometrical feature of the wing is leading crank located at 25% of the exposed semispan. As shown in Figure 13, the panel distribution of eight chordwise, three spanwise inboard of the leading edge crank, and seven spanwise outboard of this crank (grid 3.4) gives smooth converged pressures for both wing pitch and control surface rotation; thus, it is used to analyze the full-scale Shuttle with complete vehicle modes. When control-surface modes need not be represented, fewer lattice boxes are required. Hence, grid 3.5, which has only six chordwise panels and gives the same pressure distribution for a pitch mode as does grid 3.4, is used as the aerodynamic idealization for the wing. Smooth oscillatory pressures calculated using this grid are shown in Figure 14 for pitch about the wing apex. Notice the growth of the imaginary part of the pressure as frequency is increased.

Bodies. - The representation of the orbiter fuselage, the external tank, and the solid-rocket booster consisted of axial elements, strengths of which were calculated by slender body theory, and of panels of doublets applied to idealized surface of each body to account for aerodynamic interaction between the wing and bodies. In Ref. 13, idealization studies were made to determine a distribution of slender body elements and interference panels that would give converged generalized aerodynamic forces for the flutter study of a Shuttle configuration. Essentially the same modeling was used in this study.

To appraise effect of the presence of the orbiter fuselage on lift distribution of the wing, steady state lift calculations were made for wing in pitch with various root conditions and compared to the lift obtained with pitched orbiter fuselage in place. In all, five conditions were studied:

(1) Reflection plane located at the wing root, endplating it as in the tested wing alone configuration

(2) Reflection plane located at the vehicle centerplane; the root is free

(3) Reflection plane located at the vehicle centerplane; gap between the root and the centerplane is filled with a rigid plate at zero incidence

(4) Root condition same as in case 3 but rigid plate is at the same angle of incidence as the wing

(5) Pitched fuselage is modelled by slender body elements and interference panels.

Figure 15 shows resulting lift distributions. In case (2), the lift correctly falls to zero at the root because of the gap. Case (3) has a higher wing lift than (2) because the plate supports lift but has lower lift than (1) because the reflection plane in case (1) is more effective than the plate. When

the plate is pitched, it gives rise to even higher lift as shown in case (4). When in case (5) the fuselage is modelled, the lift on the wing is logically more than in case (3) and less than in case (1) because the side wall of the fuselage acts as an abbreviated reflection plane.

Because the bodies on the Shuttle have blunt or truncated aft ends and the orbiter has the rather small ratio of length to diameter of 5.4, the adequacy of slender-body theory is questionable. To resolve this question, calculations of the lift and moment of an orbiter fuselage were made and compared with available unpublished low-speed wind tunnel test data. Although this fuselage is not the same design as the current Shuttle, it has almost the same length to diameter ratio (5.6) and the same truncated aft end. In this analytical idealization, this latter feature was represented by assuming the body radius to remain constant at the end rather than returning to zero. A comparison of theoretical and experimental aerodynamic coefficients is given in Table V. The correlation is fairly good: The lift coefficients agree within 7% and the moment coefficients within 15%.

Pressure Calculations

To compare with the distributions measured on the various configurations at a constant angle of incidence to the flow, steady-state pressures were calculated on the wing for these cases. In this simple case, the slender-body pressures of equation 1 reduce to:

$$\left\{ \Delta C_{p,B} \right\} = 2\pi \left\{ R_o' \; \alpha \right\} \tag{3}$$

Flutter Model Analyses

Using modes measured in the vibration survey, flutter solutions were determined for the models tested. For configurations 2 through 4 of Table III, the rigidity of the bodies causes the slender body pressure to vanish so that equation 2 becomes:

$$\left\{ \begin{array}{c} \Delta C_{p,w} \\ \\ \Delta C_{p,I} \end{array} \right\} = \left[\begin{array}{cc} D_{w,w} & D_{w,I} \\ \\ D_{I,w} & D_{I,I} \end{array} \right]^{-1} \left\{ \begin{array}{c} W_w \\ \\ 0 \end{array} \right\}. \tag{4}$$

12

In configurations 5 and 6, the SRB is allowed to heave and pitch and, hence, gives rise to slender-body pressures as calculated by equation 1. Since the lower frequency mode in each case has very little curvature, the h" term is zero for this mode.

In configuration 1, the base case, there are no bodies to give rise to aerodynamic interaction. In this case equation 4 is further simplified to:

$$\left\{\Delta C_{p,w}\right\} = \left[D_{w,w}\right]^{-1}\left\{W_w\right\}. \tag{5}$$

Full-Scale Flutter Analyses

Calculated symmetric normal modes for the Space Shuttle were obtained from Ref. 14. Table VI lists the frequencies of the lowest 30 modes together with a brief description of each. Only 20 of these modes, as designated in this table, were used in a flutter analysis of the full-scale vehicle. The modes ignored were those that were aerodynamically inactive, such as longitudinal modes. Since the modes entail body motions of a general type, all the terms in equations 1 and 2 are needed in calculating the unsteady pressures and, hence, the associated generalized aerodynamic forces required in the flutter analysis.

MODEL FLUTTER RESULTS

Analytical Results

Shown in Figures 16 and 17 are representative analytical plots of damping and frequency as a function of airspeed for the isolated wing and the Shuttle. From V-g-ω plots such as these, flutter speeds and frequencies were determined for the various configurations at several values of air density over a range of subsonic Mach numbers. The flutter mechanism is the coupling of the fundamental wing bending mode with the first wing torsion mode. Although five modes were used in the flutter calculations for all the various configurations, sample calculations on the isolated wing made including only these two modes gave rise to the same flutter speeds.

For the isolated wing and for the orbiter, Figure 18 shows the resulting trends in flutter speed. Both configurations have basically the same trends: Flutter speed varies little with M until high subsonic Mach numbers are reached, where the variation experienced is strongly dependent on air density. In correlation with test data, consequently, the density ratio must be matched by analysis. Flutter frequency exhibits a similar trend but is not as dependent on air density.

Flutter Boundaries at Test Conditions

Shown in Figure 19(a) are the flutter speed and flutter frequency indices measured on the isolated wing. Also shown are the analytical results obtained at the test conditions. At Mach numbers below 0.9, the analytical flutter speed prediction is at most 6% conservative, while the predicted flutter-frequencies are 5% low at worst. Hence, the correlation in this base case is excellent.

Since the minimum measured flutter speed is only 4 1/2% lower than the measured flutter speed at M = 0.65, the wing can be said to have almost no transonic dip. Because the recovery in flutter speed is sharp, the level of the supersonic flutter speed was not ascertained.

The flutter speed and flutter frequency indices determined for the orbiter configuration are presented in Figure 19(b). Both experiment and analysis show that subsonic flutter speed is higher than that of the wing alone. The accuracy of the predicted flutter speeds is still within 6% and that of the frequencies is within 8%. Although the transonic dip of 7% is slightly more than occurs on the wing alone, it is still very shallow.

As can be seen in Figure 19(c), agreement between test and analysis begins to deteriorate on the orbiter/tank configuration. Up to a Mach number of 0.8, the flutter speeds correlate within 7%, but at M = 0.9 the analysis is 11% conservative.

On the full-up Shuttle configuration with rigid SRB attachments, the Mach number at which correlation deteriorates is seen in Figure 19(d) to shift lower. At M = 0.75, the analytical flutter speed is only 6 1/2% low; but at M = 0.8 and 0.85 the discrepancies are 9% and 13%, respectively.

Figures 19(e) and 19(f) present the flutter boundaries for the full-up Shuttle with flexible SRB attachments. At any given Mach number and density ratio, the flutter speeds calculated by analysis were the same for these two configurations as for the Shuttle with rigid SRB attachments. Hence, when adjusted to the test conditions, the analytical flutter speed boundaries for these three configurations are roughly the same. The test boundaries, however, are lower when flexible attachments are used.

Comparison of Flutter Boundaries

To compare realistically the flutter boundaries of the various configurations, it is necessary first to adjust the test data to a constant air density, since, in the blowdown wind tunnel, different operating points in general correspond to different densities. This scaling was made by multiplying

the test flutter speed by the ratio of the analytical flutter speed at the desired density to that at the test point density. To minimize the amount of scaling to be made, the boundaries were adjusted to a typical tunnel density of three times that at sea level. Figure 20 shows the resulting test flutter boundaries.

At moderate subsonic Mach numbers (M $\leq$ 0.75), the orbiter flutter speed is 7% higher than that of the wing, the orbiter/tank flutter speed is 3% higher than that of the wing and the full-up Shuttle is only 1% higher. No appreciable transonic dip occurs on any configuration. Although all configurations show a sharp flutter speed increase as Mach one is approached, this recovery occurs at increasingly lower Mach numbers as the tank and the SRB are added to the vehicle. This trend causes the order of the flutter speeds to change at the high subsonic Mach numbers so that this order becomes: wing alone lowest, orbiter higher, orbiter/tank higher still, and complete Shuttle highest. This shift in the recovery can probably be attributed to higher local Mach numbers on the wing in the vicinity of the tank and SRB when these components are added to the orbiter.

The analytical flutter boundaries at the same air density of three times that at sea level are shown in Figure 21. At moderate subsonic Mach numbers, the trend is the same as revealed by experiment. As can be seen in Table VII, the predicted percentage differences in the flutter speeds of the various configurations are quite close to those measured at these Mach numbers. Comparison of Figure 20 and 21, however, shows that the transonic trends predicted do not agree with experiment: The theoretical recovery is less and more gradual than experienced in the tests and the presence of the tank and the SRB delay rather than speed the recovery. These failings of the analysis are not unexpected, since the theory assumes that Mach number is constant throughout the flow field.

The adjusted flutter boundaries for the configurations with flexible SRB attachments are presented in Figure 22. These flexibilities cause 2% and 4% decreases in the measured subsonic flutter speed relative to the rigid case, whereas the analytical flutter speed is unaffected. As seen in Table I, the nominal SRB modes are close in frequency to the lowest wing mode, which analysis shows couples with the second wing mode to produce the flutter instability; therefore, an effect by the SRB modes on the flutter speed is not unreasonable. For the tuned flexure, the frequencies of the SRB modes are close to the flutter frequency and the even greater effect on the flutter speed should be expected. The cause of the theory's failure to predict this effect is unknown. However, studies of the Shuttle by Ericsson and Reding in Ref. 15 have shown that flow separation occurs at the shoulder of the SRB nose. It is conceivable that, when the SRB oscillates at frequencies close to the wing flutter frequency, shed vortices impinge upon the wing causing significant deviations from the unsteady pressures expected from potential theory. It is also possible that, since the axial doublet strengths are not determined simultaneously with the panel doublet strengths, the present method is not adequate for calculating interaction effects when the body is allowed to oscillate.

Base Case

For the isolated model wing end-plated at its root, Figure 23 shows good agreement between the calculated and measured steady-state pressure distribution, ΔC_p, when the wing is pitched 3°. Here, and in more detail in Figure 24, even the spillover lift from the outer panel onto the inner panel of the double-delta wing platform can be seen to be predicted.

Correlation on Wing-Body Configurations

For the three configurations for which steady-state pressures were measured, Figures 24 and 25 give a comparison of the calculated and measured distributions for M = 0.6. Comparison of the wing and the orbiter/ET trends from both test and analysis shows that replacing the root-chord reflection plane by the orbiter and tank lowers the pressure at the inboard leading edge of the wing; this effect diminishes outboard and aft. Agreement between test and analysis is good, with analysis overestimating the inboard pressure drop slightly. Similarly, the presence of the SRB lowers pressure further at the inboard leading edge and the amount of this decrease is again predicted fairly reliably. At the inboard trailing edge, both theory and test show that the SRB causes a pressure increase. Outboard the SRB causes the pressure to drop, but analysis underestimates this decrease. Overall the correlation between test and analysis is good; every qualitative feature of the measured distributions is matched.

Figures 26 and 27 show a similar comparison of pressure at M = 0.8. Generally, the analytical trends are the same as for M = 0.6. The measured data, however, does not agree well with these trends. Outboard, the SRB decreases the pressure more than predicted. Inboard, although the leading edge pressures agree with theory, pressures on the remainder of the chord are higher for the more complex configurations than for the isolated wing – the reverse of the predicted trend. This lack of agreement is consistent with the degradation of the flutter correlation on the complex configurations at high subsonic Mach numbers and can probably be attributed to transonic flow phenomena not represented by the theory. There is also the possibility that flow field is being complicated by flow separation and shed vortices.

Configurational Trends

Comparison of pressure distributions for the various configurations with the flutter results seemingly leads to contradictions: Figure 28 shows

that the spanwise loadings for the isolated wing and the orbiter are almost equal as are the centers of pressure. It might be concluded from this that the flutter speeds for these two configurations also should be the same; nevertheless, both test and analysis have shown the orbiter flutter speed to be higher. Also, since in the presence of the external tank and SRB's the loadings decrease and centers of pressure move aft, the flutter speed should increase; however, experimental and analytical flutter results show a flutter speed decrease.

Explanation for this confusion is that these steady-state pressures were measured and calculated for configurations where the entire vehicle was at an incidence angle to the flow. When steady-state pressures were calculated with only the wing at incidence to the flow and the various bodies not inclined to the flow, trends that do support the flutter results are obtained. The resultant spanwise loadings and centers of pressure from such calculations are shown in Figure 29. The following conclusions are drawn:

- Comparison of the wing alone and orbiter configurations shows that replacing the end-plate at the wing root by the rigid, unpitched fuselage extending to the vehicle centerline causes the loading to naturally decrease and the center of pressure to move slightly aft. These are stabilizing trends and a higher flutter speed should be expected on the orbiter.

- The addition of the external tank causes the loading to increase almost up to the original level of the end-plated wing. The flutter speed should be lower than that of the orbiter and slightly higher than that of the wing.

- The addition of the SRB (which one can envision as acting somewhat like a ground plane) raises the loading to a higher level than that of the end-plated wing. This effect should lower the flutter speed again and quite possibly, if the slight aft change in center of pressure does not entirely negate it, drop the flutter speed below that of the wing.

These predictions are entirely consistent with the findings of the flutter analyses.

FULL SCALE FLUTTER RESULTS

Using the 20 symmetric normal modes listed in Table VI and the aerodynamics grid 3.4 shown in Figure 11, flutter speeds were calculated for the isolated wing, the orbiter, and the Shuttle at a Mach number of 0.6 and an altitude of 15,200 m. The full scale vehicle geometry is shown in Figure 1. The resultant V-g-f plots are shown in Figures 30, 31 and 32.

While the flutter speeds of the isolated wing and Shuttle are practically identical, the flutter speed of the orbiter is 3% higher. This is the same trend as was found on the models. On the full Shuttle, two marginal instabilities occur at speeds less than 685 knots but as little as 1% structural damping stabilizes these roots at all speeds less than 685 knots.

Additional analyses were performed eliminating selected normal modes. As shown in Figure 33, a flutter speed that is only 2% different from that obtained using 20 modes can be calculated using only five: wing 1st bending, inboard elevon rotation, fuselage pitch (on interstage fittings), fuselage vertical translation (on interstage fittings), and wing 1st torsion.

CONCLUSIONS

- For general combinations of large rigid bodies in proximity to lifting surfaces, the doublet-lattice/interaciton-panel method successfully predicts the effects of aerodynamic interaction on the flutter speed of the surface at moderate subsonic Mach numbers (M < 0.75).

- More investigation is needed to determine if the effect of flexible or flexibly supported bodies on the oscillatory pressures and, hence, on the flutter speed of a proximate lifting surface can be successfully predicted by the present analysis or a modification of it.

- Steady-state pressures on a lifting surface due to the interaction between it and nearby bodies can be adequately calculated by the present method at M < .75.

- The subsonic flutter speed (M < .75) of the wing in the presence of all the bodies on the Shuttle is practically the same as that of the wind end-plated at its root. The subsonic flutter speeds of intermediate configurations, such as the orbiter, are higher than that of the wing.

REFERENCES

1. Stahle, C.V.: Transonic Effects on T-tail Flutter. The Martin Company Report RM-24, 1959.

2. Topp, L.J.; Rowe, W.S.; and Shattuck, A.W.: Aeroelastic Considerations in the Design of Variable Sweep Airplanes. ICAS Paper No. 66-12, Sept. 1966.

3. Watkins, C.E.; Runyan, H.L.; and Cunningham, H.J.: A Systematic Kernel Function Procedure for Determining Aerodynamic Forces on Oscillating or Steady Finite Wings at Subsonic Speeds. NASA TR R-48, 1959.

4. Albano, E.; and Rodden, W.P.: A Doublet Lattice Method for Calculating Lift Distributions on Oscillating Surfaces in Subsonic Flow. AIAA Journal, Vol. 7, No. 2, Feb. 1969, pp. 279-285.

5. Stark, V. J. E.: Aerodynamic Forces on a Combination of a Wing and a Fin Oscillating in Subsonic Flow. SAAB TN 54, Feb. 1964.

6. Sensberg, O.; and Laschka, B.: Flutter Induced by Aerodynamic Interference between Wing and Tail. Journal of Aircraft, Vol. 7, No. 4, July-Aug. 1970, pp. 319-324.

7. Mykytow, W.J.; Noll, T.E.; Huttsell, L.J.; and Shirk, M.H.: Investigations Concerning the Coupled Wing-Fuselage-Tail Flutter Phenomenon. Journal of Aircraft, Vol. 9, No. 1, Jan. 1972, pp. 48-54.

8. Triplett, W.E.; Burkhart, T. H.; and Birchfield, E. B.: A Comparison of Methods for the Analysis of Wing-Tail Interaction Flutter. AIAA Paper 70-80, Jan. 1970.

9. Chipman. R. R.; Rauch, F. J.; and Hess, R. W.: Flutter of Pairs of Aerodynamically Interfering Delta Wings. Journal of Aircraft, Vol. 5, No. 6, Dec. 1973, pp. 728-734.

10. Woodward, F. A.: Analysis and Design of Wing-Body Configurations at Subsonic and Supersonic Speeds, Journal of Aircraft, Vol. 5, No. 6, Dec. 1968, pp. 528-534.

11. Hess, J. L. and Smith, A. M. O.: Calculation of Non-Lifting Potential Flow About Arbitrary Three Dimensional Bodies. Douglas Aircraft Company Report No. E.S. 40622, 1962.

12. Rodden, W.P.; Giesing, J. P.; and Kalman, T.P.: New Developments and Applications of the Subsonic Doublet-Lattice Method for Nonplanar Configurations, AGARD Symposium on Unsteady Aerodynamics for Aeroelastic Analyses of Interfering Surfaces, Paper No. 4, presented in Tonsberg, Oslofjorden, Norway, November 1970, AGARD-CP-80-71.

13. Chipman, R.R.; and Shyprykevich, P.: Analysis of Wing-Body Interaction Flutter for a Preliminary Space Shuttle Design. NASA CR-2429, 1974.

14. Chesler, J.; Mitchell, L.; and Clark, W.: Preliminary Shuttle Flutter Analysis and Vibration Analyses, Vol. II. Grumman Aerospace Corp. Report LD RS-5, Oct. 1973.

15. Ericsson, L.E.; and Reding, J.P.: Unsteady Aerodynamic Analysis of Space Shuttle Vehicles. Lockheed Missiles and Space Company Report LMSC-D352320, Aug. 1973.

TABLE I.— 1/80TH-SCALE SHUTTLE MODEL FREQUENCIES

MODE	FREQUENCY, Hz
WING 1st BENDING	169.1
WING 1st TORSION	449.5
WING 2nd BENDING	548.0
WING 2nd TORSION	912.1
WING 3rd BENDING	1045.9
SRB PITCH	
NOMINAL FLEXURE	124.0
TUNED FLEXURE	222.0
SRB HEAVE	
NOMINAL FLEXURE	242.9
TUNED FLEXURE	438.0

TABLE II.– CALCULATED MASS & NODE POINT LOCATION

VIB NODE	MASS POINT	X METERS	X INCHES	Y METERS	Y INCHES	MASS KILOGRAMS x 10^3	MASS SLUGS x 10^3
	1	0.2505	9.86	0.0397	1.56	1.048	0.0718
31	2*	0.2505	9.86	0.0460	1.81	0.591	0.0405
32	3*	0.2861	11.26	0.0397	1.56	2.673	0.1832
29	4*	0.2861	11.26	0.0524	2.06	1.477	0.1012
33	5*	0.3302	13.00	0.0397	1.56	3.172	0.2174
30	6*	0.3302	13.00	0.0524	2.06	2.224	0.1524
21	7*	0.3302	13.00	0.0651	2.56	1.201	0.0823
34	8*	0.3543	13.95	0.0397	1.56	1.243	0.0852
	9	0.3543	13.95	0.0524	2.06	0.680	0.0466
22	10*	0.3543	13.95	0.0651	2.56	0.738	0.0506
12	11*	0.3543	13.95	0.0778	3.06	0.664	0.0455
35	12*	0.3781	14.89	0.0397	1.56	2.457	0.1684
	13	0.3781	14.89	0.0524	2.06	2.183	0.1496
23	14*	0.3781	14.89	0.0651	2.56	1.948	0.1335
	15	0.3781	14.89	0.0778	3.06	1.245	0.0853
13	16*	0.3781	14.89	0.0905	3.56	0.620	0.0425
6	17*	0.3781	14.89	0.1032	4.06	0.691	0.0473
36	18*	0.3966	15.61	0.0397	1.56	1.952	0.1337
	19	0.3966	15.61	0.0524	2.06	2.019	0.1384
24	20*	0.3966	15.61	0.0651	2.56	1.261	0.0864
	21	0.3966	15.61	0.0778	3.06	1.092	0.0748
14	22*	0.3966	15.61	0.0905	3.56	0.709	0.0486
	23	0.3966	15.61	0.1032	4.06	0.416	0.0285
7	24*	0.3966	15.61	0.1159	4.56	0.403	0.0276
5	25*	0.3966	15.61	0.1286	5.06	0.356	0.0244
37	26*	0.4150	16.34	0.0397	1.56	1.931	0.1323
	27	0.4150	16.34	0.0524	2.06	1.867	0.1279
25	28*	0.4150	16.34	0.0651	2.56	1.026	0.0703
	29	0.4150	16.34	0.0778	3.06	0.975	0.0668
15	30*	0.4150	16.34	0.0905	3.56	0.855	0.0586
	31	0.4150	16.34	0.1032	4.06	0.556	0.0381
8	32*	0.4150	16.34	0.1159	4.56	0.650	0.0445
	33	0.4150	16.34	0.1286	5.06	0.381	0.0261
1	34*	0.4150	16.34	0.1413	5.56	0.347	0.0238
38	35*	0.4308	16.96	0.0397	1.56	1.716	0.1176
	36	0.4308	16.96	0.0524	2.06	1.718	0.1177
26	37*	0.4308	16.96	0.0651	2.56	0.569	0.0390
	38	0.4308	16.96	0.0778	3.06	0.820	0.0561
16	39*	0.4308	16.96	0.0905	3.56	0.747	0.0512
	40	0.4308	16.96	0.1032	4.06	0.542	0.0372
9	41*	0.4308	16.96	0.1159	4.56	0.696	0.0477
	42	0.4308	16.96	0.1286	5.06	0.333	0.0228
2	43*	0.4308	16.96	0.1314	5.56	0.571	0.0392
39	44*	0.4416	17.39	0.0397	1.56	0.311	0.0213
	45	0.4416	17.39	0.0524	2.06	0.384	0.0263
27	46*	0.4416	17.39	0.0651	2.56	0.274	0.0187
19	47*	0.4416	17.39	0.0778	3.06	0.465	0.0319
40	48*	0.4591	18.08	0.0397	1.56	0.246	0.0169
	49	0.4591	18.08	0.0524	2.06	0.651	0.0384
28	50*	0.4591	18.08	0.0651	2.56	0.247	0.0169
20	51*	0.4591	18.08	0.0778	3.06	0.394	0.0270
17	52*	0.4416	17.39	0.0905	3.56	0.175	0.0120
	53	0.4416	17.39	0.1032	4.06	0.179	0.0122
10	54*	0.4416	17.39	0.1159	4.56	0.200	0.0137
	55	0.4416	17.39	0.1286	5.06	0.147	0.0101
3	56*	0.4416	17.39	0.1413	5.56	0.227	0.0156
18	57*	0.4543	17.89	0.0905	3.56	0.293	0.0201
	58	0.4543	17.89	0.1032	4.06	0.231	0.0159
11	59*	0.4543	17.89	0.1159	4.56	0.279	0.0191
	60	0.4543	17.89	0.1286	5.06	0.367	0.0251
4	61*	0.4543	17.89	0.1413	5.56	0.415	0.0285

*VIBRATION SURVEY MEASUREMENT POINTS

TABLE III.– MODEL CONFIGURATIONS STUDIED

CONFIGURATION	*INVESTIGATIONS PERFORMED
1. ISOLATED WING	P AND F
2. ORBITER	F
3. ORBITER & TANK	P AND F
4. SHUTTLE (RIGID CONNECTION)	P AND F
5. SHUTTLE (NOMINAL FLEXURE)	F
6. SHUTTLE (TUNED FLEXURE)	F

*P–PRESSURE DISTRIBUTION (STEADY STATE)
 F–FLUTTER BOUNDARY DETERMINATION

TABLE IV. – FLUTTER TEST DATA

(a) Wing

RUN	POINT	MODEL	MODEL BEHAVIOR	MACH	DYNAMIC PRES. (N/M2)	(PSI)	TRUE VELOCITY (M/SEC)	(FT/SEC)	SIGMA	MASS DEN. RATIO	FREQ. (HZ)	FLUTTER SPEED INDEX
13	001	1M*	FI	0.812	86961.	12.60	258.2	847.2	2.127	15.22	272.	0.392
13	002	1M*	FSS	0.795	95735.	13.87	253.1	830.5	2.438	13.26	283.	0.411
14	001	1M*	S	0.830	54685.	7.92	265.3	870.5	1.267	25.56		0.310
14	002	1M*	FI	0.932	111154.	16.11	289.6	949.8	2.164	14.96	270.	0.443
14	003	1M*	FSS	0.946	123572.	17.91	292.5	959.6	2.356	13.74	271.	0.467
15	001	1M*	LD	0.666	87621.	12.70	218.1	715.7	3.004	10.76	315.	0.393
15	002	1M*	FI	0.663	97052.	14.07	216.6	710.9	3.373	9.60	311.	0.414
15	2.1	1M*	FSS	0.679	104987.	15.22	221.2	725.7	3.501	9.25	315.	0.430
16	001	1M*	FI	1.034	146817.	21.29	317.7	1042.3	2.373	13.64	306.	0.509
16	002	1M*	FI	1.026	170603.	24.73	314.4	1031.5	2.816	11.50	330.	0.549
16	003	1M*	FSS	1.018	186656.	27.06	308.7	1012.9	3.195	10.15	330.	0.574
16	004	1M*	FD	0.988	175802.	25.48	300.9	987.2	3.168	10.22	315.	0.557
17	001	1M*	LD	0.870	70132.	10.16	280.4	920.1	1.454	22.26	246.	0.352
17	002	1M*	FI	0.868	88174.	12.78	276.9	908.7	1.875	17.27	260.	0.394
17	003	1M*	FSS	0.873	100619.	14.58	275.0	902.5	2.169	14.92	260.	0.421
17	004	1M*	FSS	0.865	104749.	15.18	272.9	895.5	2.294	14.12	263.	0.430
18	001	1M*	FSS	0.700	109040.	15.80	220.6	723.9	3.654	8.86	312.	0.439
18	002	1M*	FSS	0.682	106899.	15.49	214.7	704.4	3.783	8.56	310.	0.434
18	3	1M*	FI	0.700	97442.	14.12	223.6	733.8	3.178	10.19	304.	0.415
29	001	2M*	S	1.357	179919.	26.08	394.0	1292.8	1.890	17.13		0.564
29	002	2M*	S	1.346	202349.	29.33	388.3	1274.1	2.189	14.79		0.598
30	001	2M*	S	1.244	208201.	30.18	366.3	1201.9	2.531	12.79		0.606
31	001	2M*	S	1.113	171242.	24.82	331.2	1086.7	2.546	12.72		0.550
32	001	2M*	FI	0.678	118289.	17.14	221.6	727.2	3.929	8.24		0.457
33	001	2M*	FSS	0.939	116920.	16.95	299.6	983.1	2.124	15.24	260.	0.454
33	002	2M*	FSS	0.959	139466.	20.21	301.3	988.7	2.505	12.92	273.	0.496
33	3	2M*	FI	0.944	109039.	15.80	302.7	993.4	1.940	16.69	245.	0.439
34	001	2M*	FSS	0.832	108011.	15.65	269.7	884.9	2.422	13.37	275.	0.436
34	2	2M*	FSS	0.828	96774.	14.02	271.5	890.8	2.142	15.12	264.	0.413
35	001	2M*	FI	0.736	111159.	16.11	240.2	788.3	3.141	10.31	305.	0.443
35	2	2M*	FSS	0.738	116968.	16.95	241.7	793.2	3.265	9.92	306.	0.454
35	3	2M*	FSS	0.735	105996.	15.36	239.8	786.8	3.006	10.77	300.	0.432
36	001	2M*	FI	0.685	115162.	16.69	221.5	727.3	3.824	8.47	315.	0.451
36	002	2M*	FSS	0.705	123183.	17.85	227.4	746.2	3.885	8.33	314.	0.466

(b) Wing and Fuselage

RUN	POINT	MODEL	MODEL BEHAVIOR	MACH	DYNAMIC PRES. (N/M2)	(PSI)	TRUE VELOCITY (M/SEC)	(FT/SEC)	SIGMA	MASS DEN. RATIO	FREQ. (HZ)	FLUTTER SPEED INDEX
37	001	2M*	FI	0.857	119324.	17.29	271.1	889.6	2.648	12.23	266.	0.459
37	002	2M*	FI	0.849	129388.	18.75	268.2	880.1	2.933	11.04	272.	0.478
38	001	2M*	LD	1.069	134920.	19.56	328.7	1078.4	2.037	15.89	279.	0.468
38	002	2M*	LD	1.049	145503.	21.09	322.7	1058.7	2.280	14.20	290.	0.507
38	003	2M*	FI	1.030	165913.	24.05	317.0	1040.1	2.693	12.02	316.	0.541
39	001	2M*	S	0.593	94554.	13.70	190.7	625.6	4.242	7.63		0.408
40	001	2M*	LD	0.767	96903.	14.04	246.6	809.2	2.599	12.46	300.	0.413
40	1.1	2M*	FSS	0.762	114096.	16.54	241.5	792.5	3.190	10.15	290.	0.449
40	002	2M*	FSS	0.746	126296.	18.30	230.3	755.7	3.884	8.34	303.	0.472
41	.1	2M*	FI	0.956	98381.	14.26	302.2	991.7	1.757	18.43	250.	0.417
41	001	2M*	FSS	0.927	123602.	17.91	293.2	962.0	2.345	13.81	280.	0.467
41	002	2M*	FSS	0.900	126151.	18.28	282.4	926.5	2.581	12.55	270.	0.472
42	001	2M*	FI	1.046	168611.	24.44	318.8	1046.0	2.706	11.96	300.	0.545
42	002	2M*	FI	1.039	180483.	26.16	313.7	1029.1	2.992	10.82	310.	0.564
42	003	2M*	FI	1.016	180713.	26.19	301.4	988.8	3.246	9.97	310.	0.565
43	001	2M*	FI	1.107	183123.	26.54	331.9	1089.0	2.712	11.94	310.	0.569
43	002	2M*	S	1.104	190101.	27.55	328.0	1076.0	2.882	11.23		0.579
44	001	2M*	S	0.624	96665.	14.01	193.5	634.9	4.212	7.69		0.413
45	001	2M*	S	0.754	92658.	13.43	244.0	800.6	2.538	12.76		0.404
45	002	2M*	FI	0.748	106064.	15.37	241.1	791.3	2.975	10.86	295.	0.433
45	003	2M*	FSS	0.737	123351.	17.88	236.6	776.5	3.593	9.01	310.	0.466
46	001	2M*	FI	0.813	88946.	12.89	260.9	856.1	2.131	15.20	280.	0.396
46	002	2M*	FSS	0.821	106925.	15.50	262.3	860.7	2.535	12.77	270.	0.434
47	001	2M*	FI	0.933	95810.	13.89	296.3	972.4	1.779	18.20	270.	0.411
47	002	2M*	FSS	0.924	120118.	17.41	290.7	953.9	2.318	13.97	270.	0.460
48	001	2M*	FI	0.992	127486.	18.48	309.7	1016.0	2.169	14.93	280.	0.474
48	002	2M*	FSS	0.979	161864.	23.46	303.5	995.9	2.866	11.30	310.	0.534
49	001	2M*	S	1.193	177016.	25.66	356.1	1168.4	2.277	14.22		0.559
49	002	2M*	S	1.171	207943.	30.14	348.4	1143.1	2.795	11.59		0.606
50	001	2M*	S	1.256	187575.	27.19	373.9	1226.8	2.189	14.79		0.575
50	002	2M*	S	1.262	211671.	30.68	365.0	1197.5	2.592	12.49		0.611
51	001	2M*	S	1.370	174738.	25.33	399.6	1311.3	1.785	18.14		0.555
51	002	2M*	S	1.363	217863.	31.58	390.0	1279.5	2.337	13.85		0.620

S	STABLE	FSS	STEADY STATE FLUTTER
LD	LOW DAMPING	FD	DIVERGENT FLUTTER
FI	INTERMITTENT FLUTTER		

TABLE IV. – CONTINUED

(c) Wing, Fuselage and Tank

RUN	POINT	MODEL	MODEL BEHAVIOR	MACH	DYNAMIC PRES. (N/M2)	(PSI)	TRUE VELOCITY (M/SEC)	(FT/SEC)	SIGMA	MASS DEN. RATIO	FREQ. (HZ)	FLUTTER SPEED INDEX
52	001	2M*	S	0.587	93414.	13.54	186.7	612.8	4.369	7.41		0.406
53	001	2M*	FSS	0.845	113215.	16.41	272.0	892.3	2.497	12.97	273.	0.447
53	002	2M*	FSS	0.832	117244.	16.99	266.7	875.1	2.668	12.04	285.	0.455
54	001	2M*	LD	0.715	100628.	14.59	232.0	761.4	3.048	10.62	300.	0.421
54	002	2M*	FSS	0.705	115469.	16.74	224.4	736.5	3.738	8.66	310.	0.451
54	2.1	2M*	FSS	0.688	109010.	15.80	219.1	718.8	3.705	8.74	312.	0.439
55	001	2M*	FSS	0.775	109582.	15.88	249.1	817.5	2.879	11.25	295.	0.440
55	1.1	2M*	FSS	0.784	114488.	16.59	250.7	822.5	2.972	10.93	295.	0.449
55	002	2M*	FSS	0.772	118550.	17.18	247.0	810.4	3.170	10.21	300.	0.457
56	001	2M*	FSS	0.899	113822.	16.50	284.1	932.2	2.500	14.06	270.	0.448
56	1.1	2M*	FSS	0.906	121001.	17.54	286.0	938.5	2.413	13.42	275.	0.462
56	002	2M*	FSS	0.905	130718.	18.95	286.0	938.4	2.607	12.42	285.	0.460
56	2.1	2M*	FSS	0.894	141709.	20.54	281.5	923.6	2.917	11.10	295.	0.500
57	001	2M*	FSS	0.944	155693.	22.57	292.8	960.9	2.961	10.93	315.	0.524
57	1.1	2M*	FSS	0.932	157042.	22.76	289.6	950.1	3.055	10.60	305.	0.526
58	.1	2M*	FI	0.990	180115.	26.11	304.0	997.4	3.180	10.18	282.	0.564
58	001	2M*	S	0.973	181185.	26.26	296.8	973.8	3.356	9.65		0.565
58	002	2M*	FSS	0.913	157004.	22.76	280.2	919.3	3.262	9.92	286.	0.526
58	2.1	2M*	FSS	0.856	132701.	19.23	263.4	864.4	3.119	10.38	286.	0.484
58	2.2	2M*	FSS	0.921	161126.	23.35	282.5	926.9	3.294	9.83	286.	0.533
59	.1	2M*	FSS	1.100	186142.	26.98	334.4	1097.2	2.715	11.92	320.	0.573
59	001	2M*	FSS	1.105	188494.	27.32	335.1	1099.7	2.737	11.83	312.	0.577
59	1.1	2M*	FSS	1.087	188381.	27.31	330.7	1084.9	2.810	11.52	312.	0.577
59	1.2	2M*	FSS	1.077	188482.	27.32	326.9	1072.6	2.877	11.25	310.	0.577
59	1.3	2M*	FSS	1.073	188508.	27.32	325.2	1067.2	2.907	11.14	318.	0.577
59	1.4	2M*	S	1.056	185107.	26.83	316.1	1037.1	3.023	10.71		0.572
60	001	2M*	S	1.131	204015.	29.57	334.6	1097.9	2.972	10.89	320.	0.600
60	1.1	2M*	FSS	1.107	189588.	27.48	329.9	1082.5	2.842	11.39	320.	0.578
60	1.2	2M*	FI	1.121	198355.	28.75	333.6	1094.7	2.907	11.14	320.	0.592
61	001	2M*	S	1.238	217723.	31.56	364.5	1195.9	2.673	12.11		0.620
62	001	2M*	S	1.346	215941.	31.30	383.7	1258.9	2.393	13.53		0.617
63	001	2M*	FSS	0.885	119489.	17.32	279.3	916.4	2.498	12.96	275.	0.459
64	.1	2M*	FSS	0.744	108780.	15.77	241.1	791.2	3.051	10.61	298.	0.438
64	001	2M*	FSS	0.723	109193.	15.83	234.6	769.9	3.235	10.01	295.	0.439
64	002	2M*	FSS	0.702	118945.	17.24	227.2	745.6	3.758	8.62	310.	0.458
64	2.1	2M*	S	0.632	99129.	14.37	206.0	675.8	3.812	8.49		0.418
64	2.2	2M*	FSS	0.680	116380.	16.87	219.9	721.6	3.925	8.25	312.	0.453
65	001	2M*	FI	1.002	163780.	23.74	305.0	1000.8	2.871	11.28	310.	0.538
65	002	2M*	S	0.978	168271.	24.39	299.1	981.5	3.068	10.55		0.545
65	2.1	2M*	FSS	0.938	152000.	22.03	286.7	940.7	3.016	10.73	300.	0.518
65	2.2	2M*	FSS	0.874	125955.	18.26	268.0	879.3	2.861	11.32	280.	0.471

(d) Wing, Fuselage, Tank, and Rigid SRM

RUN	POINT	MODEL	MODEL BEHAVIOR	MACH	DYNAMIC PRES. (N/M2)	(PSI)	TRUE VELOCITY (M/SEC)	(FT/SEC)	SIGMA	MASS DEN. RATIO	FREQ. (HZ)	FLUTTER SPEED INDEX
19	001	1M*	FI	0.671	106548.	15.44	213.3	699.8	3.821	8.47	320.	0.434
19	1.1	1M*	FSS	0.665	106718.	15.47	211.1	692.8	3.905	8.29	328.	0.434
19	002	1M*	S	0.673	108835.	15.77	214.3	703.1	3.866	8.37		0.438
20	001	1M*	FI	0.847	111838.	16.21	261.5	857.9	2.668	12.13	290.	0.444
20	1.1	1M*	FI	0.838	126919.	18.40	258.7	849.0	3.092	10.47	314.	0.473
20	002	1M*	FI	0.842	136933.	19.85	259.5	851.6	3.316	9.76	310.	0.492
20	2.1	1M*	FI	0.803	124400.	18.03	249.1	817.3	3.270	9.90	310.	0.468
21	001	1M*	LD	0.772	99556.	14.43	247.0	810.5	2.661	12.17	294.	0.419
21	002	1M*	FSS	0.754	109565.	15.88	239.0	784.2	3.129	10.35	310.	0.440
22	001	1M*	LD	0.947	105388.	15.27	297.2	975.1	1.946	16.64	282.	0.431
22	002	1M*	FSS	0.909	134074.	19.43	283.9	931.4	2.714	11.93	317.	0.466
22	003	1M*	FSS	0.910	142454.	20.65	284.0	931.8	2.881	11.24	309.	0.501
23	001	1M*	S	0.575	92755.	13.44	184.9	606.7	4.425	7.32		0.404
24	001	1M*	S	1.330	170303.	24.68	386.4	1268.0	1.860	17.41		0.548
24	002	1M*	S	1.325	208968.	30.29	381.8	1252.8	2.338	13.85		0.607
25	001	1M*	S	1.098	93413.	13.54	337.6	1107.7	1.337	24.22		0.406
25	002	1M*	S	1.112	171939.	24.92	336.1	1102.9	2.482	13.05		0.551
25	003	1M*	S	1.101	197209.	29.59	330.3	1083.6	2.949	10.98		0.590
27	001	1M*	LD	0.977	148236.	21.49	303.1	994.5	2.632	12.30	306.	0.511
27	002	1M*	FI	0.958	174558.	25.30	296.1	971.5	3.248	9.97	332.	0.555
27	003	1M*	FSS	0.910	164237.	23.81	281.4	923.2	3.384	9.57	335.	0.538
28	001	1M*	S	0.769	82570.	11.97	247.1	810.7	2.206	14.68		0.382
28	002	1M*	S	0.467	17190.	2.49	149.9	491.9	1.247	25.96		0.174
28	003	1M*	LD	0.896	80524.	11.67	284.6	933.7	1.622	19.97	280.	0.377
28	004	1M*	FI	0.909	126922.	18.40	293.6	963.5	2.401	13.48	310.	0.473
28	4.1	1M*	FSS	0.793	134249.	19.46	252.1	827.2	3.446	9.40	312.	0.487
28	005	1M*	FSS	0.795	138309.	20.05	257.2	843.8	3.411	9.49	315.	0.494
28	5.1	1M*	FSS	0.738	108626.	15.74	231.8	760.6	3.298	9.82	310.	0.438
28	006	1M*	LD	0.679	87254.	12.64	214.0	702.1	3.108	10.42	314.	0.392

TABLE IV. — CONCLUDED

(e) Wing, Fuselage, Tank and SRM (Flexure I)

RUN	POINT	MODEL	MODEL BEHAVIOR	MACH	DYNAMIC PRES. (N/M2)	(PSI)	TRUE VELOCITY (M/SEC)	(FT/SEC)	SIGMA	MASS DEN. RATIO	FREQ. (HZ)	FLUTTER SPEED INDEX
66	001	2M*	FSS	0.636	102448.	14.85	208.9	685.5	3.829	8.46	319.	0.425
67	001	2M*	FSS	0.874	125769.	18.23	278.3	913.3	2.648	12.23	268.	0.471
69	.1	2M*	S	0.845	104252.	15.11	273.8	898.6	2.267	14.28		0.429
69	001	2M*	FSS	0.791	111381.	16.10	255.9	839.5	2.768	11.70	300.	0.443
69	002	2M*	FSS	0.729	112225.	16.26	235.0	771.2	3.313	9.77	310.	0.445
70	1	5M*	FI	0.776	105526.	15.29	249.0	816.9	2.777	11.66	300.	0.451
70	1.1	5M*	FSS	0.818	128469.	18.62	260.2	853.9	3.094	10.46	295.	0.476
70	002	5M*	FSS	0.779	124381.	18.03	249.1	817.4	3.269	9.90	305.	0.468
71	.1	6M*	FSS	0.895	166919.	24.19	282.7	927.5	3.408	9.50	330.	0.543
71	001	6M*	FSS	0.891	164994.	23.92	281.2	922.6	3.404	9.51	350.	0.540
72	.1	6M*	FI	0.960	149358.	21.65	300.0	984.2	2.708	11.96	320.	0.513
72	.2	6M*	FSS	0.952	161760.	23.45	296.6	973.1	3.000	10.79	330.	0.534
72	001	6M*	FSS	0.946	166140.	24.08	294.3	965.5	3.130	10.34	340.	0.541
73	001	6M*	FI	0.976	183008.	26.53	300.5	986.1	3.305	9.80	340.	0.568
73	1.1	6M*	FSS	0.951	172217.	24.96	293.9	964.3	3.253	9.95	310.	0.551
73	002	6M*	FSS	0.918	158893.	23.03	284.4	933.2	3.204	10.11	310.	0.530
74	001	6M*	S	1.073	201990.	29.28	326.1	1070.0	3.098	10.45		0.597
74	002	6M*	FSS	0.919	136234.	19.75	283.5	930.4	2.764	11.71	295.	0.490
75	001	6M*	S	1.121	209194.	30.32	339.2	1113.1	2.965	10.92		0.608
76	001	6M*	S	1.217	214990.	31.16	358.7	1177.1	2.725	11.88		0.616
77	001	6M*	S	1.321	213839.	31.00	383.8	1259.4	2.368	13.68		0.614
78	001	6M*	FSS	0.917	126972.	18.40	288.2	945.5	2.494	12.98	307.	0.473
79	.1	6M*	FI	0.859	95719.	13.87	276.3	906.5	2.045	15.83	270.	0.411
79	.2	6M*	FSS	0.841	101472.	14.71	269.6	884.5	2.277	14.22	280.	0.423
79	001	6M*	FSS	0.847	110188.	15.97	271.5	890.9	2.438	13.26	275.	0.441
79	002	6M*	FSS	0.824	120471.	17.46	263.3	863.9	2.835	11.42	295.	0.461
80	.1	6M*	FSS	0.660	93679.	13.58	214.0	702.2	3.336	9.70	308.	0.406
80	001	6M*	FSS	0.662	95302.	13.81	214.6	704.2	3.375	9.59	318.	0.410
80	002	6M*	FSS	0.657	99380.	14.40	212.0	695.6	3.607	8.98	310.	0.419

(f) Wing, Fuselage, Tank and SRM (Flexure II)

RUN	POINT	MODEL	MODEL BEHAVIOR	MACH	DYNAMIC PRES. (N/M2)	(PSI)	TRUE VELOCITY (M/SEC)	(FT/SEC)	SIGMA	MASS DEN. RATIO	FREQ. (HZ)	FLUTTER SPEED INDEX
81	001	6M*	FI	0.675	91354.	13.24	219.6	720.6	3.090	10.48	305.	0.401
81	1.1	6M*	FSS	0.664	90608.	13.13	215.9	708.6	3.169	10.22	310.	0.400
81	002	6M*	FSS	0.661	97453.	14.12	214.4	703.6	3.457	9.36	310.	0.415
82	001	6M*	FI	0.787	89499.	12.97	252.1	827.1	2.297	14.10	280.	0.397
82	001	6M*	FSS	0.786	98638.	14.30	251.0	823.7	2.553	12.60	290.	0.417
82	002	6M*	FSS	0.782	102683.	14.89	245.7	816.0	2.708	11.96	292.	0.426
83	.1	6M*	FI	0.728	87632.	12.70	237.0	779.7	2.532	12.79	300.	0.393
83	.2	6M*	FSS	0.736	94451.	13.69	236.5	776.1	2.754	11.76	300.	0.408
83	001	6M*	FSS	0.731	100547.	14.57	233.2	765.1	3.017	10.73	310.	0.421
84	.1	6M*	FI	0.959	146029.	21.17	302.6	992.8	2.602	12.44	320.	0.508
84	001	6M*	FSS	0.936	146373.	21.22	294.1	964.9	2.761	11.73	320.	0.508
85	001	6M*	FSS	0.908	106747.	15.47	288.9	947.9	2.086	15.52	285.	0.454
86	001	6M*	FSS	0.853	110811.	16.06	269.8	885.4	2.402	13.04	280.	0.442
87	.1	6M*	FI	0.856	100297.	14.54	273.7	898.2	2.183	14.83	270.	0.421
87	001	6M*	FSS	0.846	107357.	15.56	268.7	881.8	2.425	13.35	280.	0.435
88	.1	6M*	FI	0.825	93975.	13.62	265.2	870.3	2.179	14.86	280.	0.407
88	001	6M*	FSS	0.806	98569.	14.29	257.9	846.1	2.418	13.39	280.	0.417
89	.1	6M*	FI	0.703	87367.	12.66	225.7	740.5	2.798	11.57	305.	0.393
89	001	6M*	FSS	0.702	96376.	13.97	226.0	741.6	3.077	10.52	303.	0.412
90	.1	6M*	FI	1.008	165962.	24.06	309.1	1014.1	2.854	11.43	350.	0.541
90	001	6M*	FSS	0.986	183312.	26.57	303.1	994.6	3.254	9.95	335.	0.569
90	002	6M*	FSS	0.920	149524.	21.67	281.7	924.4	3.073	10.54	305.	0.514
91	001	6M*	FSS	0.951	139327.	20.19	294.7	967.0	2.617	12.37	320.	0.496
92	001	6M*	S	1.089	212810.	30.85	332.2	1090.0	3.145	10.30		0.613
92	2	6M*	FSS	0.997	174874.	25.35	307.8	1009.8	3.012	10.75	330.	0.556
93	001	6M*	S	1.212	215733.	31.27	359.6	1179.8	2.721	11.90		0.617
94	001	6M*	FSS	0.923	119143.	17.27	289.2	949.0	2.323	13.94	300.	0.458

TABLE V.— AERODYNAMIC COEFFICIENTS FOR AN ORBITER FUSELAGE

	c_{L_α} (DEG^{-1})	c_{M_α} (DEG^{-1})
EXPERIMENT	0.0041	0.0015
ANALYSIS	0.00384	0.00173

TABLE VI.— SHUTTLE SYMMETRIC FREE-FREE NORMAL MODES FOR NOMINAL ELEVONS

MODE NO.	ORDER IN FLUTTER ANALYSIS	FREQ, Hz	GEN WEIGHT, LB	GEN MASS, Kg	PREDOMINANT MODAL DESCRIPTION
1	1	2.25	82,088	37,235	FUSELAGE 1st VERTICAL BENDING
2		2.77	376,078	170,589	SRB YAW
3	2	3.07	231,358	104,944	SRB PITCH
4		3.91	319,346	144,855	SHUTTLE LONGITUDNIAL (FUSELAGE VS OXYGEN)
5		4.04	100,841	45,741	SRB 1st LATERAL BENDING
6		4.33	60,322	27,362	ET 1st VERTICAL BENDING
7	3	5.01	12,607	5,719	PAYLOAD PITCH
8	4	5.17	944	428	WING 1st BENDING
9		5.51	34,416	15,611	ET LONGITUDINAL (OXYGEN VS HYDROGEN)
10		6.17	340,368	154,391	ET/SRB LONGTIUDINAL (SRB VS HYDROGEN)
11	5	6.96	273,739	124,168	SRB 1st VERTICAL BENDING
12		7.36	35,857	16,265	PAYLOAD 1st VERTICAL BENDING
13		8.13	41,131	18,657	FUSELAGE 2nd VERTICAL BENDING
14		8.88	100,011	45,365	ET 2nd VERTICAL BENDING
15	6	10.36	624	283	INBOARD ELEVON ROTATION
16	7	10.63	1,318	598	FUSELAGE PITCH (ON INTERSTAGE FITTINGS)
17	8	10.89	11,567	5,247	SRB 2nd LATERAL BENDING
18	9	11.23	1,238	562	FUSELAGE VERTICAL (ON INTERSTAGE FITTINGS)
19	10	11.98	1,425	646	WING 1st TORSION; OUTBOARD ELEVON ROTATION
20		12.59	10,464	4,746	AFT CREW COMPARTMENT TRUNNION
21		12.97	13,611	6,174	PAYLOAD 1st LONGITUDINAL
22	11	14.11	2,932	1,330	FIN
23		14.30	25,771	11,690	ET 1st LOCAL OXYGEN TANK VERTICAL BENDING
24	12	15.14	363	165	WING 2nd BENDING; OUTBOARD ELEVON TORSION
25	13	15.30	4,014	1,821	FORWARD CREW COMPARTMENT TRUNNION
26	14	16.83	36,957	16,764	SRB 2nd VERTICAL BENDING
27		17.06	14,801	6,714	FUSELAGE 1st LONGITUDINAL
28	15	17.93	6,382	2,895	FUSELAGE 3rd VERTICAL BENDING
29		17.99	13,470	6,110	ET 2nd LOCAL OXYGEN TANK VERTICAL BENDING
30	16	18.62	9,136	4,144	SRB 3rd VERTICAL BENDING
31		19.69	20,870	9,467	SRB 3rd LATERAL BENDING
32	17	20.01	377	171	INBOARD ELEVON TORSION
33	18	20.69	1,163	528	WING 2nd TORSION; OUTBOARD ELEVON ROTATION
34	19	22.40	14,638	6,640	ET 3rd VERTICAL BENDING
35	20	23.81	6,547	2,970	FUSELAGE 2nd LONGITUDINAL

TABLE VII.– EFFECT OF AERODYNAMIC INTER-
ACTION ON FLUTTER SPEED OF A
1/80th-SCALE SHUTTLE MODEL

CONFIGURATION	M	VF/VF OF WING ALONE	
		ANALYSIS	TEST
ORBITER	0.7	1.05	1.07
	0.9	1.02	1.01
ORBITER/ET	0.7	1.02	1.03
	0.9	0.97	1.02
SHUTTLE (RIGID COUPLING)	0.7	1.00	1.01
	0.9	0.95	1.06
SHUTTLE (NOMINAL FLEXURES)	0.7	1.00	0.99
	0.9	0.95	1.03
SHUTTLE (TUNED FLEXURES)	0.7	1.00	0.97
	0.9	0.95	0.97

MODEL

0.149m

0.556m

0.594m

0.719m

FULL SCALE

8.25m

6.18m

2.75m

9.15m

3.61m

23.8m

44.5m

47.5m

57.5m
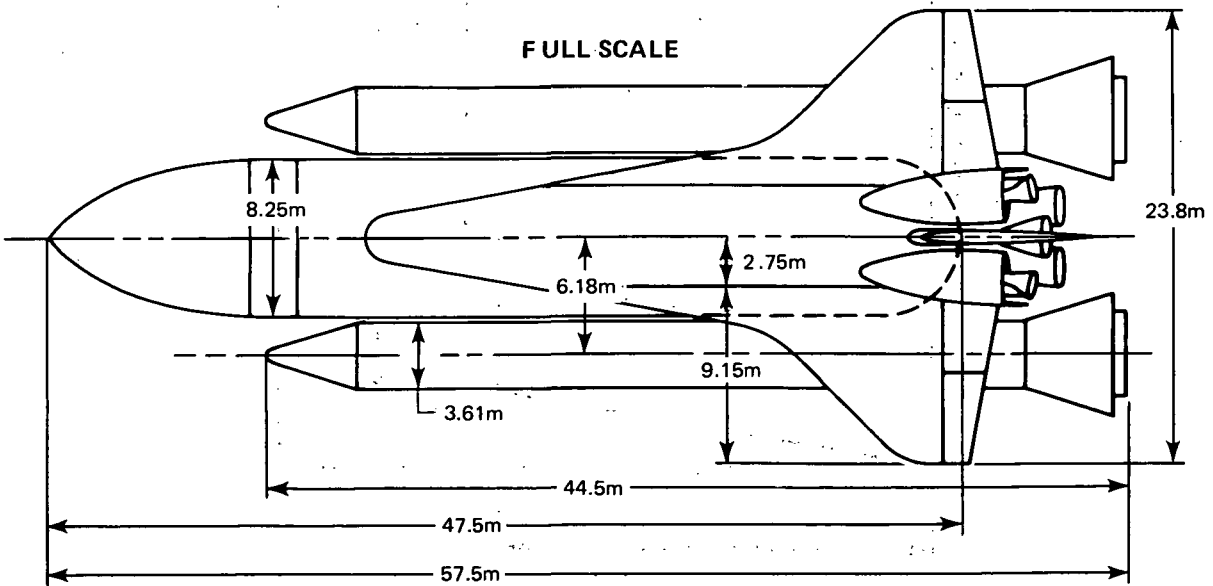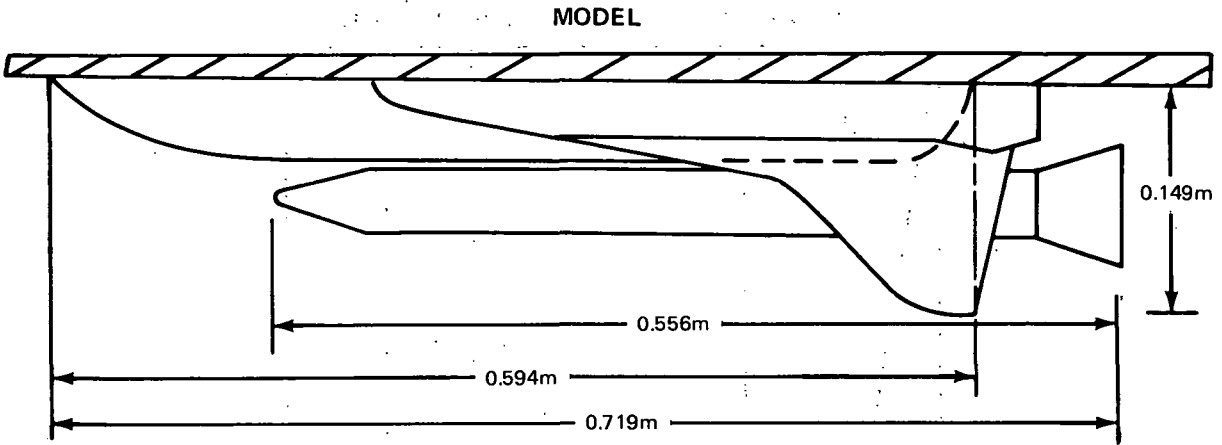
Figure 1. — Space Shuttle Design Studied
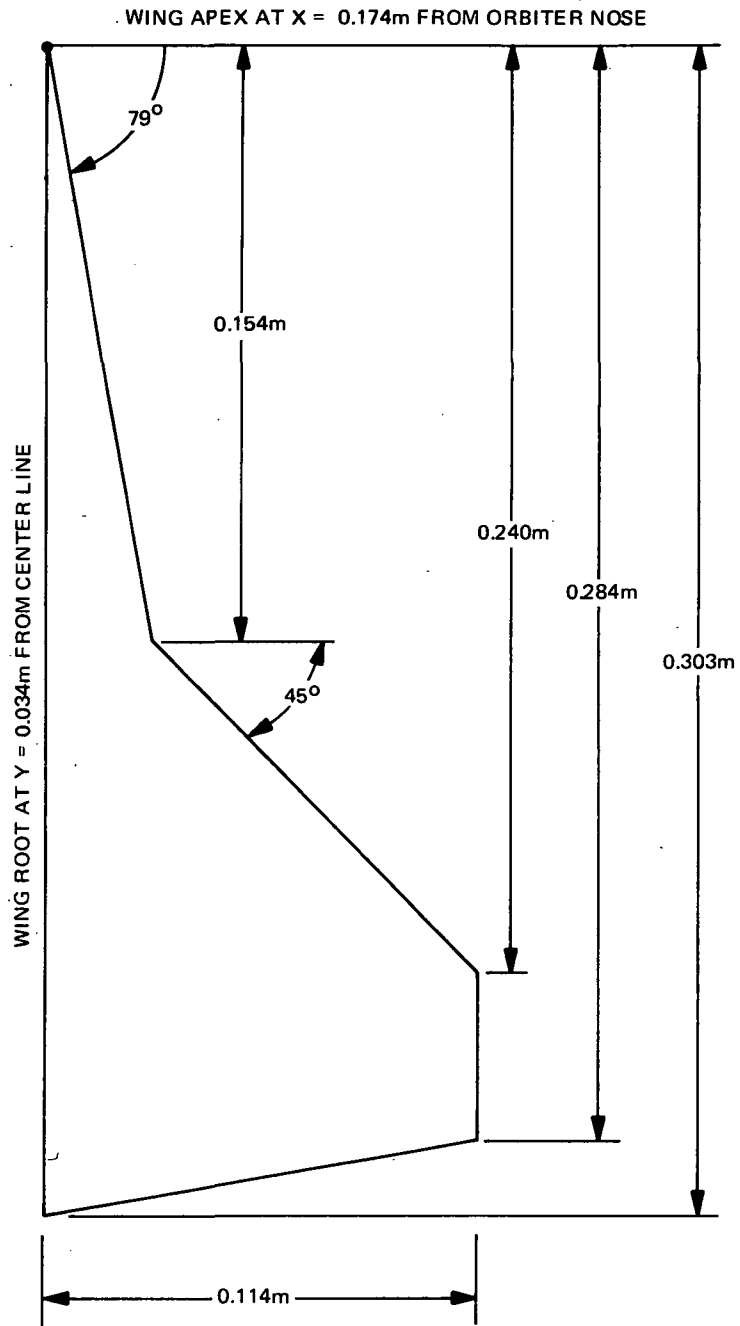
Figure 2.— Orbiter Wing Model
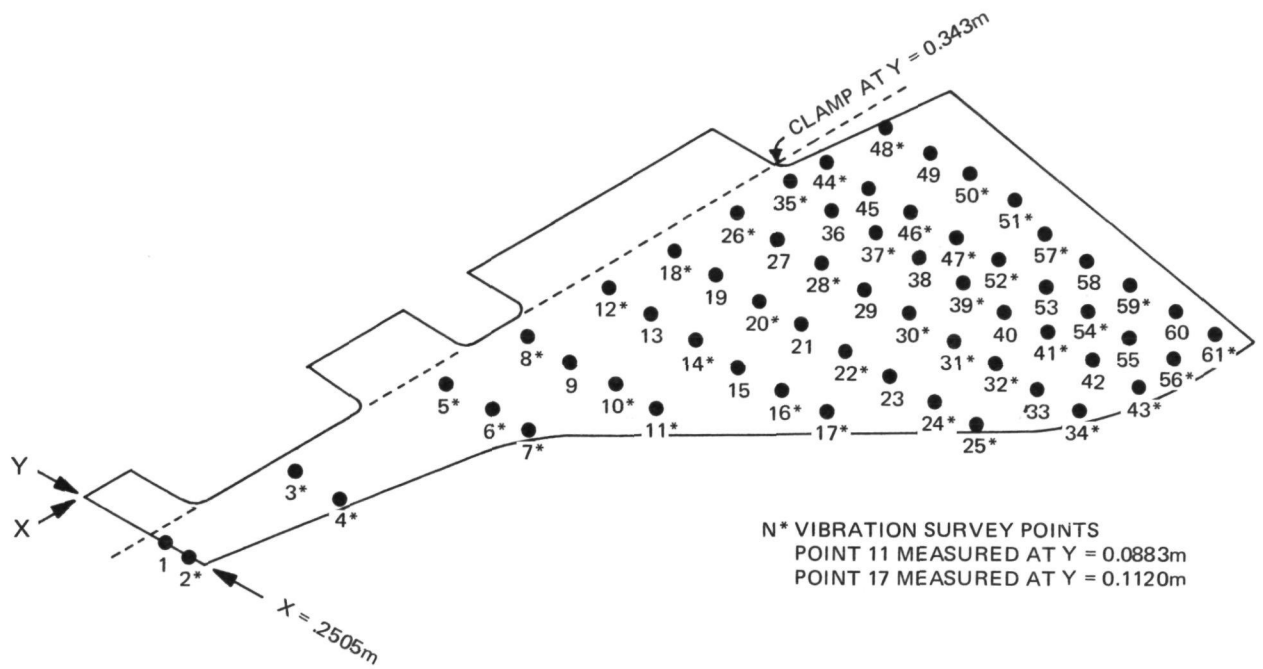
Figure 5.— Mass Point and Vibration Measurement Locations

(a) FREQUENCY = 169.1 Hz   DAMPING COEFFICIENT = .008

FIRST BENDING MODE
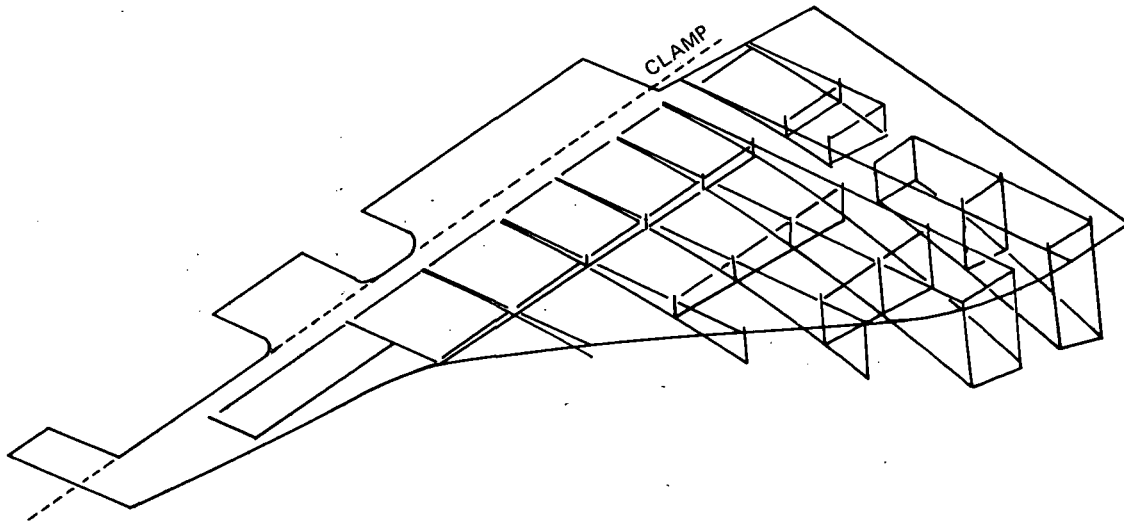
VIB NODE*	NORMALIZED DEFLECTION	VIB NODE	NORMALIZED DEFLECTION	VIB NODE	NORMALIZED DEFLECTION
1	0.72	15	0.22	29	0
2	0.82	16	0.26	30	
3	0.87	17	0.29	31	
4	1.0C	18	0.33	32	
5	0.50	19	0.18	33	
6	0.26	20	0.23	34	
7	0.36	21	0.01	35	
8	0.44	22	0.03	36	0.01
9	0.49	23	0.05	37	0.01
10	0.57	24	0.06	38	0.01
11	0.62	25	0.08	39	0.01
12	0.08	26	0.10	40	0.02
13	0.14	27	0.11		
14	0.18	28	0.12		

(a) 1st Mode   *See First Column of Table II

Figure 6.— Mode Shape Data, 1/80th-Scale Wing
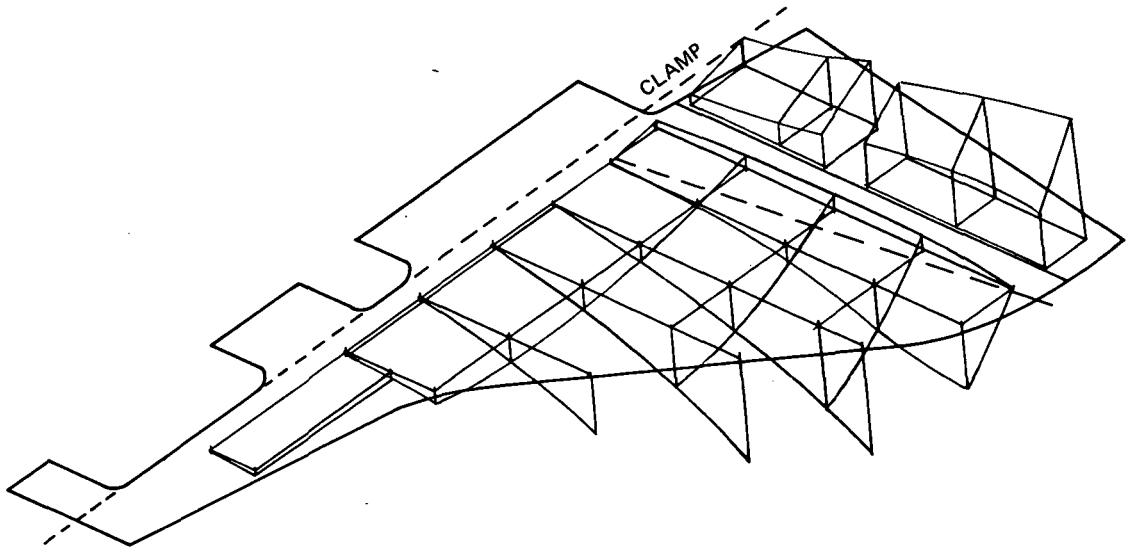
33

FIRST TORSION MODE

VIB NODE*	NORMALIZED DEFLECTION	VIB NODE	NORMALIZED DEFLECTION	VIB NODE	NORMALIZED DEFLECTION
1	-0.565	15	-0.152	29	-0.022
2	0.022	16	0.109	30	-0.044
3	0.435	17	0.326	31	0
4	1.000	18	0.630	32	0
5	-0.913	19	0.260	33	-0.022
6	-0.892	20	0.565	34	-0.022
7	-0.717	21	-0.109	35	-0.022
8	-0.348	22	-0.195	36	-0.022
9	0.109	23	-0.195	37	-0.022
10	0.435	24	-0.130	38	0.066
11	0.825	25	-0.044	39	0.109
12	-0.500	26	0.109	40	0.240
13	-0.500	27	0.175		
14	-0.390	28	0.410		

(b) 2nd Mode   *See First Column of Table II

Figure 6.— Continued

DAMPING COEFFICIENT = .019

SECOND BENDING MODE
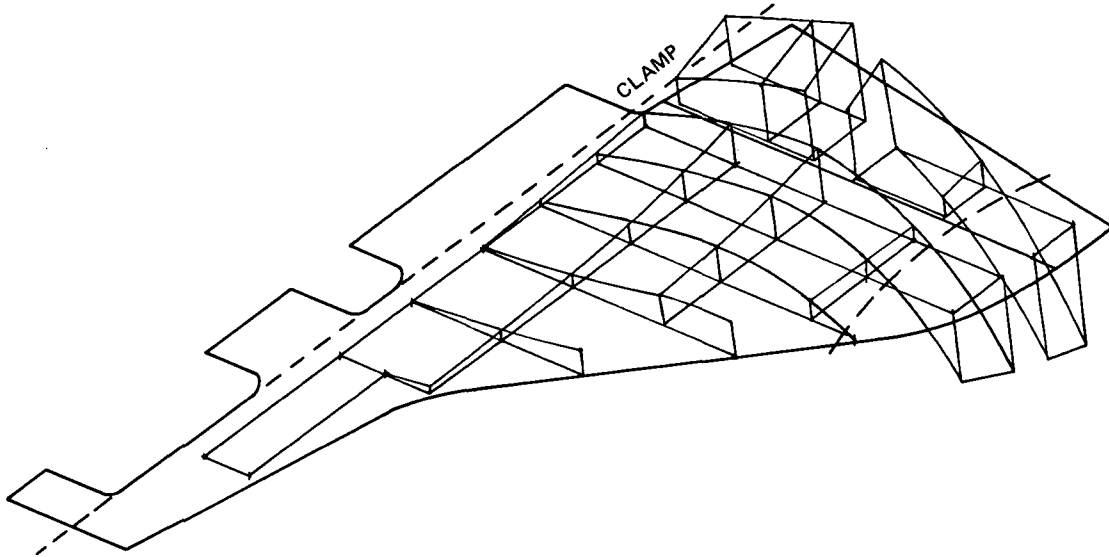
VIB NODE*	NORMALIZED DEFLECTION	VIB NODE	NORMALIZED DEFLECTION	VIB NODE	NORMALIZED DEFLECTION
1	0.59	15	-0.38	29	0
2	0.79	16	-0.48	30	
3	0.90	17	-0.62	31	
4	1.0	18	-0.79	32	
5	0.07	19	-0.59	33	
6	-0.28	20	-0.83	34	
7	-0.17	21	-0.03	35	0
8	-0.14	22	-0.07	36	-0.03
9	-0.14	23	-0.10	37	-0.07
10	-0.17	24	-0.17	38	-0.10
11	-0.24	25	-0.24	39	-0.21
12	-0.21	26	-0.34	40	-0.41
13	-0.24	27	-0.48		
14	-0.31	28	-0.69		

(c) 3rd Mode

*See First Column of Table II

Figure 6.— Continued

(d) FREQUENCY = 912.1 Hz   DAMPING COEFFICIENT = .02

SECOND TORSION MODE
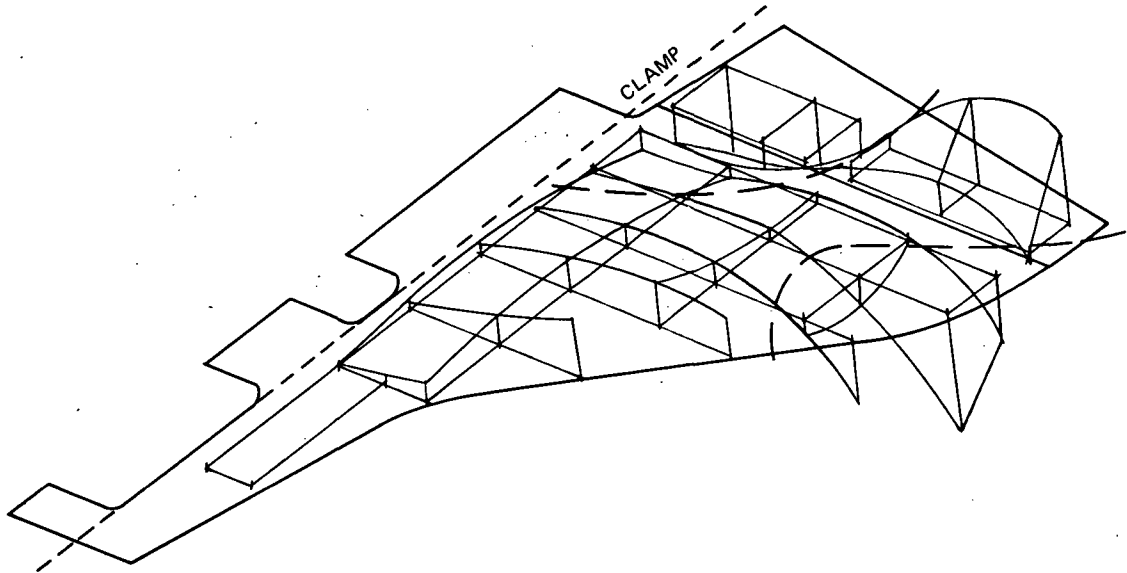
VIB NODE*	NORMALIZED DEFLECTION	VIB NODE	NORMALIZED DEFLECTION	VIB NODE	NORMALIZED DEFLECTION
1	-1.00	15	0.09	29	0
2	-0.54	16	0.09	30	0.07
3	-0.12	17	0.11	31	0
4	0.72	18	0.14	32	0
5	-0.59	19	-0.086	33	0.02
6	0.30	20	-0.26	34	0.04
7	-0.16	21	0.16	35	0.06
8	-0.23	22	0.25	36	0.02
9	0.03	23	0.23	37	-0.05
10	0.28	24	0.14	38	-0.17
11	0.76	25	0.03	39	-0.31
12	0.50	26	-0.108	40	-0.74
13	0.36	27	-0.22		
14	0.18	28	-0.55		

(d) 4th Mode   *See First Column of Table II

Figure 6.— Continued

(e) FREQUENCY = 1045.9 Hz — DAMPING COEFFICIENT = .021

THIRD BENDING MODE
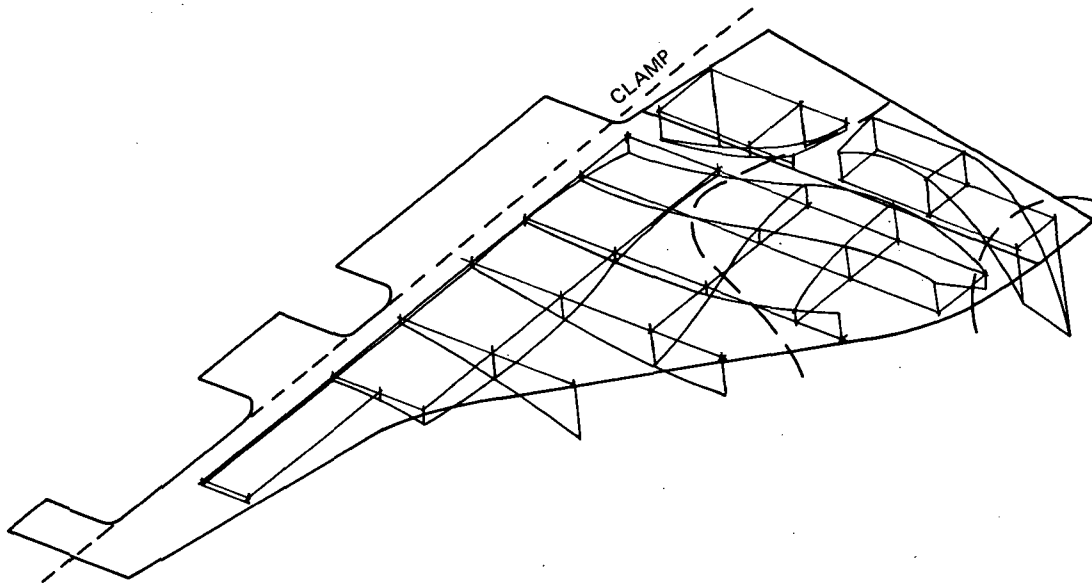
VIB NODE*	NORMALIZED DEFLECTION	VIB NODE	NORMALIZED DEFLECTION	VIB NODE	NORMALIZED DEFLECTION
1	−0.26	15	−0.12	29	0.03
2	0.13	16	−0.19	30	0.07
3	0.48	17	−0.23	31	0.03
4	1.00	18	−0.27	32	0.03
5	−0.20	19	−0.06	33	0.03
6	0.32	20	0.04	34	0.04
7	−0.09	21	0.15	35	0.04
8	−0.29	22	0.23	36	0.03
9	−0.32	23	0.18	37	0.04
10	−0.31	24	0.09	38	0.13
11	−0.27	25	0.03	39	0.23
12	0.48	26	0.04	40	0.65
13	0.31	27	0.11		
14	0.08	28	0.35		

(e) 5th Mode

*See First Column of Table II

Figure 6.— Concluded

f = 124.0 Hz

f = 242.9 Hz
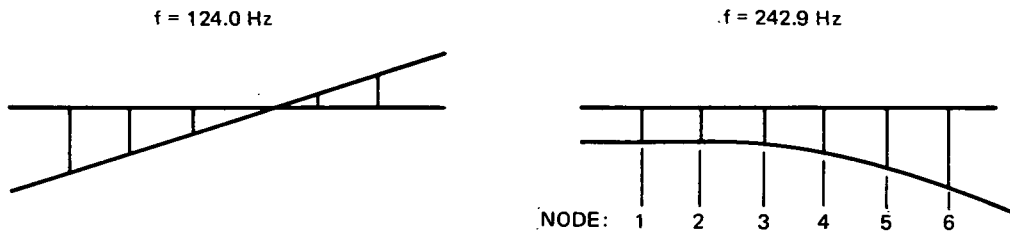
NODE: 1   2   3   4   5   6

NODE NO.	1	2	3	4	5	6
MEASURED DEFLECTIONS FOR MODE 1	.78	.55	.32	.09	−.18	−.40
MEASURED DEFLECTIONS FOR MODE 2	.41	.43	.46	.53	.75	1.00

(a) Nominal Flexures

f = 222.0 Hz

f = 438.0 Hz
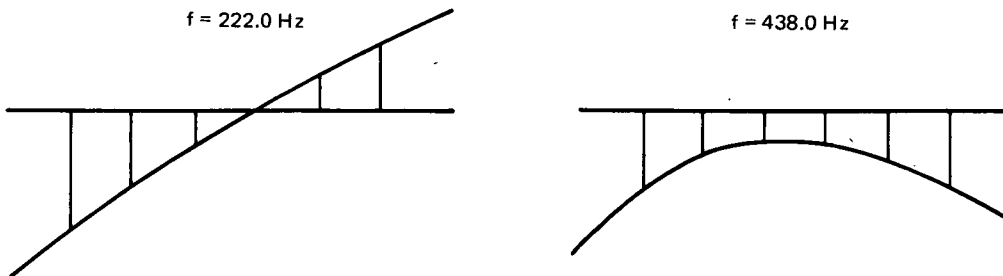
NODE NO.	1	2	3	4	5	6
MEASURED DEFLECTIONS FOR MODE 1	1.5	.89	.39	.07	−.34	−.80
MEASURED DEFLECTIONS FOR MODE 2	1.0	.50	.40	.40	.60	.90

(b) Tuned Flexures

Figure 7.— Mode Shape Data, 1/80th-Scale Rigid SRB on Flexible
Attachments
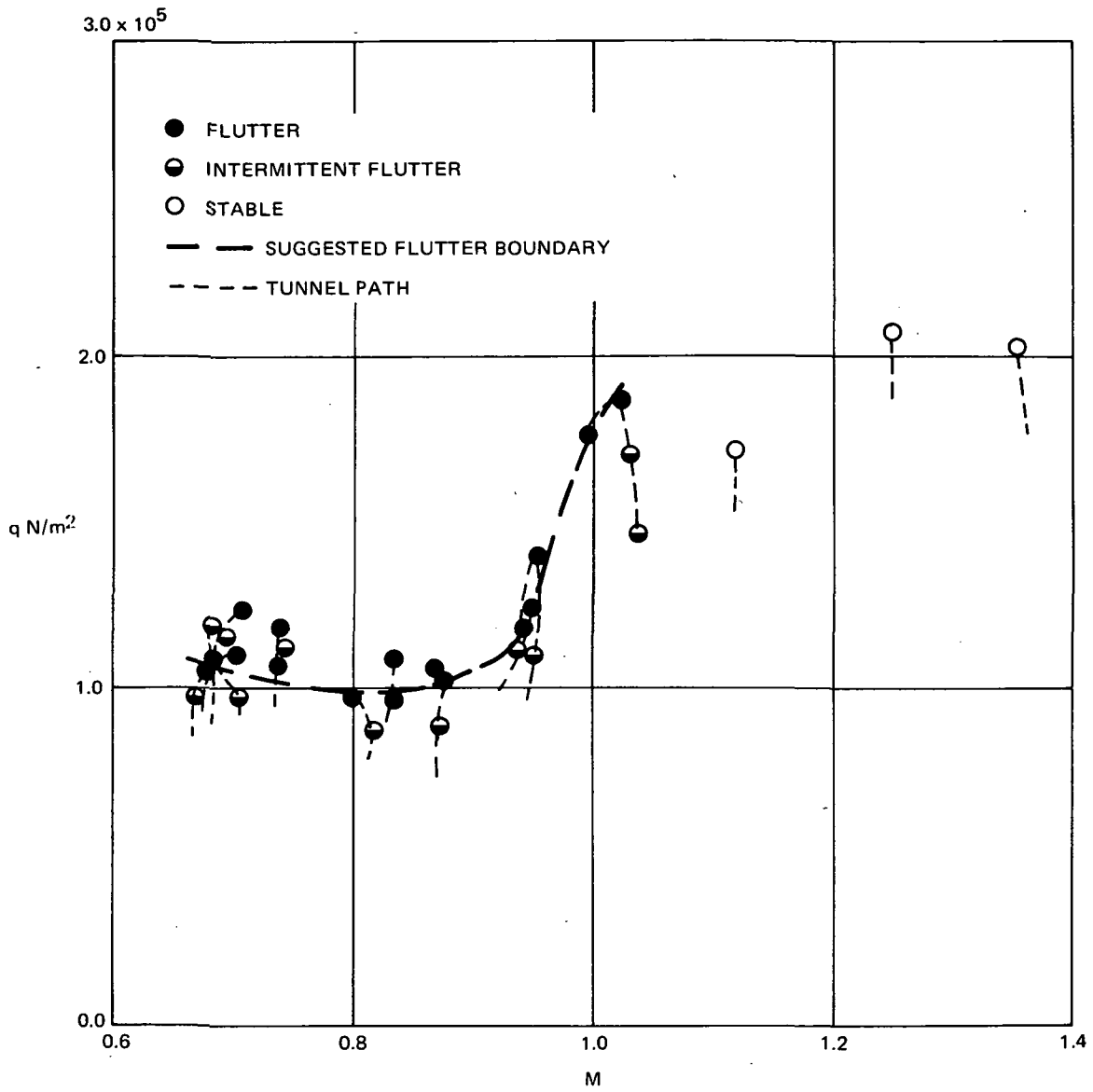
Figure 8.— Variation of Measured Dynamic Pressure with Mach Number
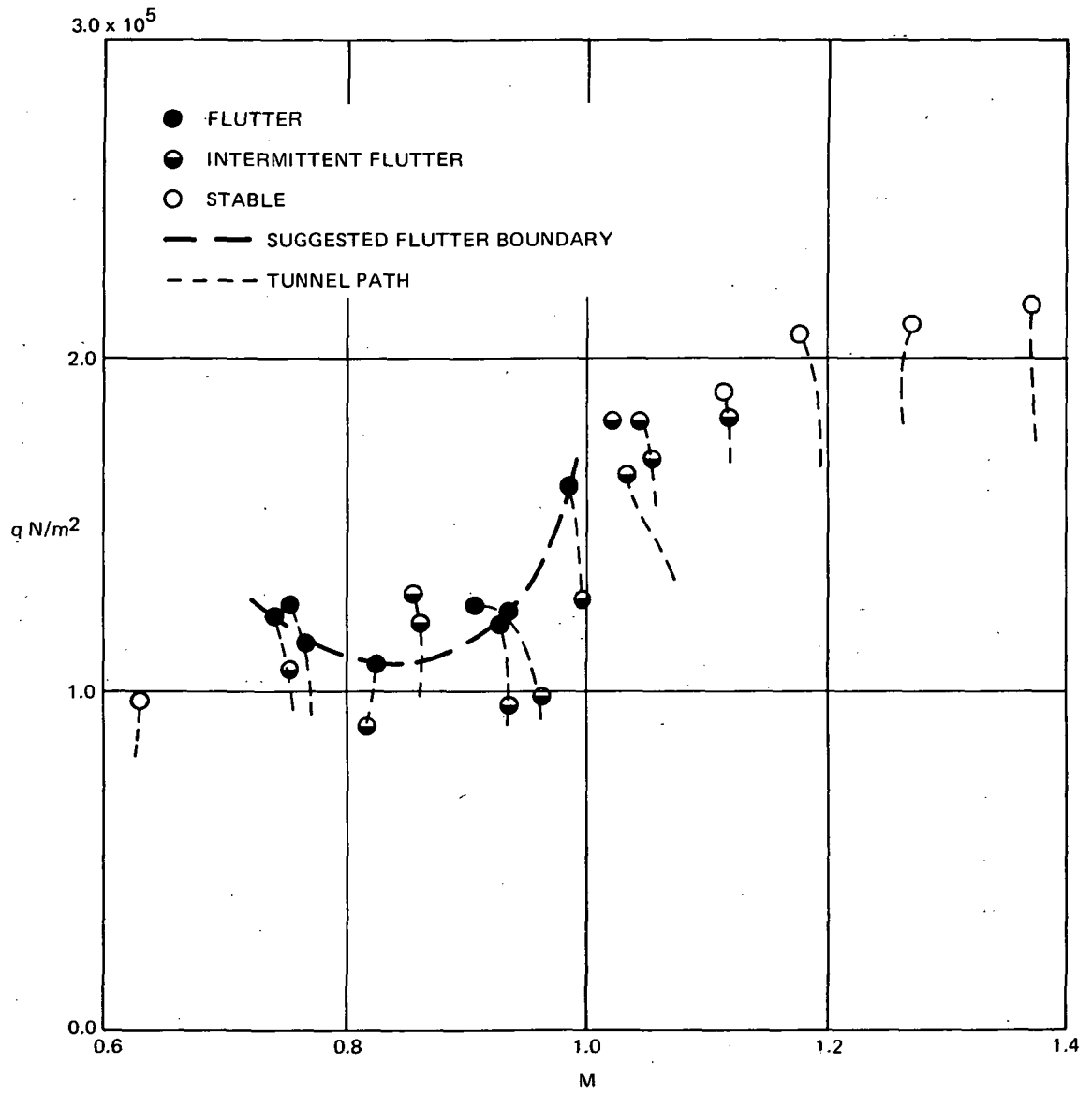
(b) Orbiter

Figure 8.— Continued
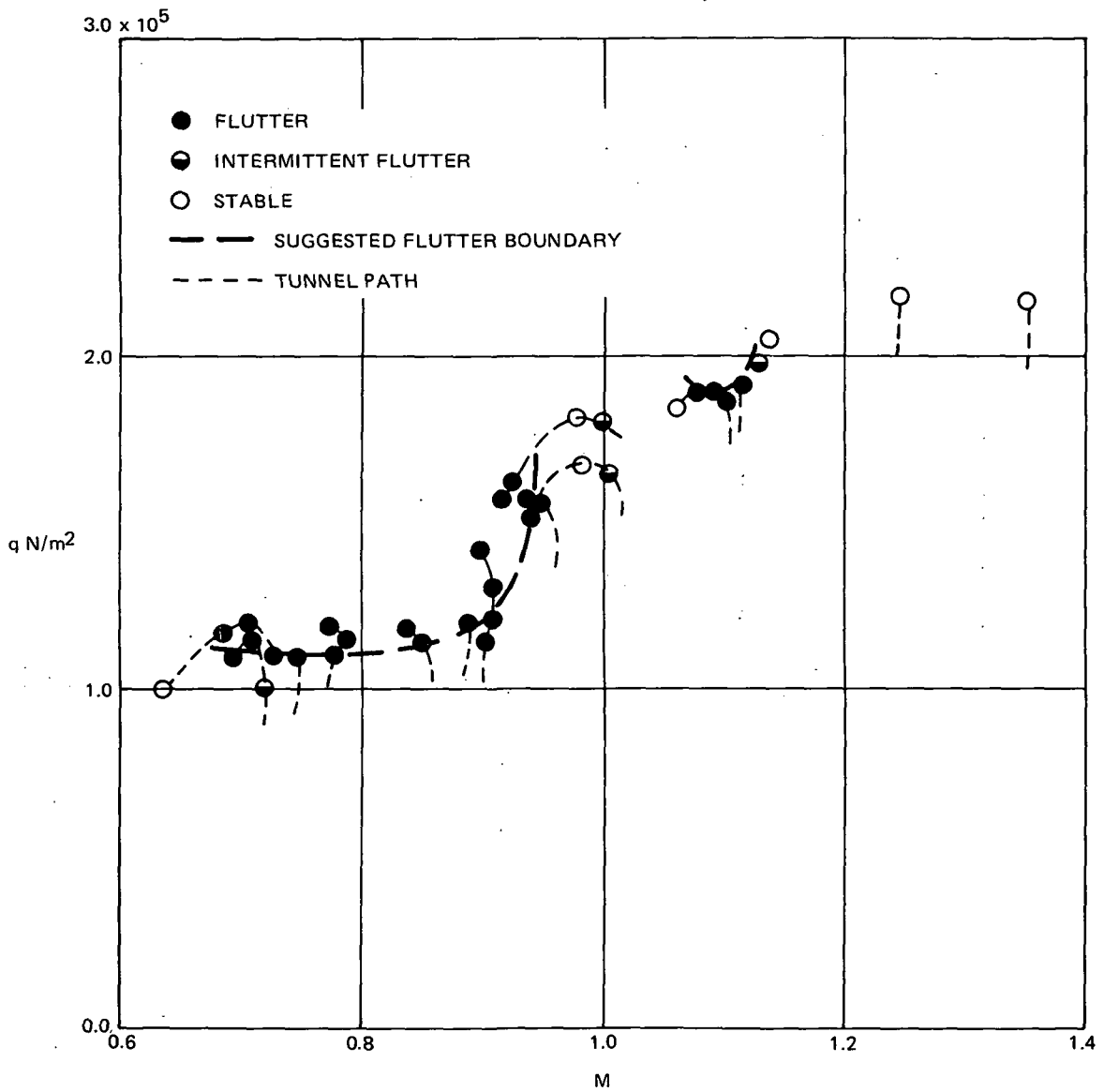
(c) Orbiter/External Tank

Figure 8.— Continued

3.0×10^5

● FLUTTER

◑ INTERRMITTENT FLUTTER

○ STABLE

— — SUGGESTED FLUTTER BOUNDARY

– – – – TUNNEL PATH

2.0

$q \ N/m^2$

1.0

0.0

0.6   0.8   1.0   1.2   1.4

M
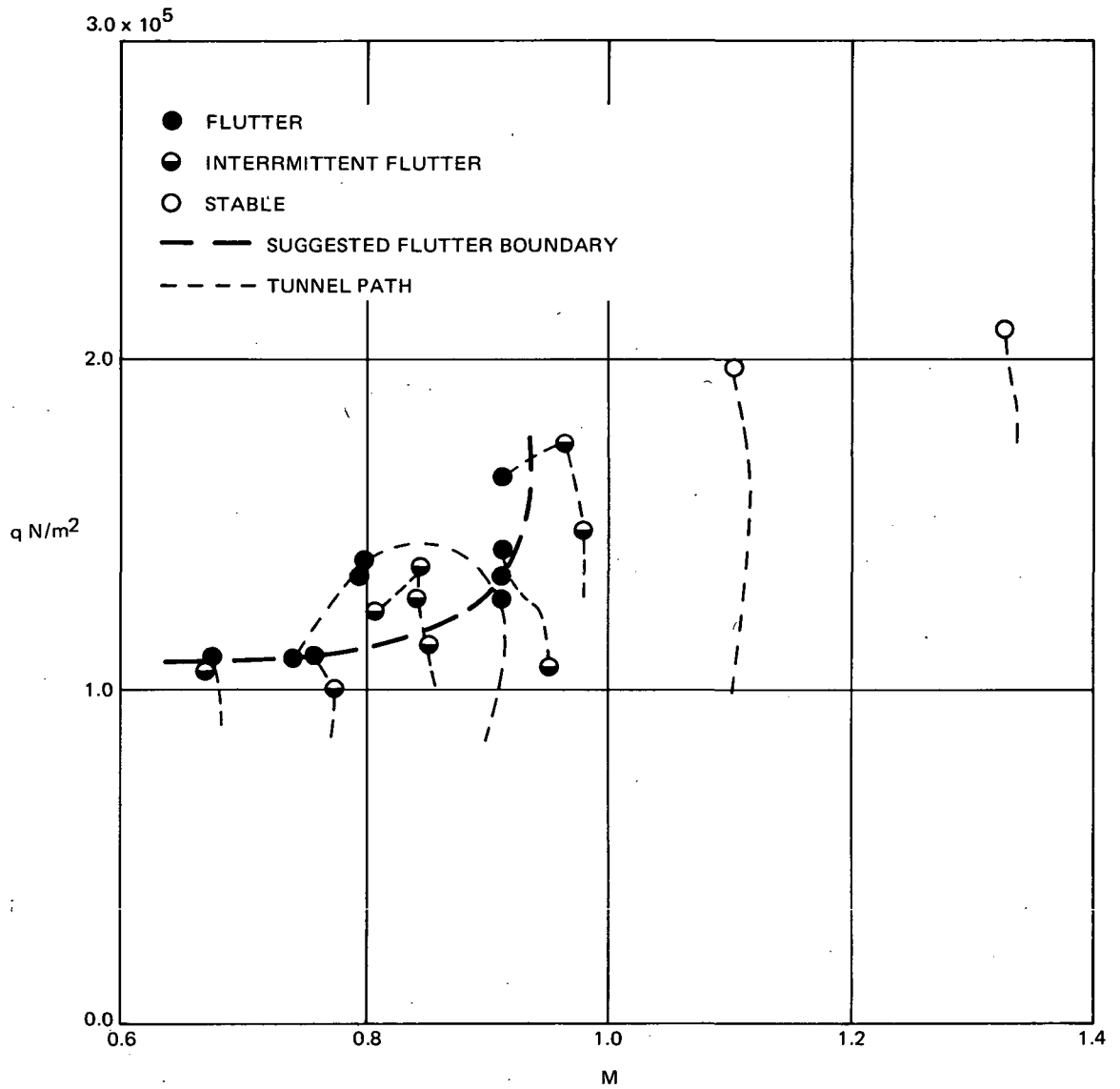
(d) Shuttle, Rigid SRB Attachments
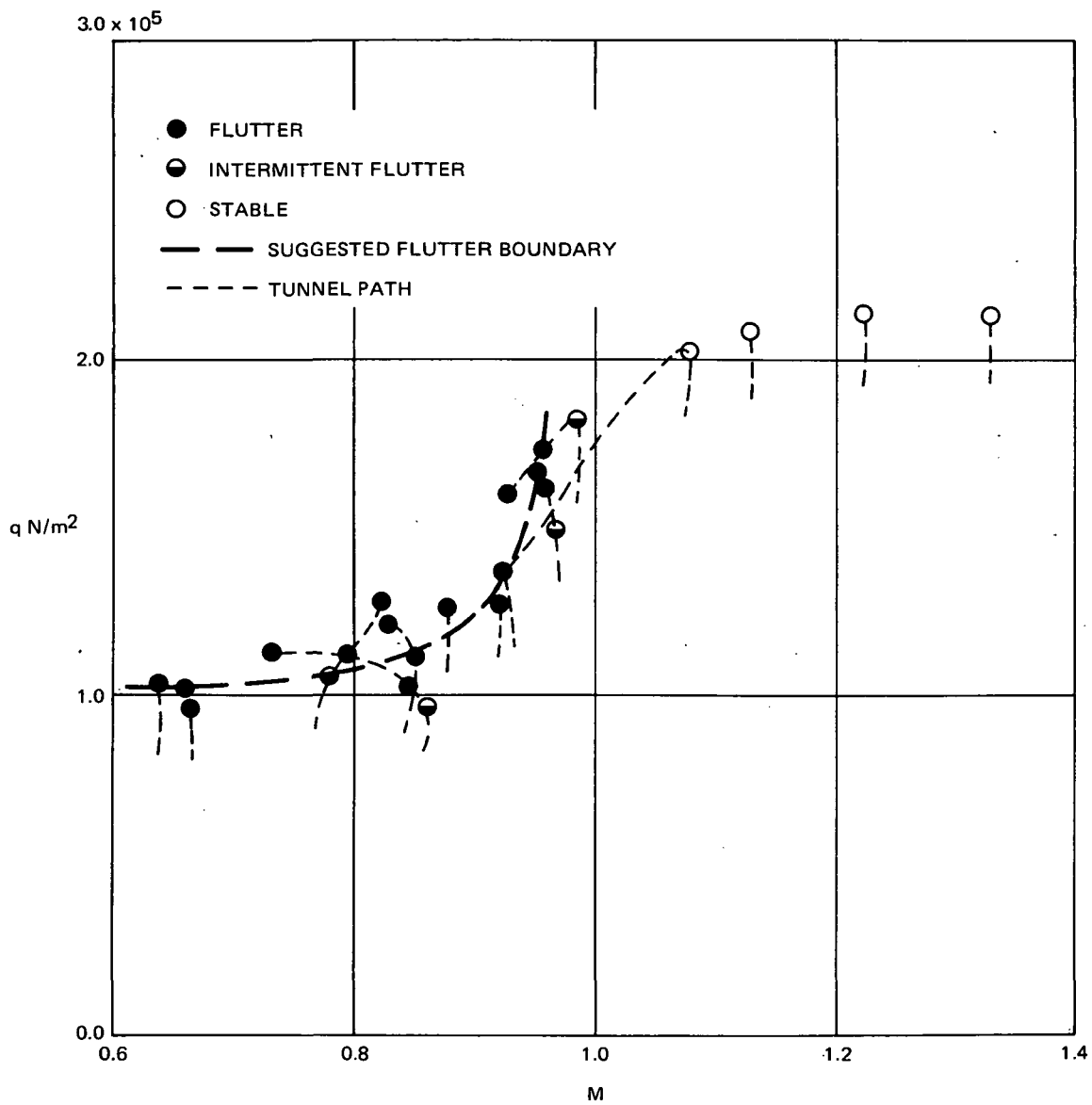
Figure 8.— Continued

(e) Shuttle, Nominal SRB Attachments

Figure 8.— Continued
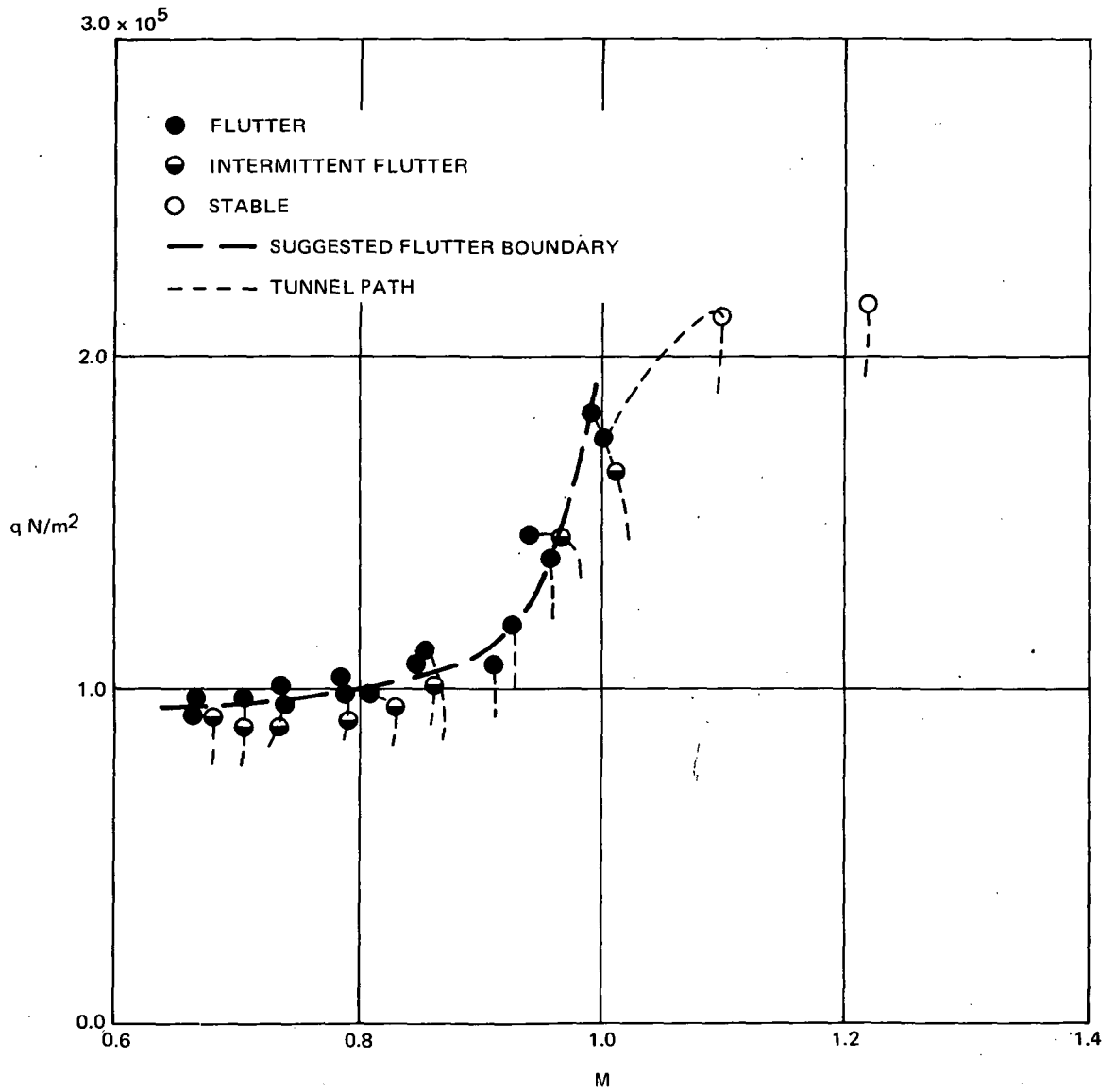
(f) Shuttle, Tuned SRB Attachments

Figure 8.— Concluded
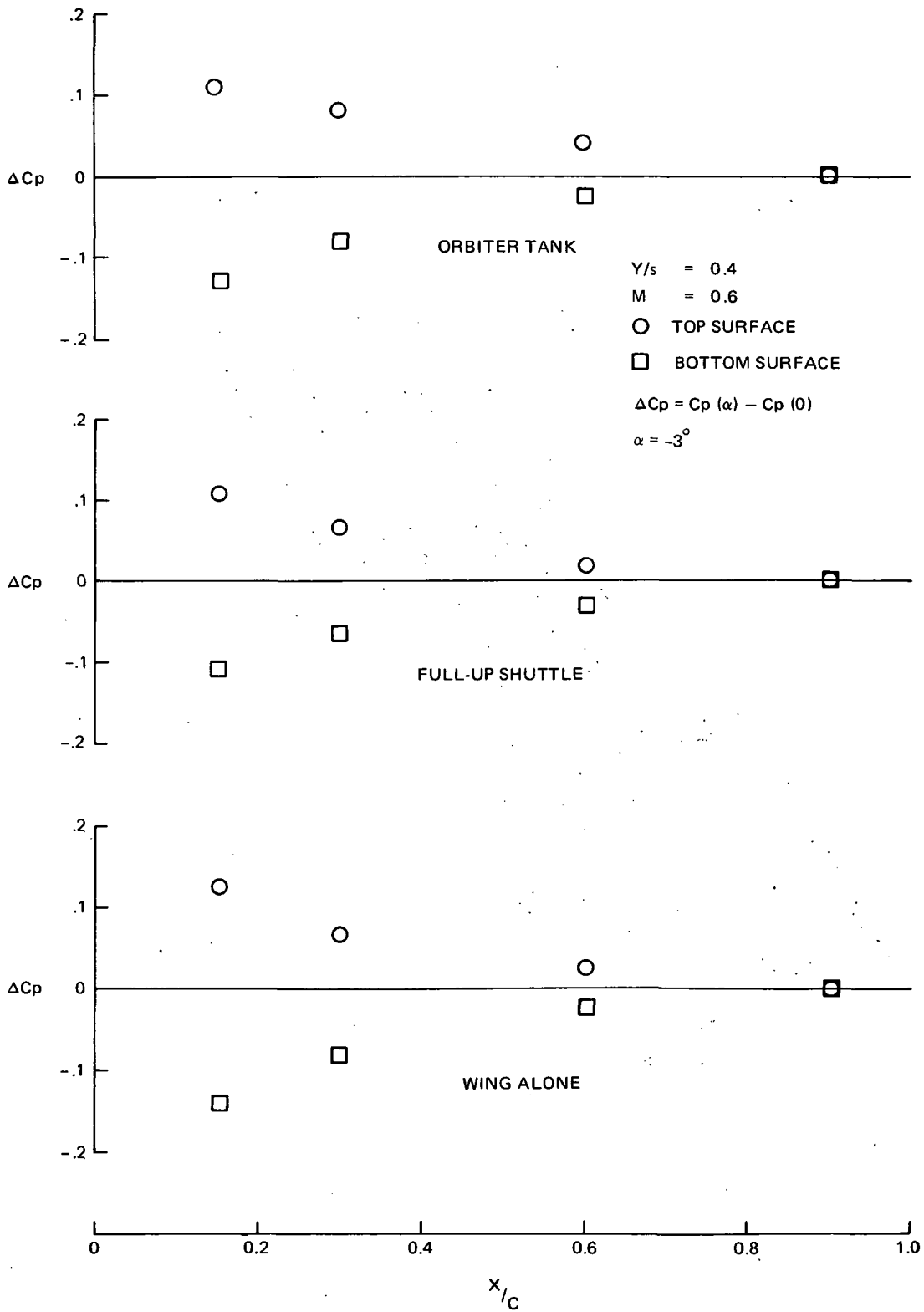
Figure 9.— Measured Pressures on Wing Surfaces Due to Incidence
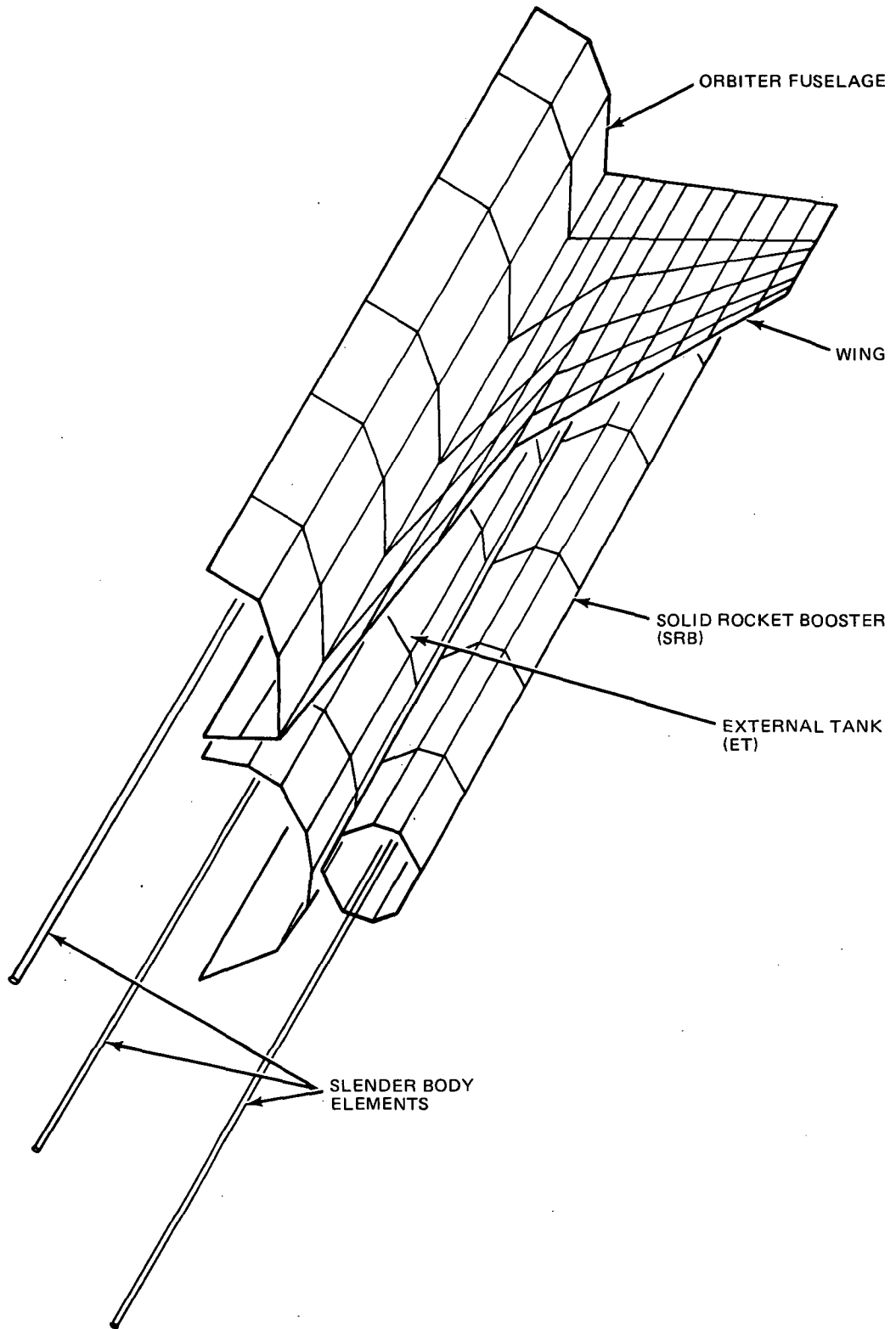
Figure 10.— Aerodynamic Idealization of Space Shuttle

GRID 1

Y/S = 0.25
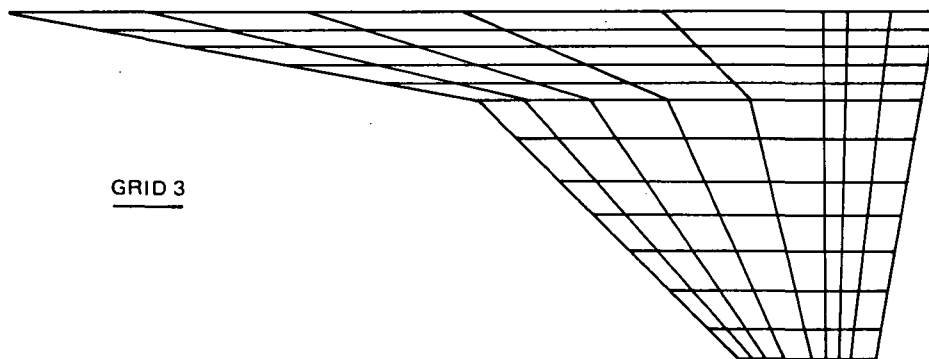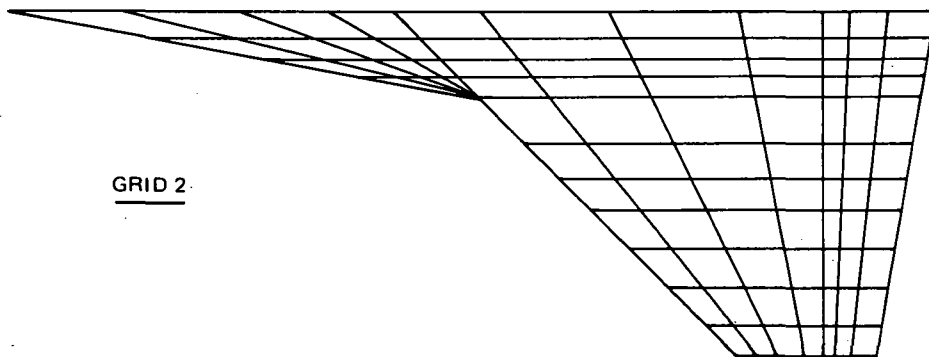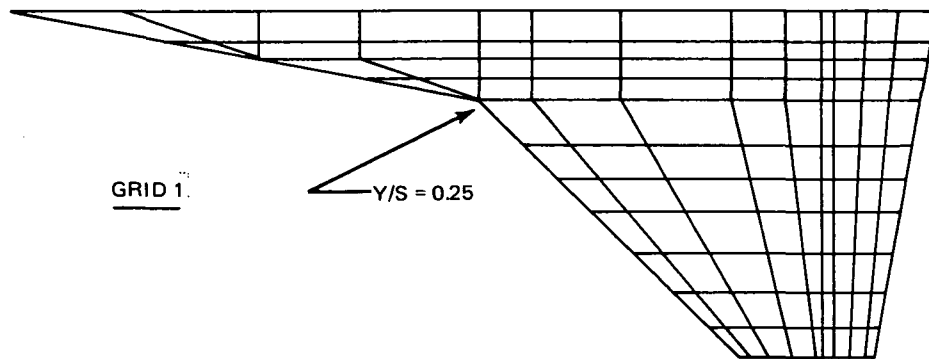
GRID 2

GRID 3

VARIATIONS IN GRID 3

	GRID NO.	3.0	3.1	3.2	3.3	3.4	3.5	3.6	3.7	3.8
NO. OF BOXES	CHORDWISE	8	7	10	10	8	6	8	8	8
	SPANWISE (INNER PANEL)	5	5	5	6	3	3	6	5	5
	SPANWISE (OUTER PANEL)	7	7	7	7	7	7	7	5	9

Figure 11.— Aerodynamic Grids Studied on Orbiter Wing
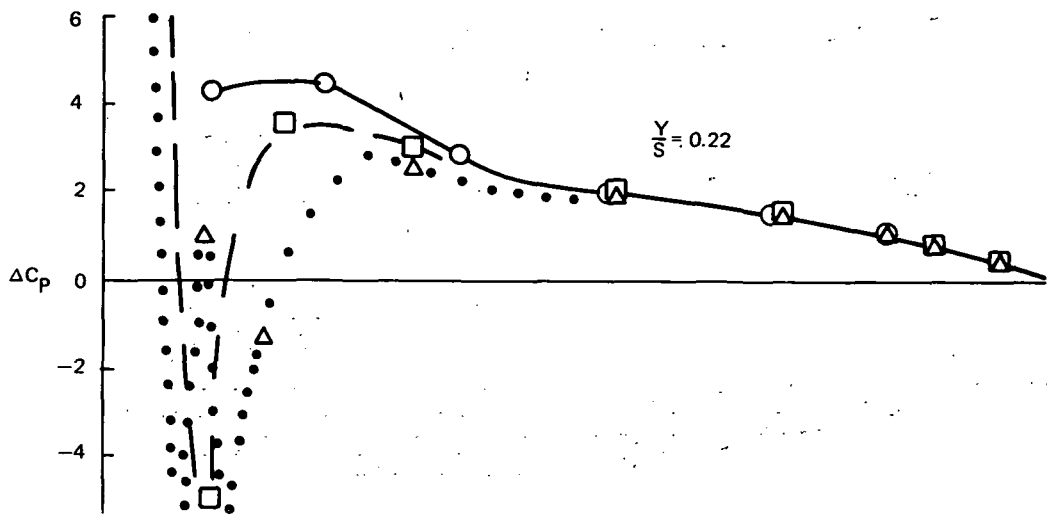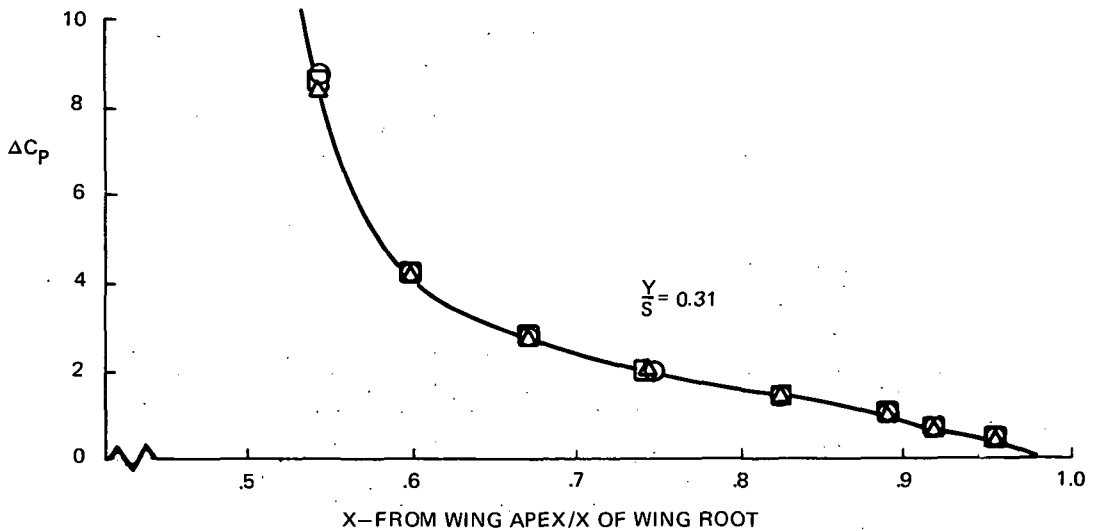
Figure 12.— Effect of Misaligned Aerodynamic Grid on Lift and Pressure Distributions on the Wing.
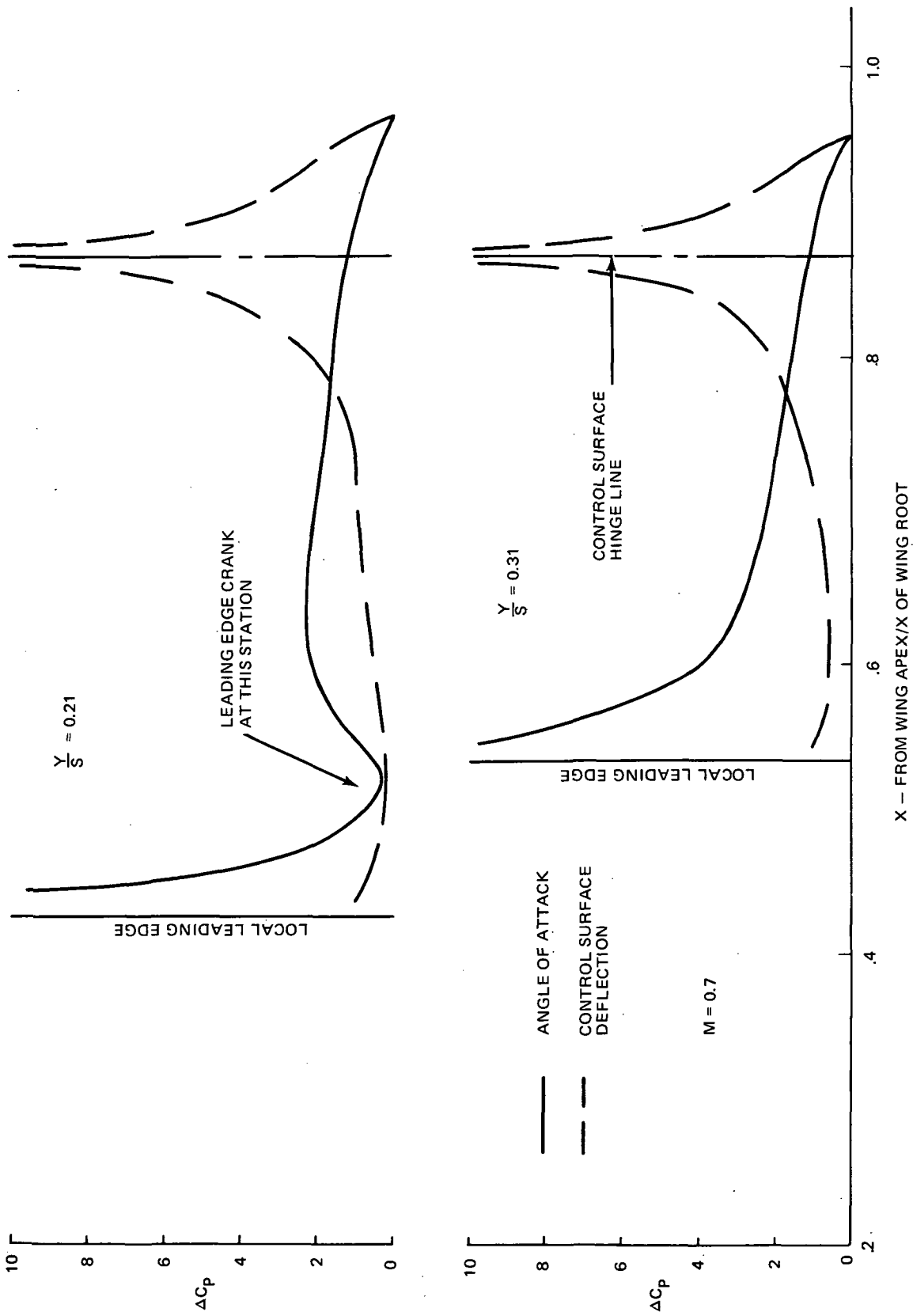
Figure 13.— Pressure Distributions on the Orbiter Wing with the Preferred Aerodynamic Grid

49

k = 0.07
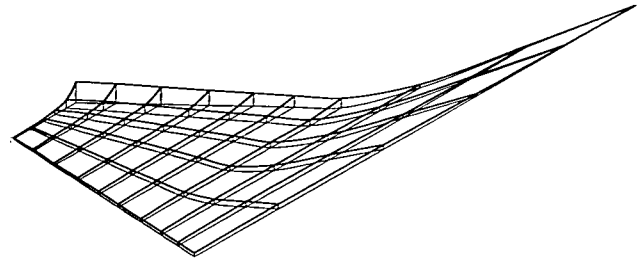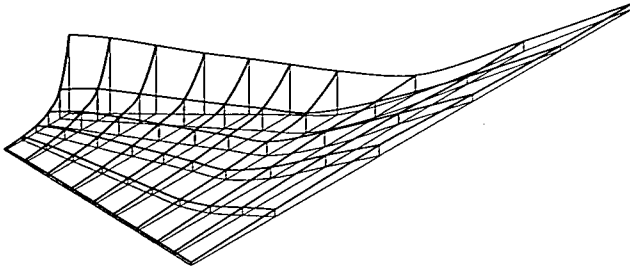
k = 0.12
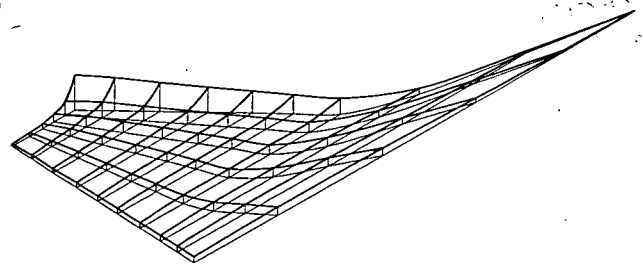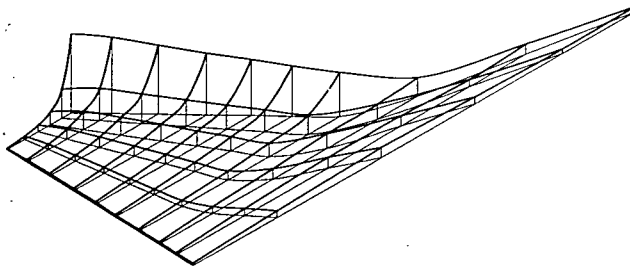
k = 0.26
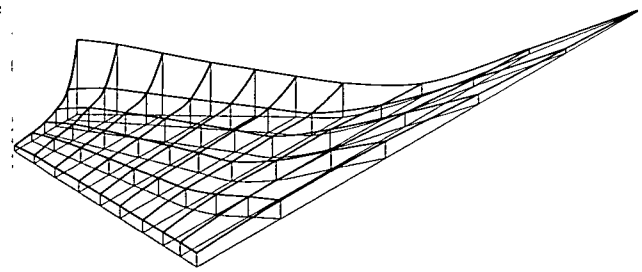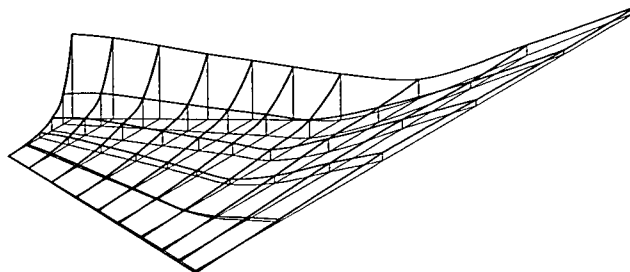
k = 0.61
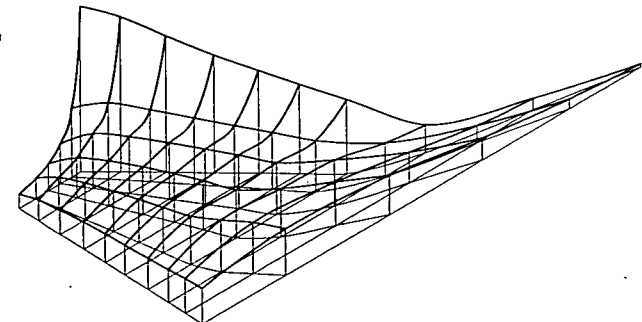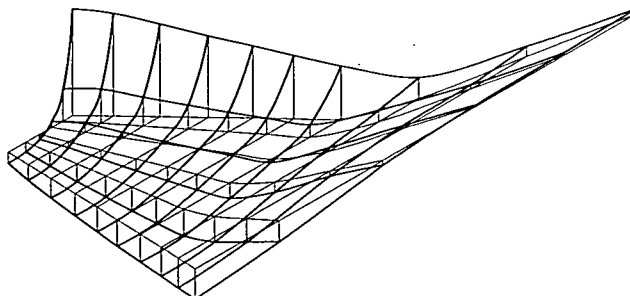
Figure 14. - Oscillatory Pressures on Isolated Wing at M = 0.6 for Pitch About the Apex
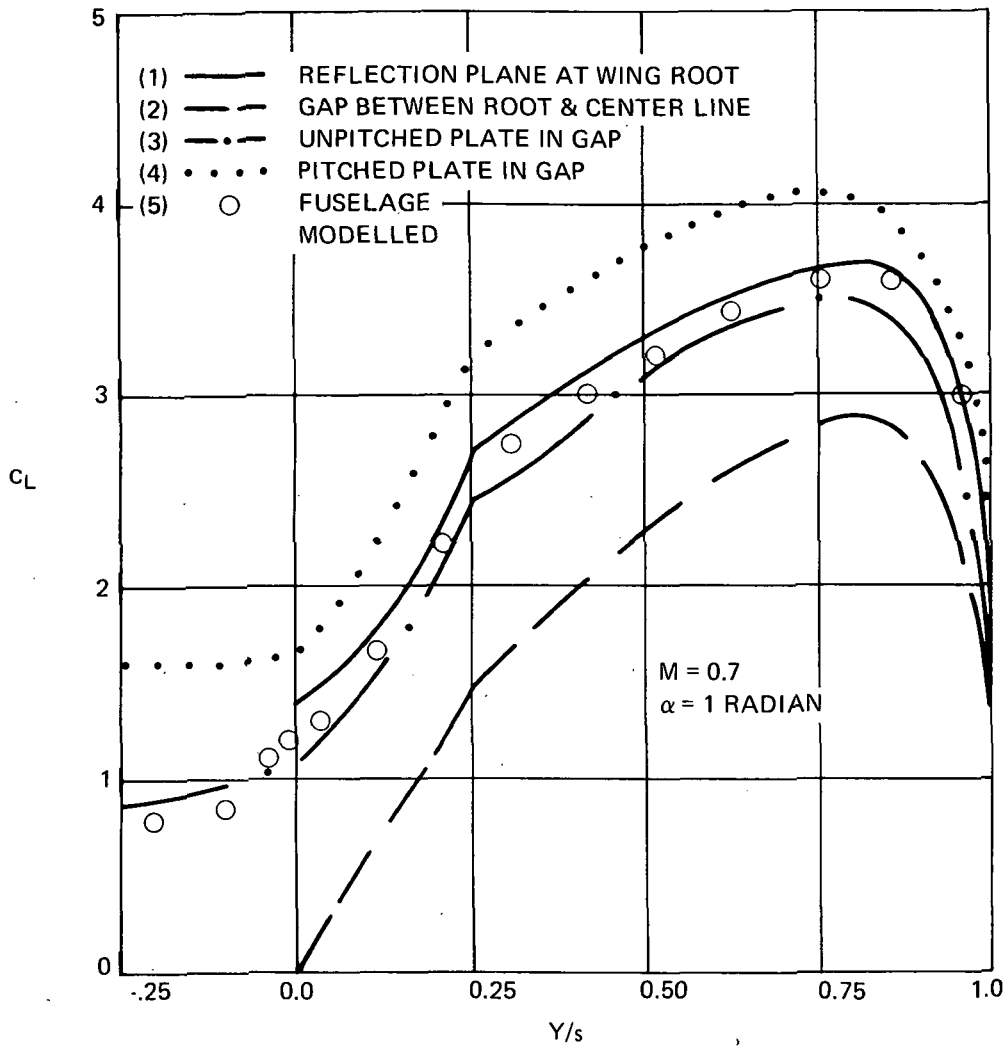
Figure 15. - Effect of Wing Root Condition on Spanwise Lift Distribution.
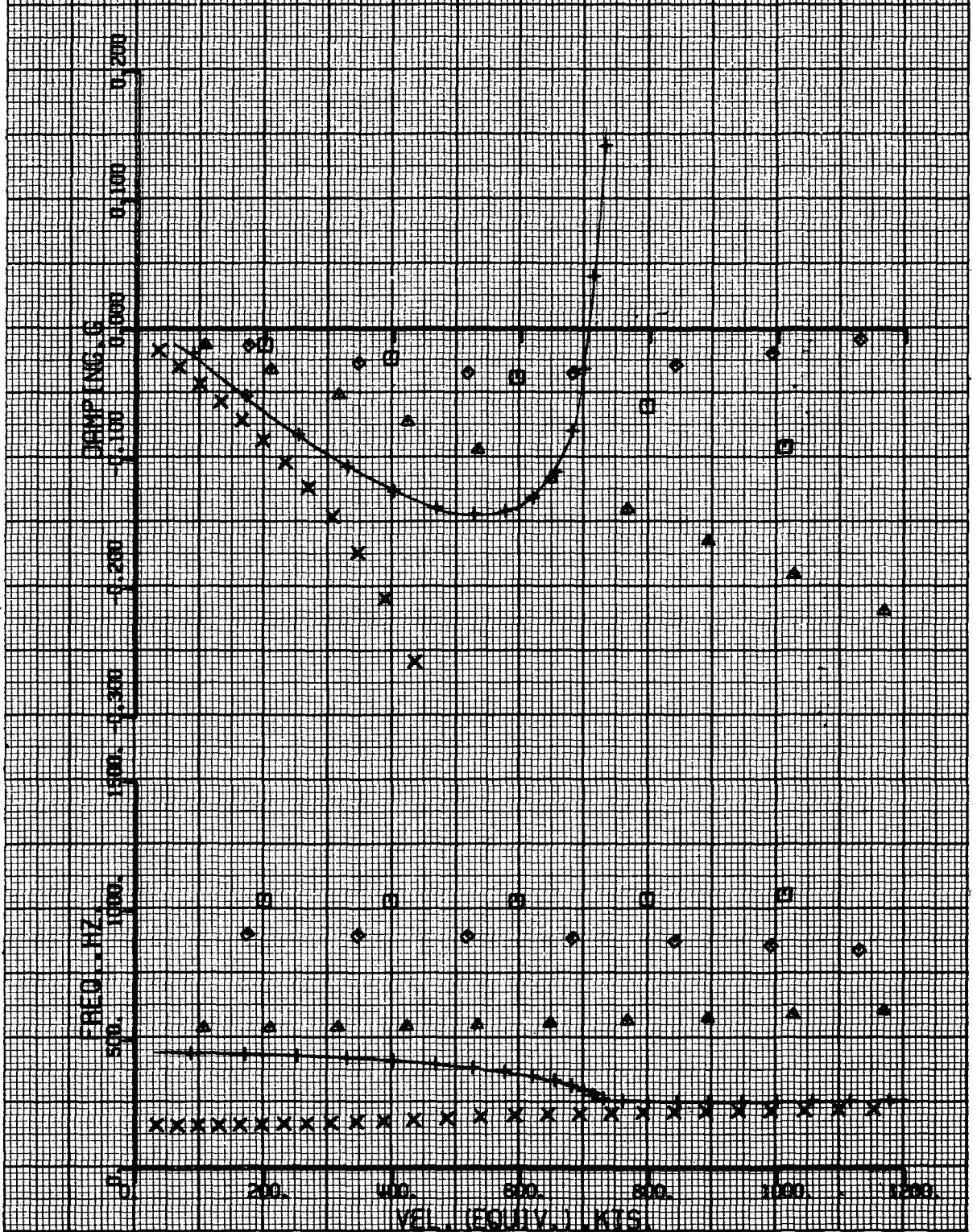
Figure 16. — Damping and Frequency as a Function of Airspeed for the Isolated 1/80th-Scale Wing Endplated at its Root

52
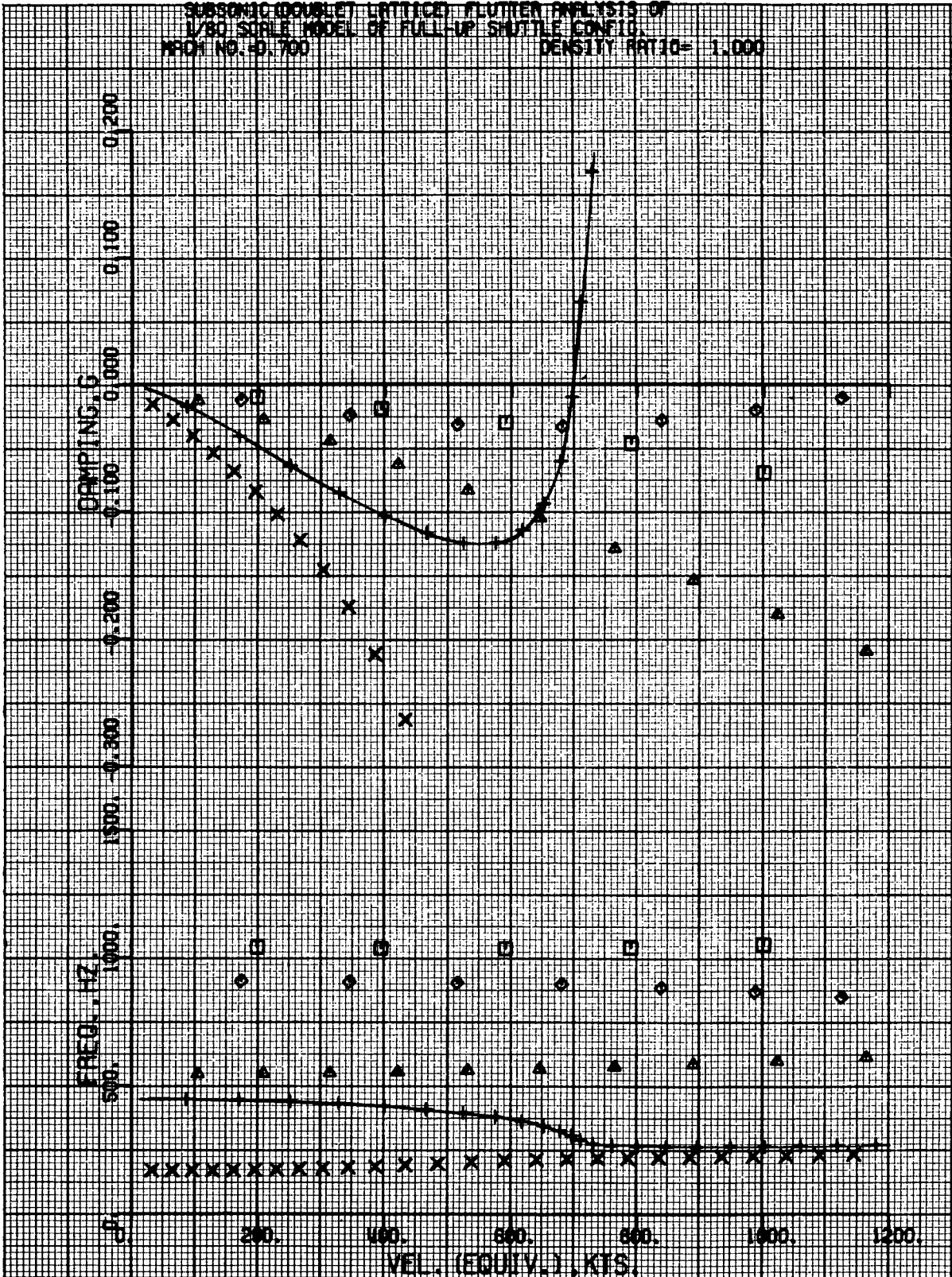
Figure 17.— Damping and Frequency as a Function of Airspeed for the 1/80th-Scale Wing in the Presence of the Other Shuttle Components (Fuselage, External Tank and Solid Rocket Booster)
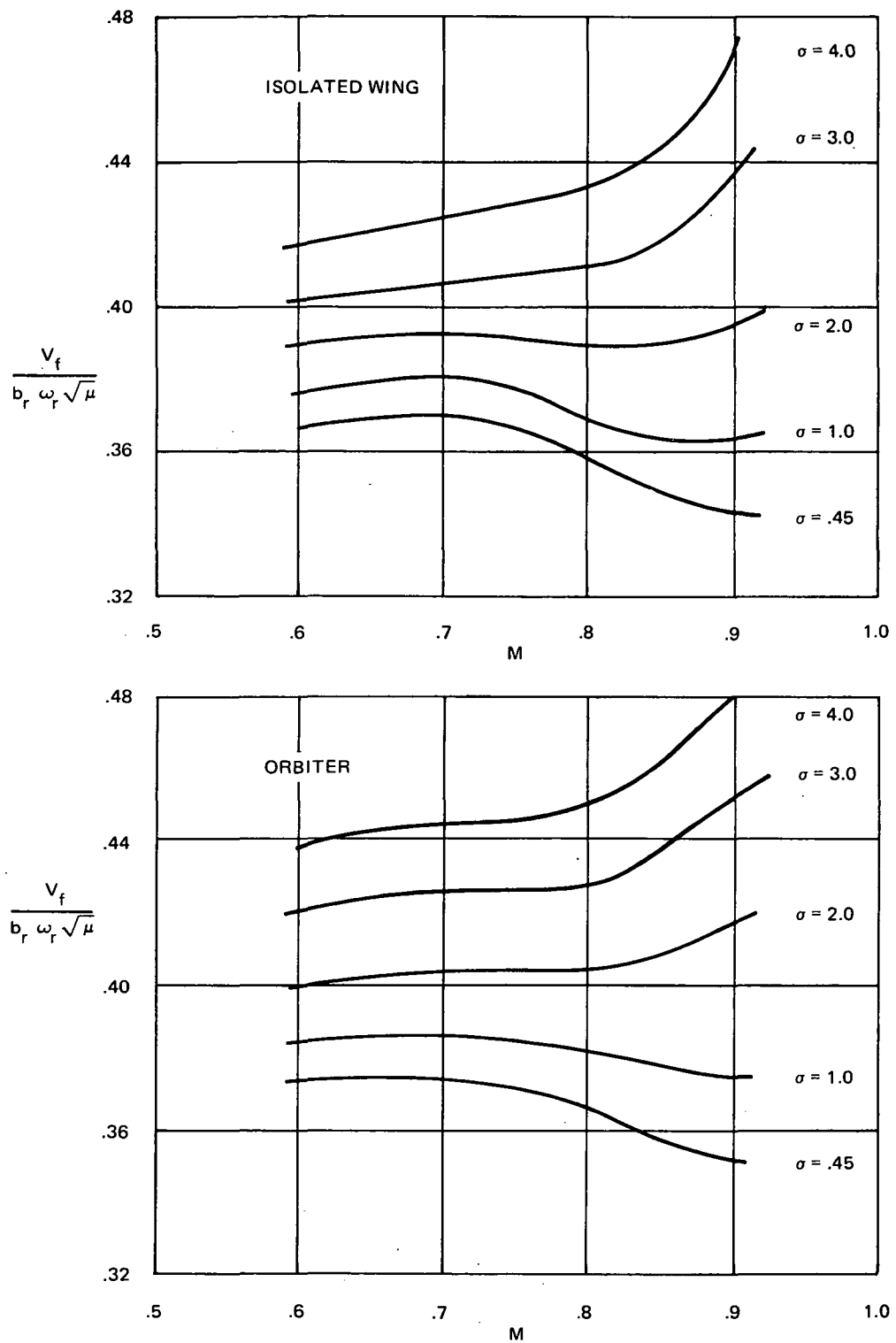
Figure 18.— Calculated Flutter Speed Indices for the Isolated 1/80th-Scale Wing and the Wing in the Presence of the Orbiter Fuselage as Functions of Mach Number and Air Density
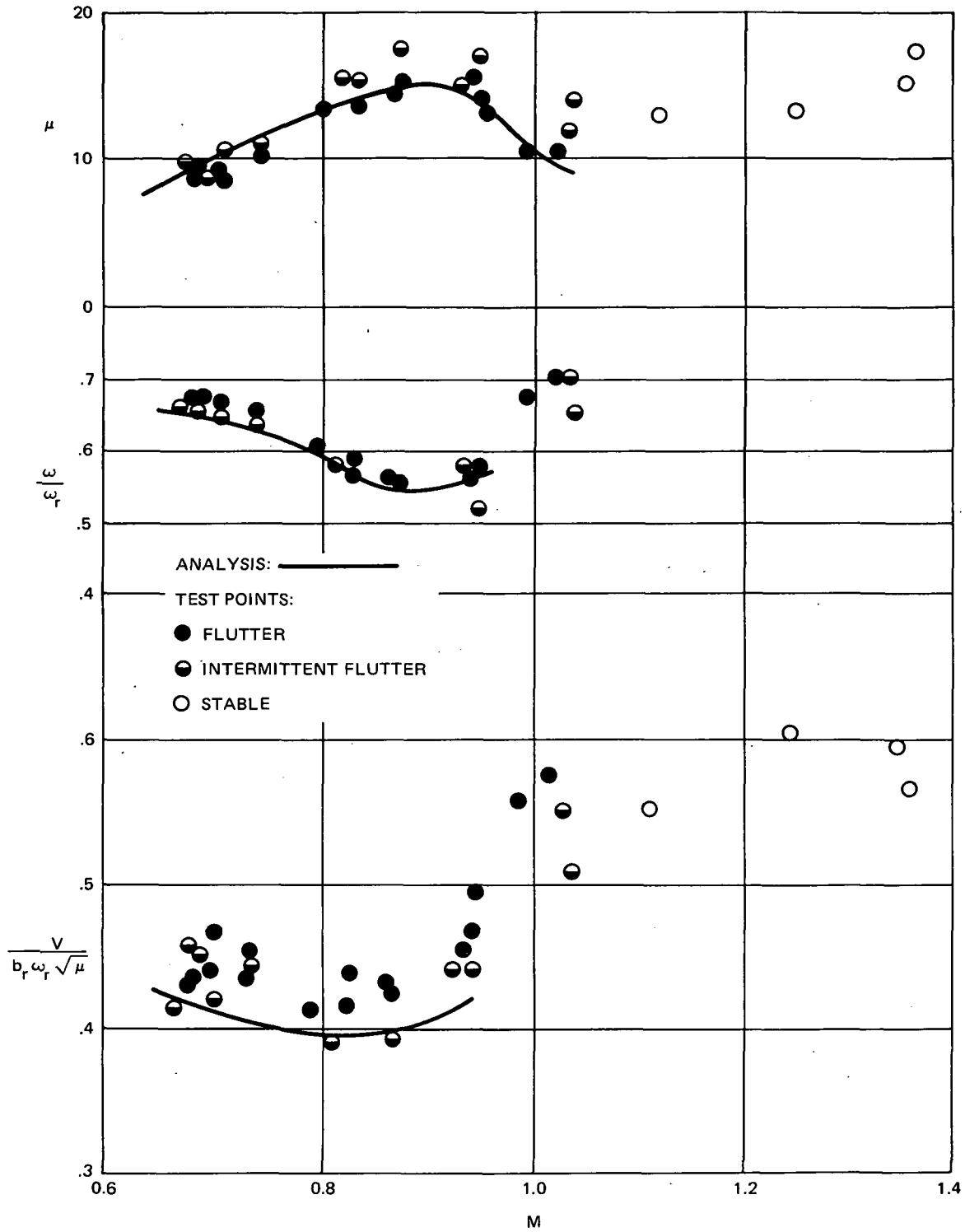
(a) Isolated Wing

Figure 19.— Variation of Mass Density Ratio, Flutter Frequency Index and Flutter Speed Index with Mach Number for the 1/80th-Scale Shuttle Model
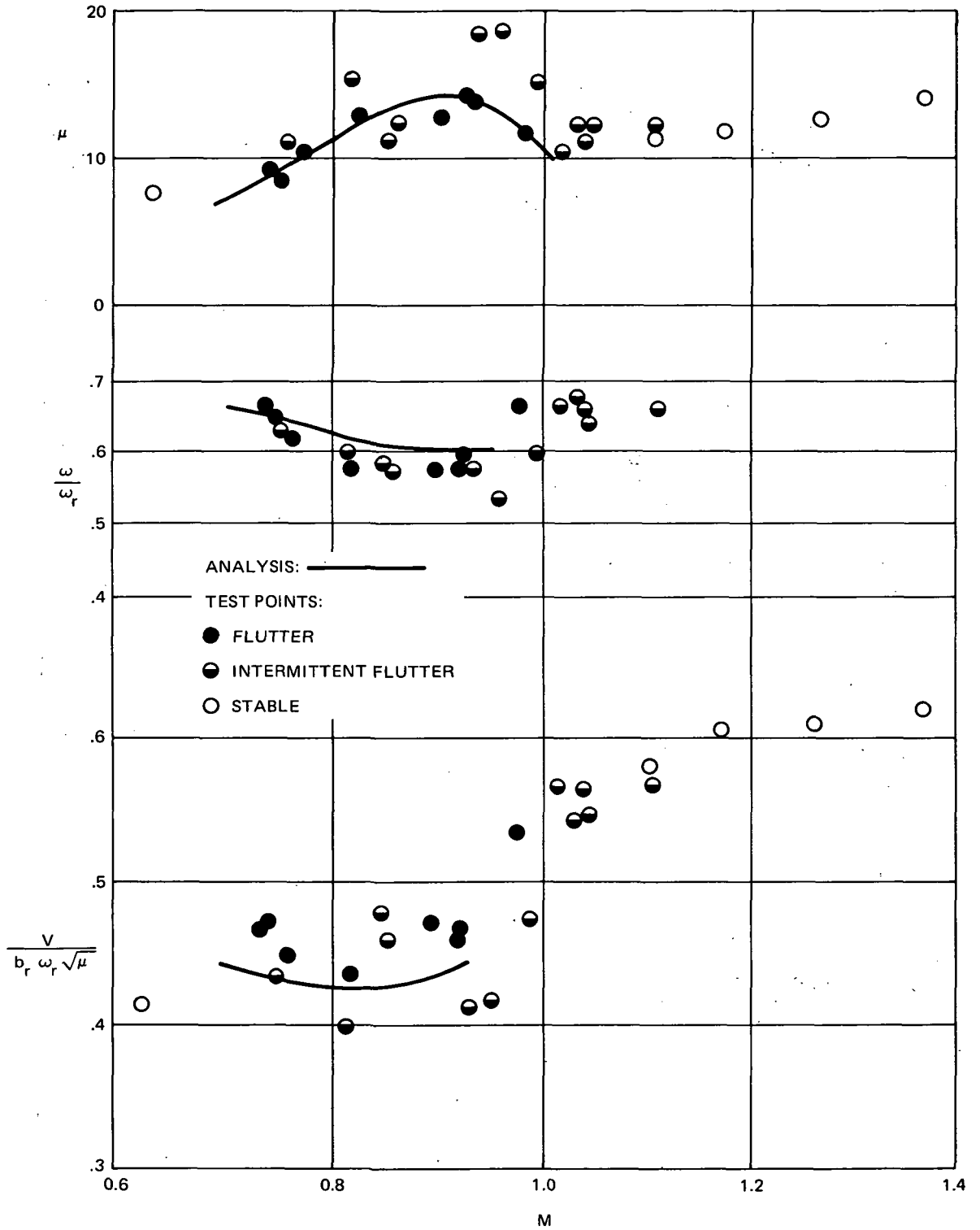
(b) Orbiter

Figure 19.— Continued
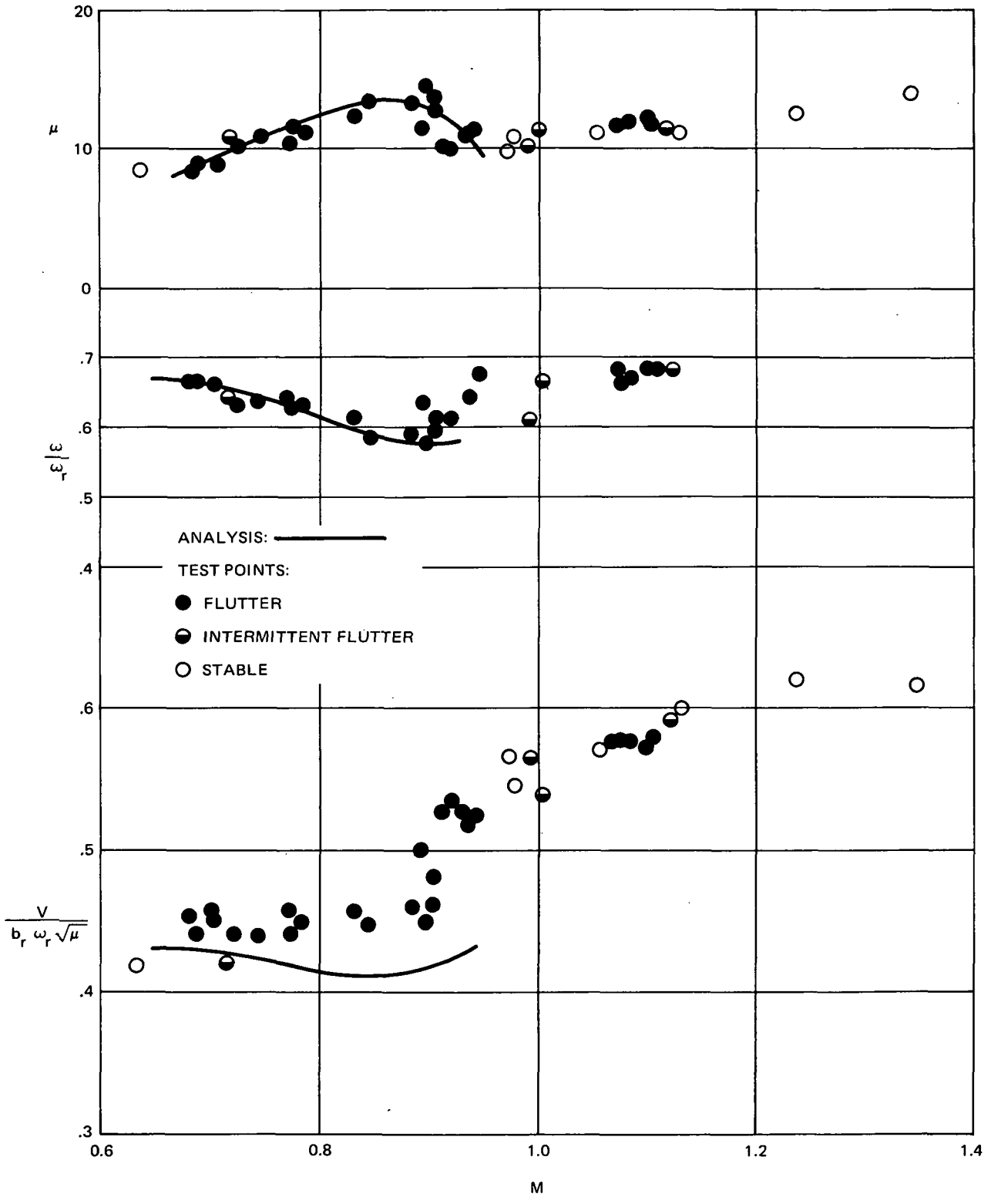
(c) Orbiter/External Tank

Figure 19.— Continued

(d) Shuttle With Rigid Attachments

Figure 19.— Continued
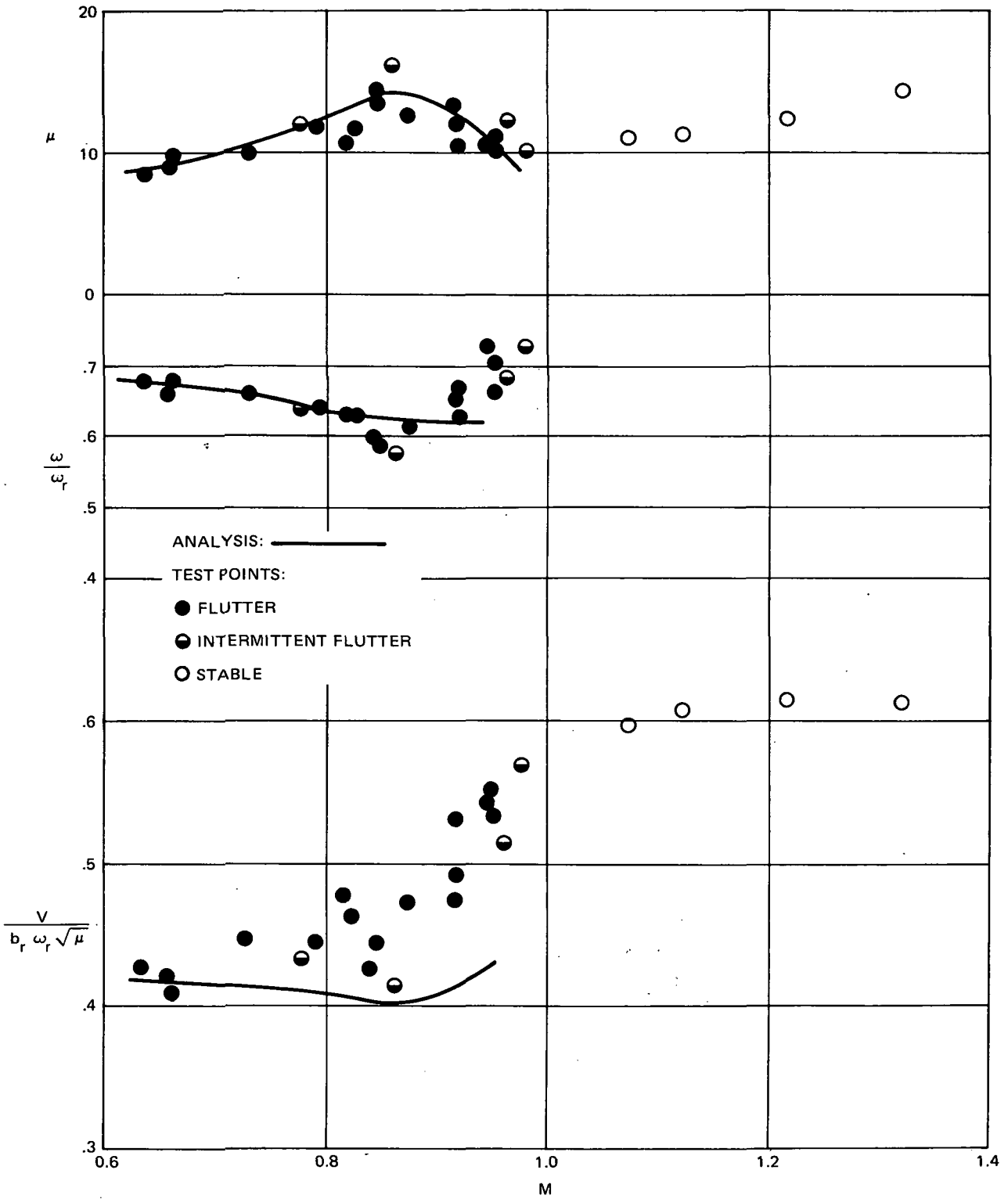
(e) Shuttle With Nominal Attachments

Figure 19.— Continued

20

μ

10

0

.7

.6

$\dfrac{\omega}{\omega_r}$

.5

.4

ANALYSIS: ———

TEST POINTS:

● FLUTTER

◐ INTERMITTENT FLUTTER

○ STABLE

.6

.5

$\dfrac{V}{b_r\, \omega_r\, \sqrt{\mu}}$

.4

.3

0.6   0.8   1.0   1.2   1.4

M
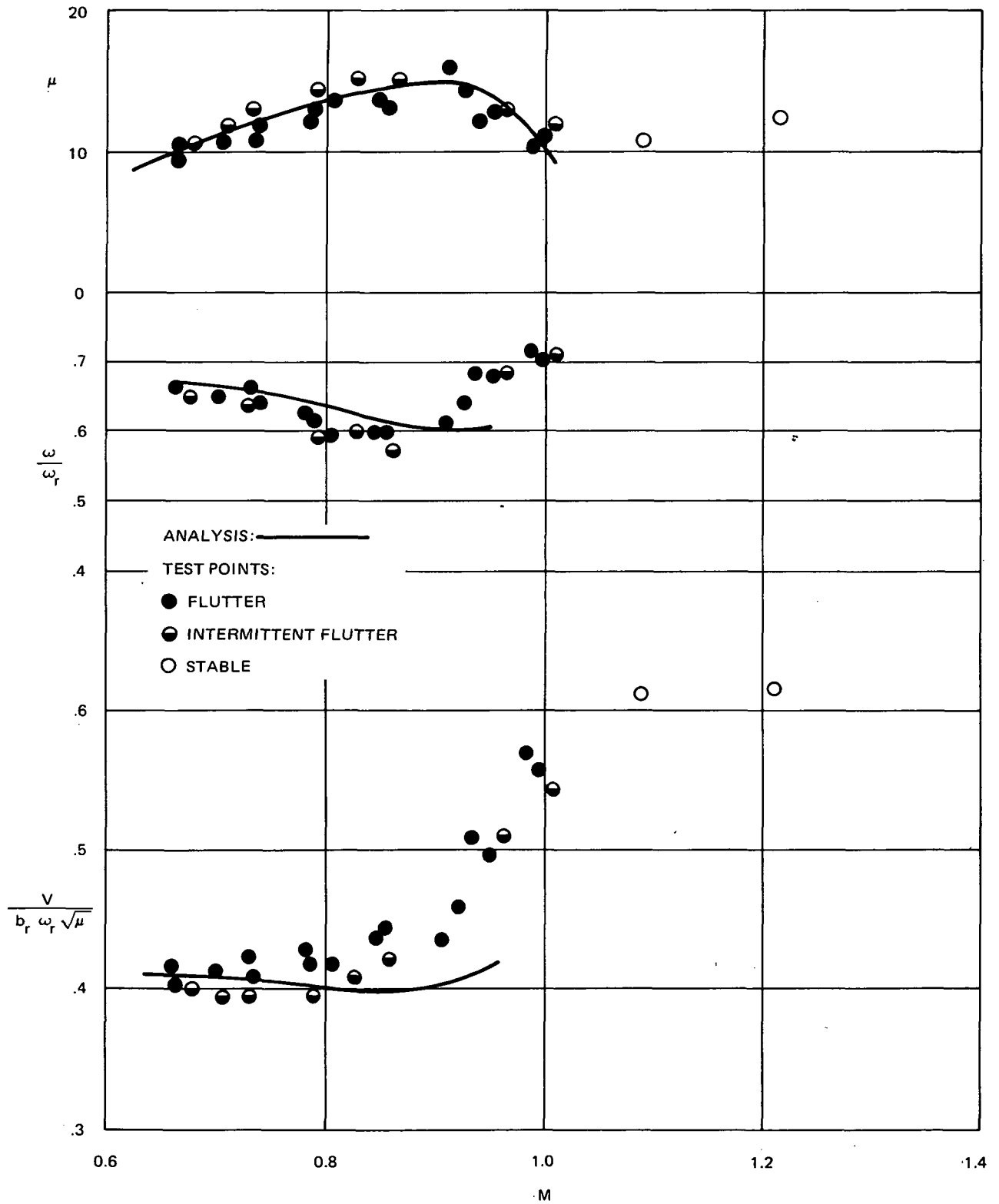
(f) Shuttle with Tuned Attachments

Figure 19.— Concluded
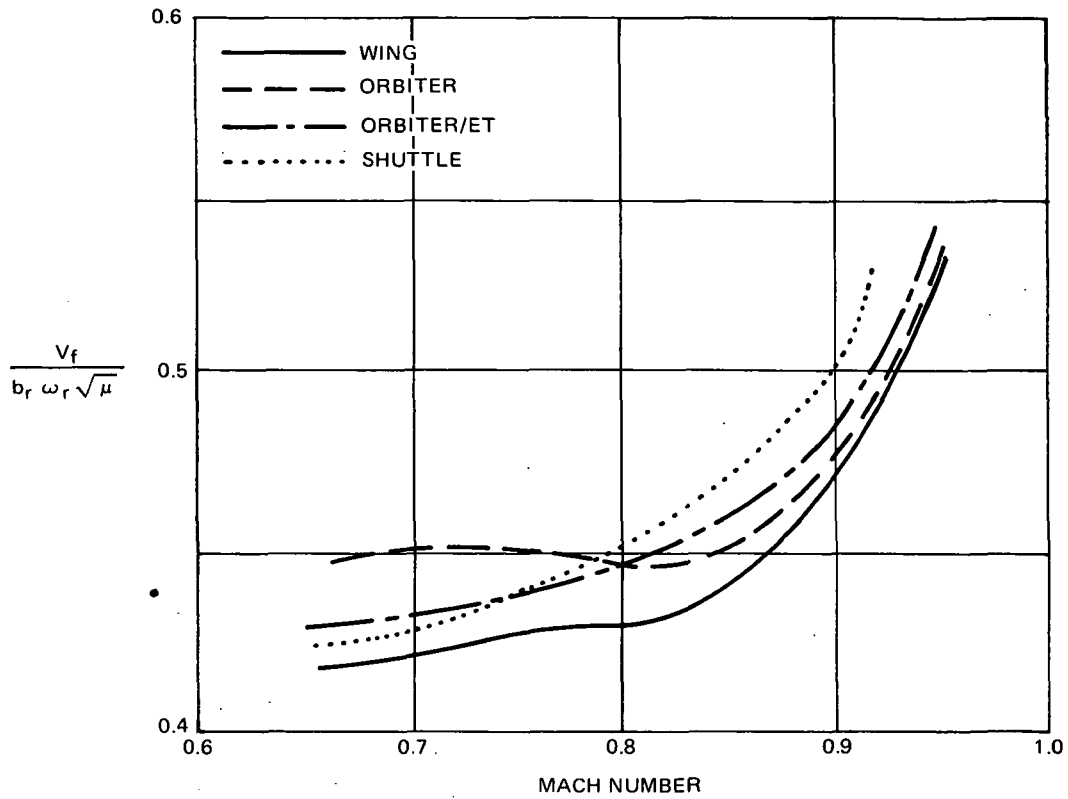
Figure 20.– Test Flutter Boundaries Adjusted to $\sigma = 3.0$
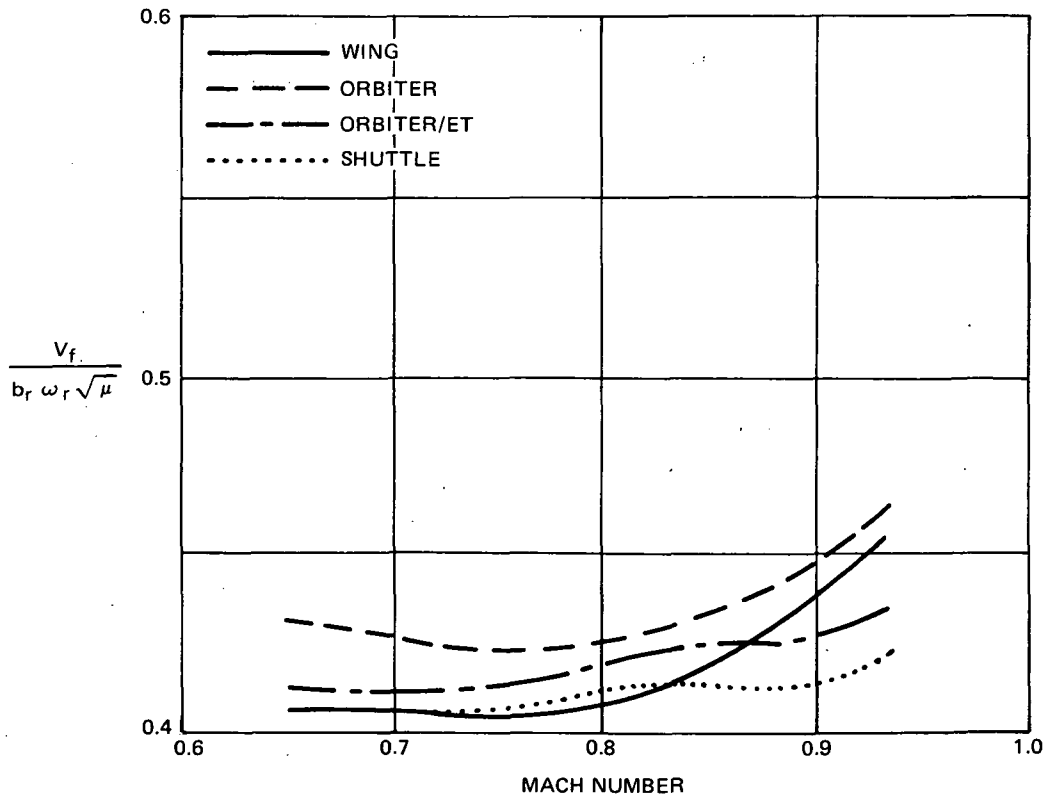
Figure 21.– Analytical Flutter Boundaries at $\sigma = 3.0$

61
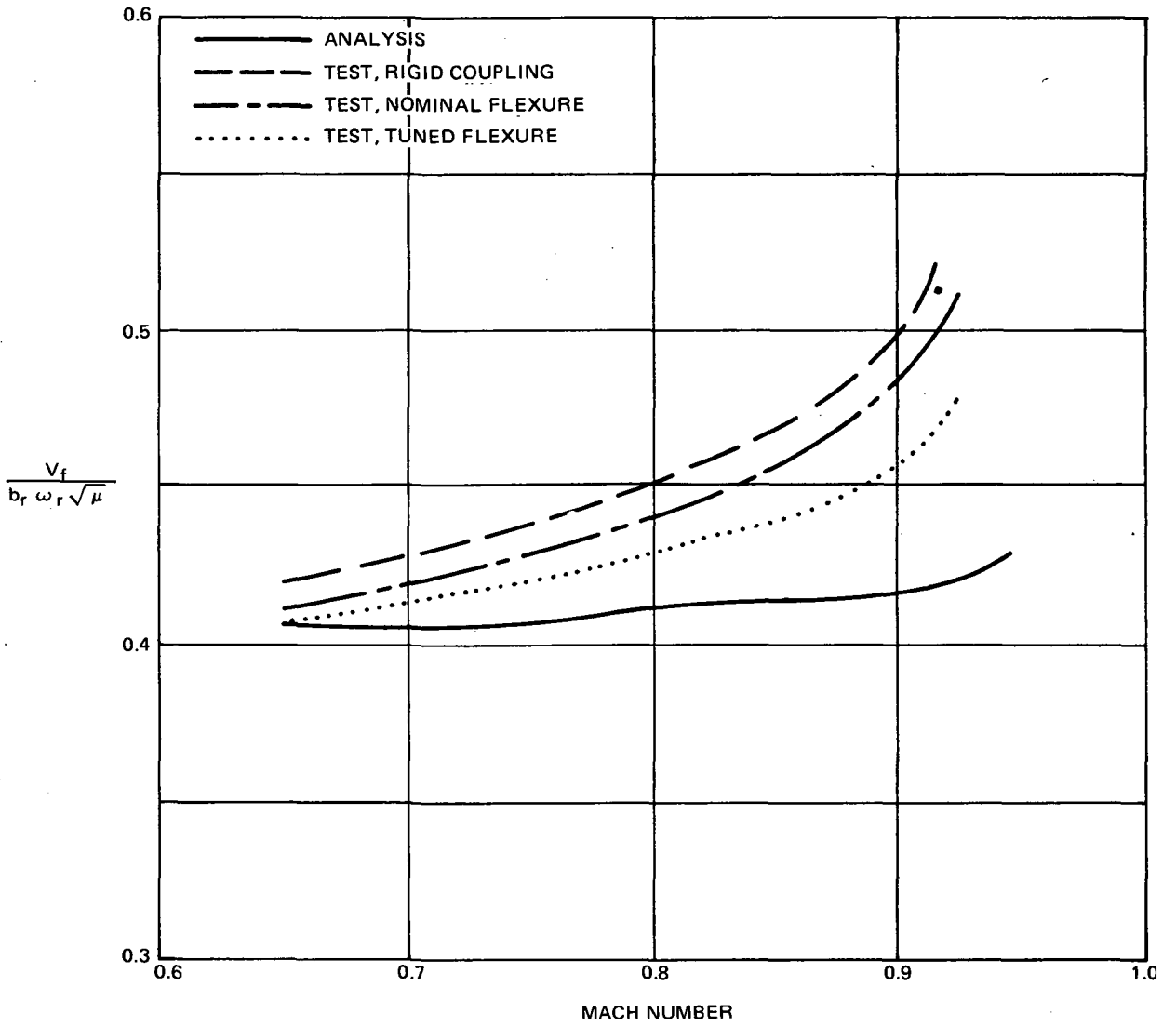
Figure 22.— Shuttle Flutter Speeds at σ = 3.0 for Various SRB Attachment Flexibilities

ANALYSIS

TEST

U_∞

$M = 0.6$
$\alpha = -3°$
$k = 0.0$
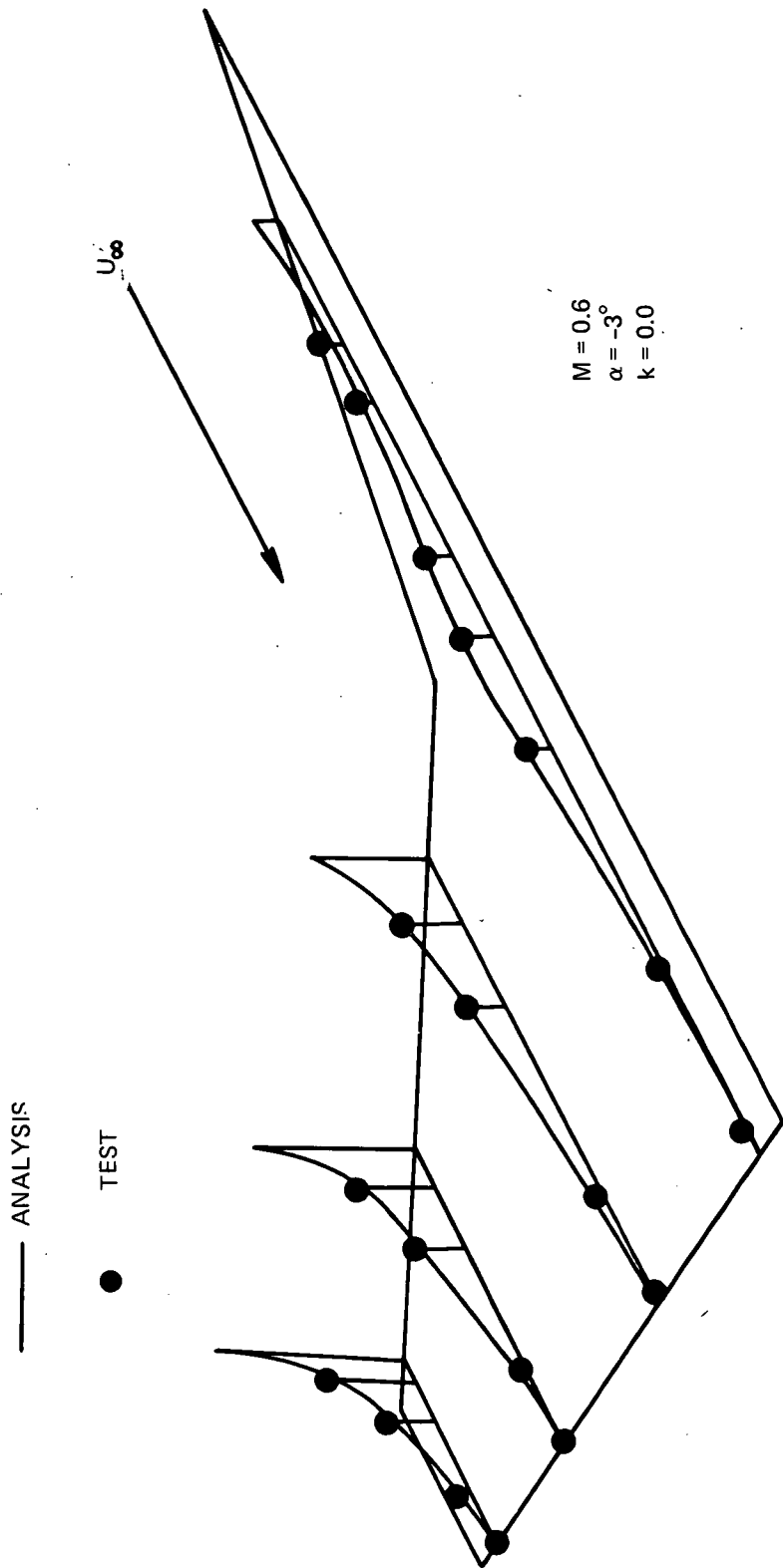
Figure 23.— Pressure Distribution on Isolated Orbiter Wing.
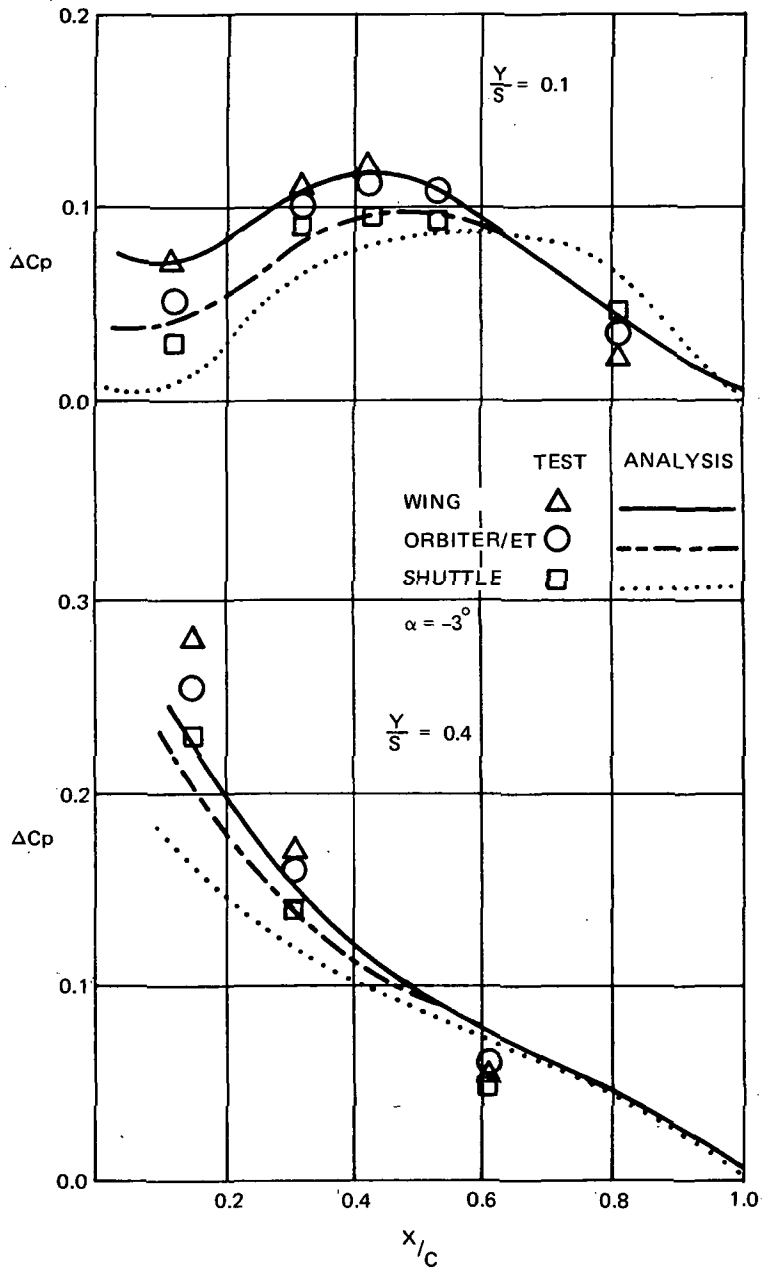
Figure 24.— **Steady State Pressure Distributions on the Inner Wing at M = 0.6**
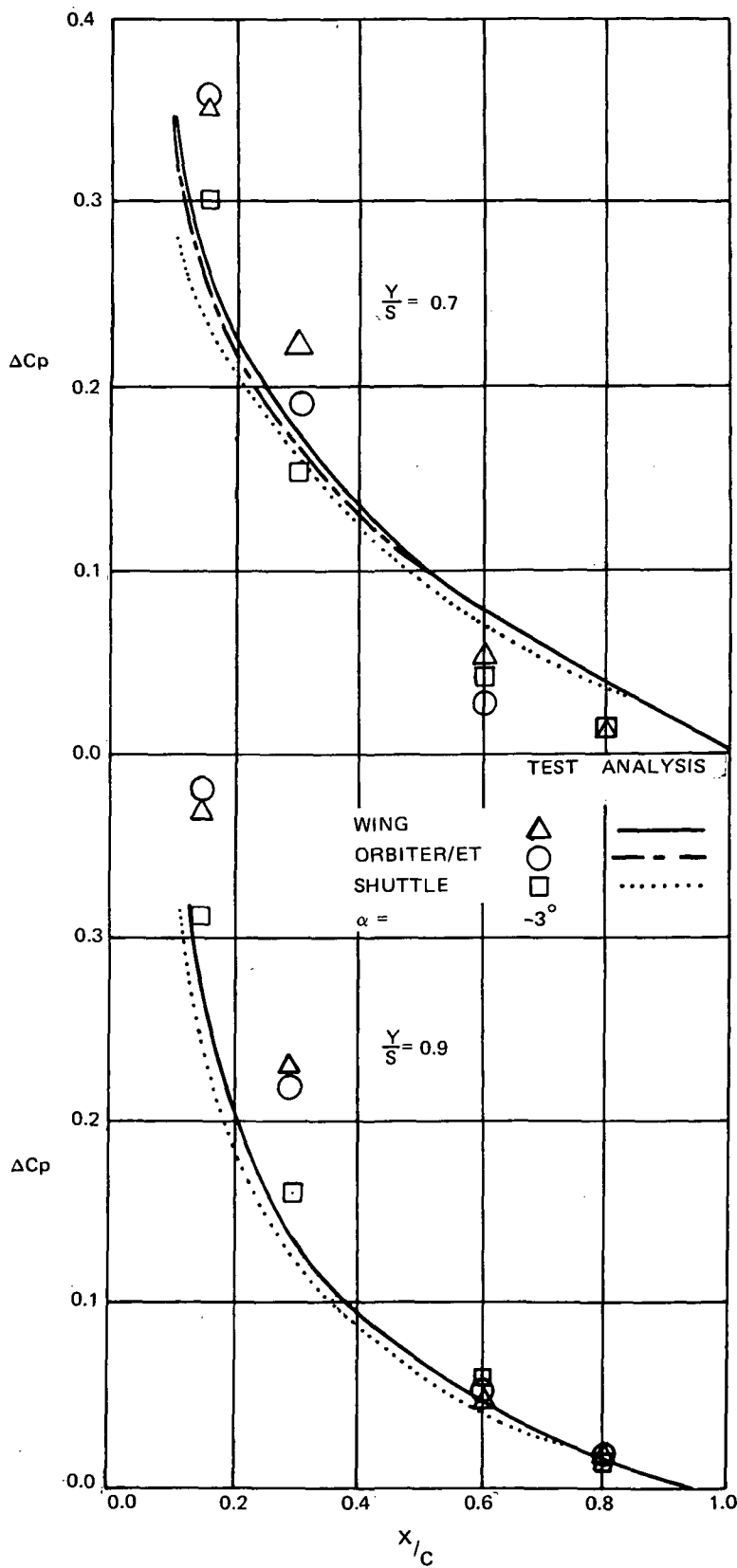
Figure 25.— Steady State Pressure Distributions on the Outer Wing
at M = 0.6
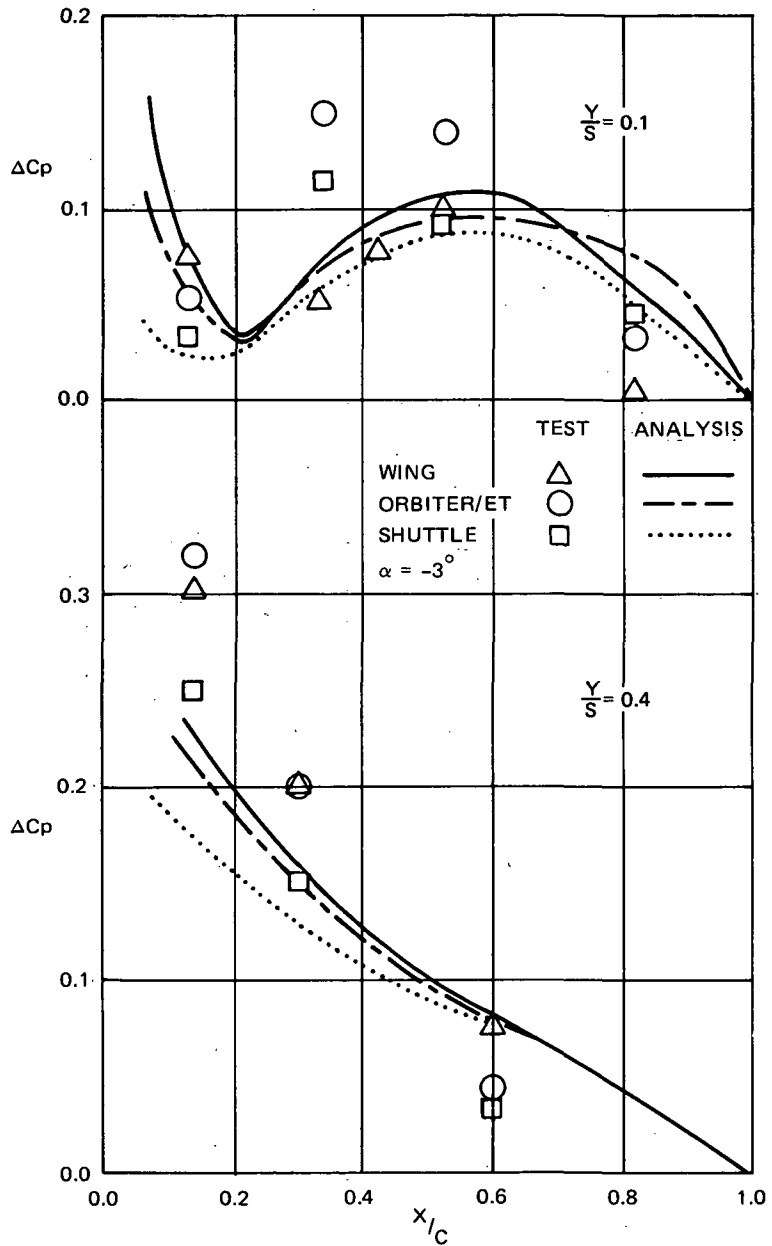
Figure 26.— Steady State Pressure Distributions on the Inner Wing
at M = 0.8
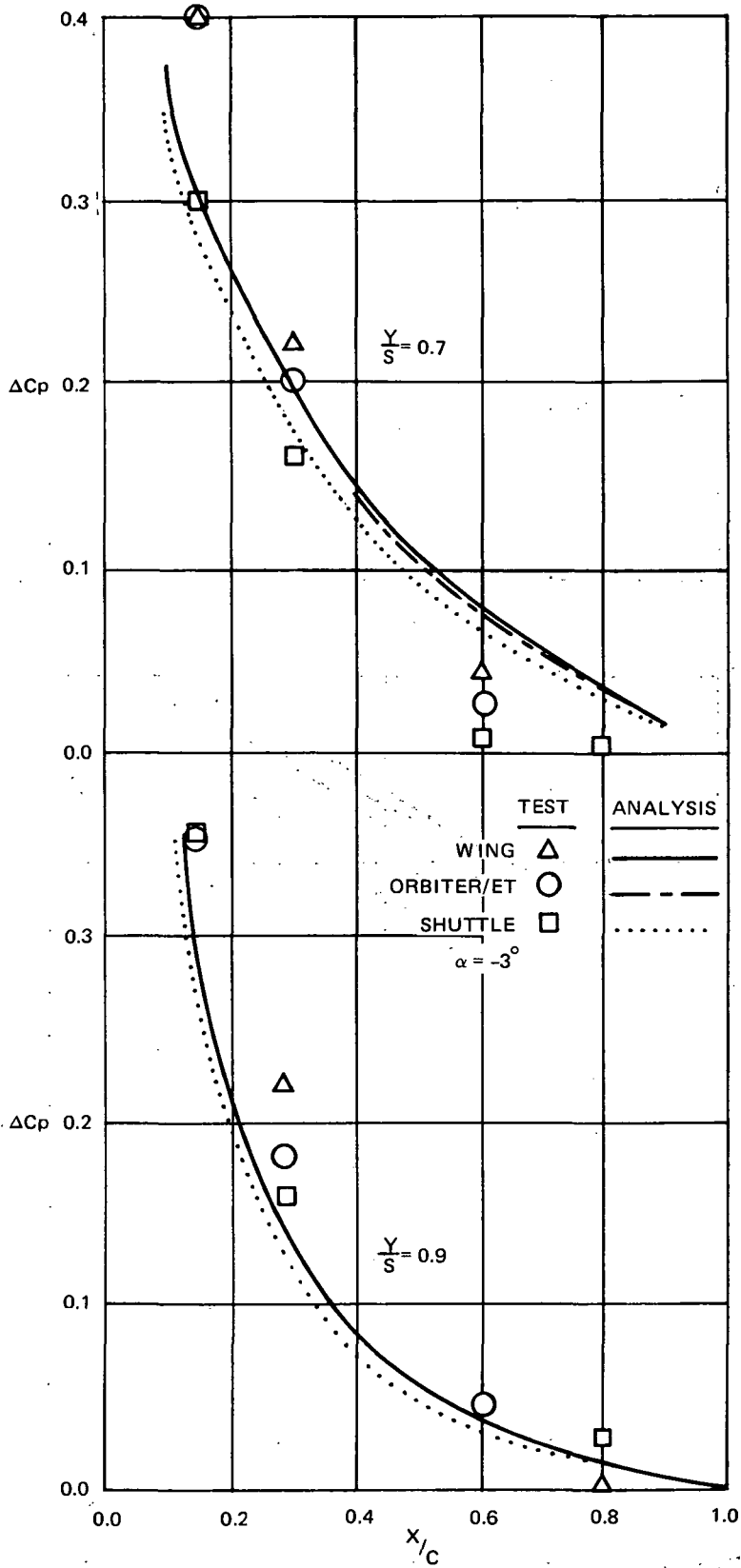
Figure 27.— Steady State Pressure Distributions on the Outer Wing at
M = 0.8
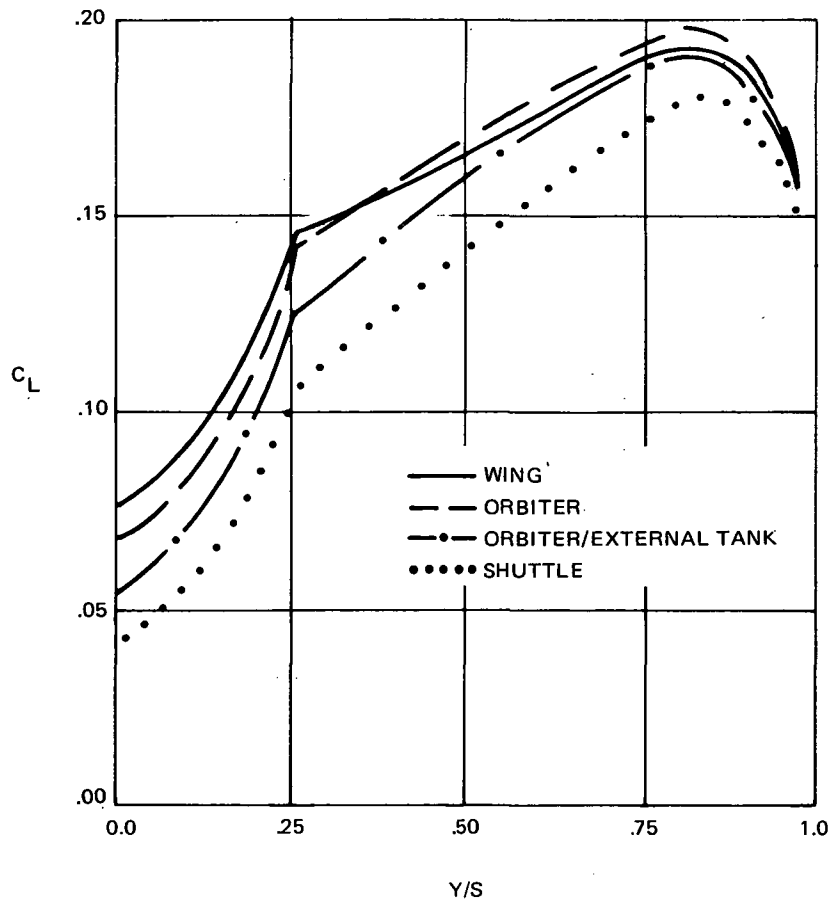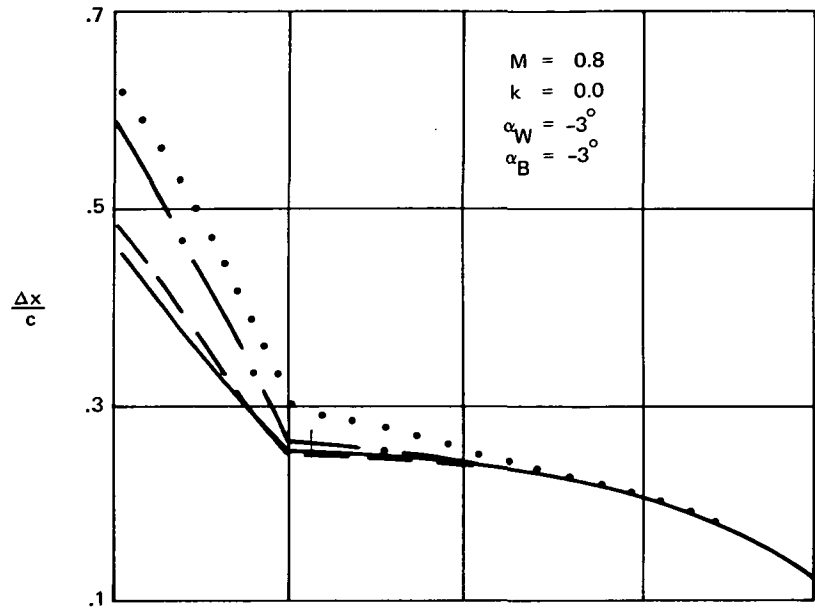
Figure 28.— Calculated Spanwise Loadings and Centers of Pressure for Various Shuttle Configurations at Angle of Incidence
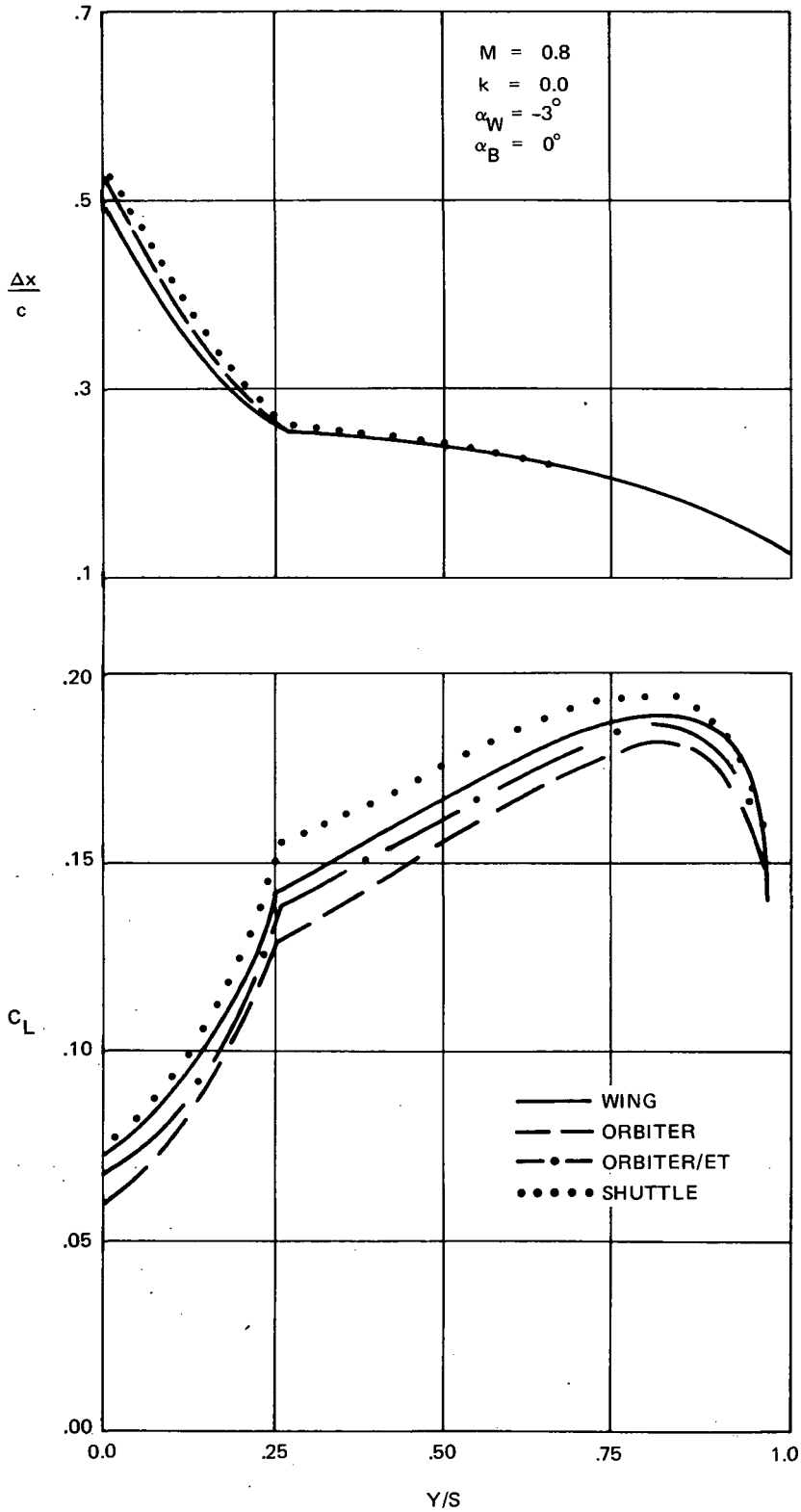
Figure 29.— Calculated Spanwise Loadings and Centers of Pressure for Various
Shuttle Configurations — Bodies at Zero Incidence
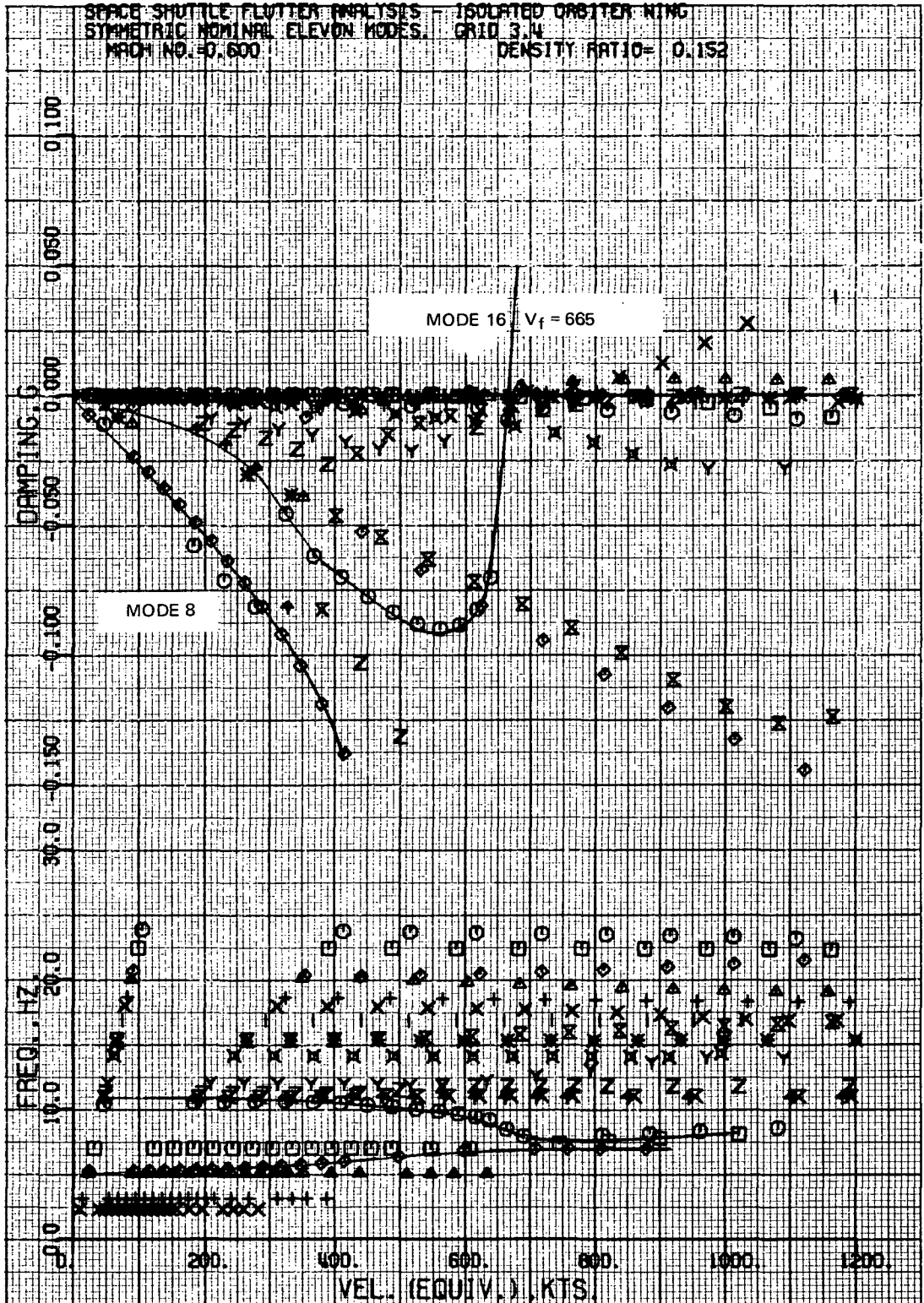
Figure 30.— Damping and Frequency as a Function of Airspeed for the Full-Scale Wing
Endplated at its Root.

70
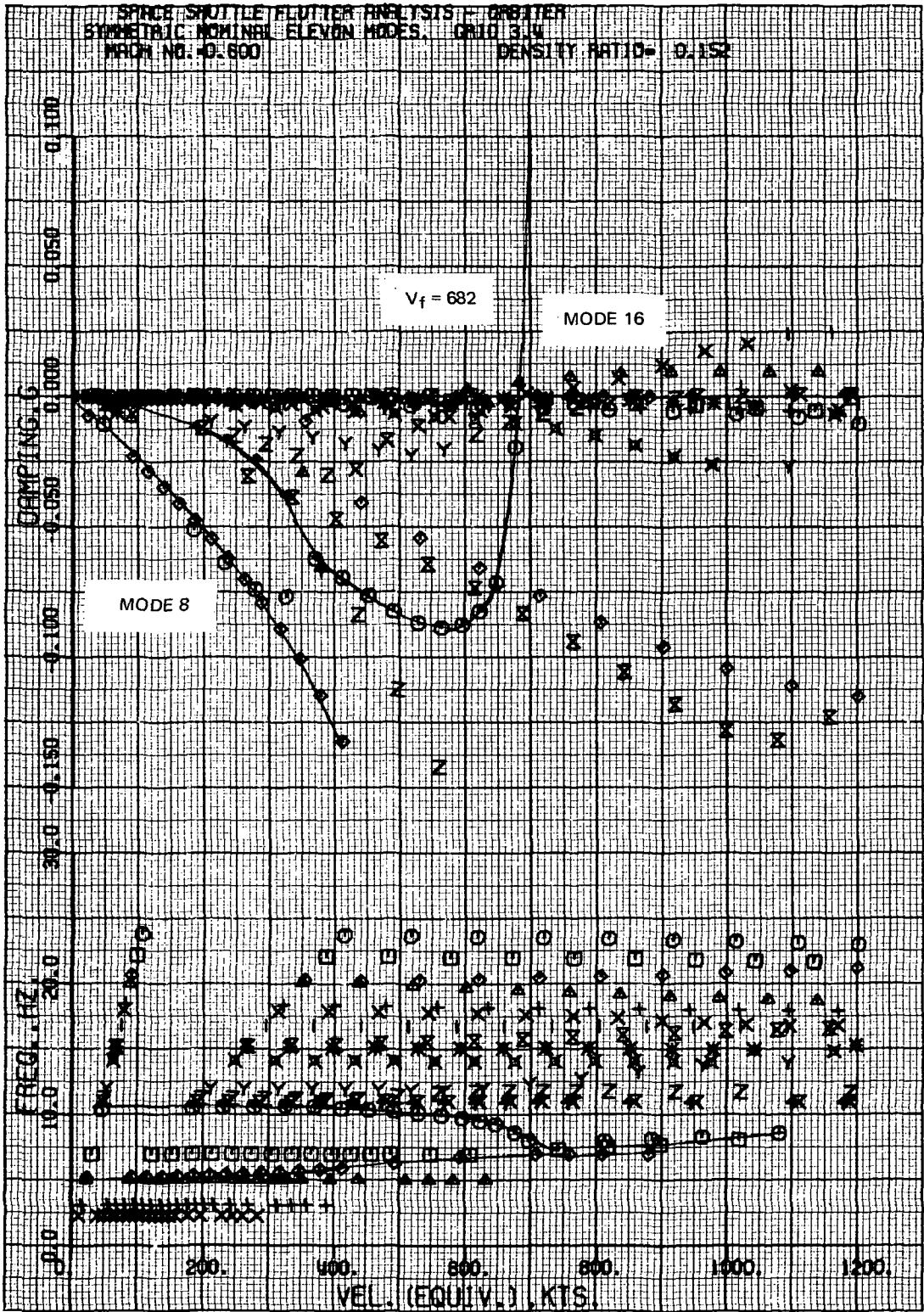
Figure 31.— Damping and Frequency as a Function of Airspeed for the Full-Scale Wing in the
Presence of the Orbiter Fuselage
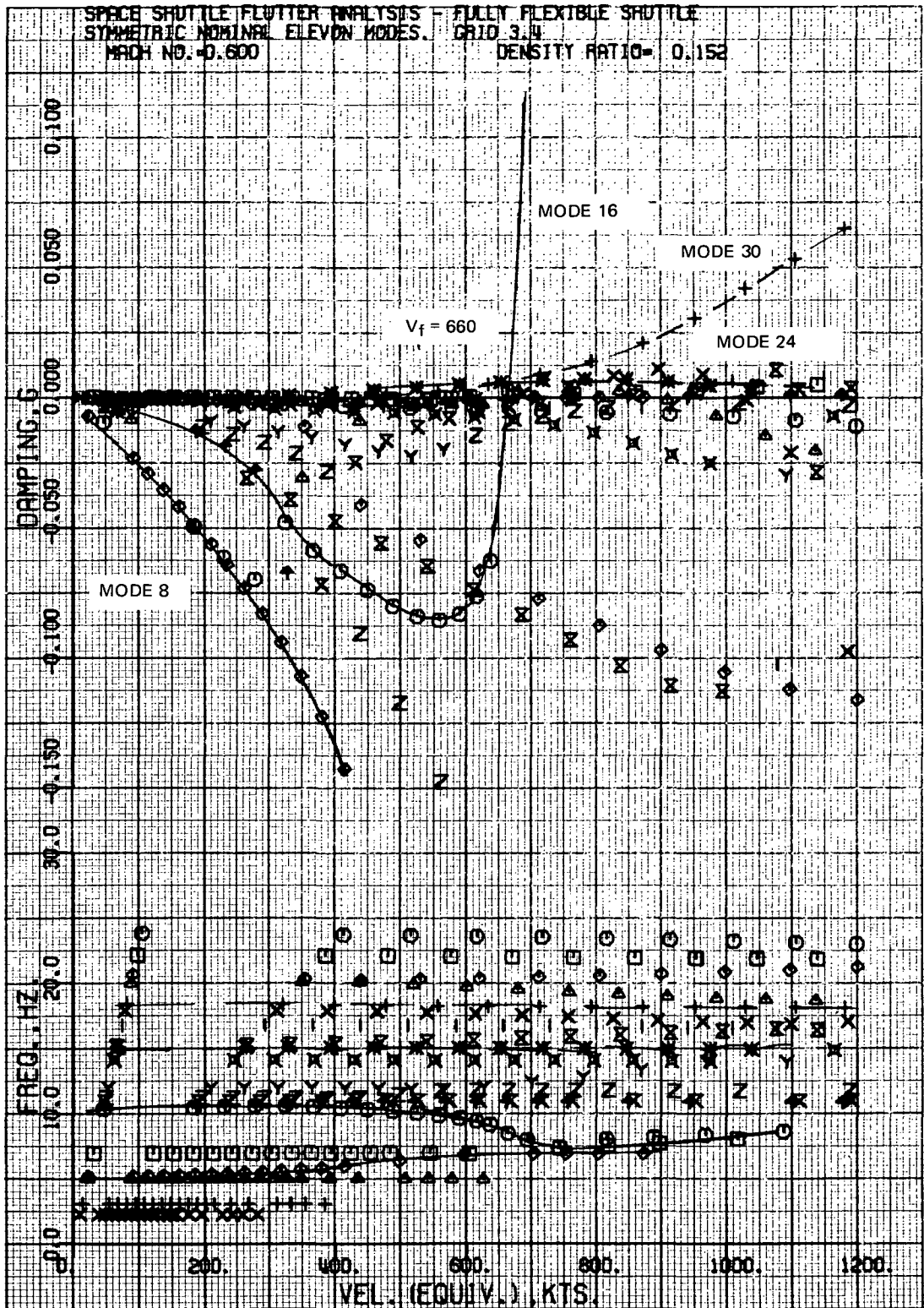
Figure 32.— Damping and Frequency as a Function of Airspeed for the Full-Scale Wing in the Presence of Other Shuttle Components (Fuselage, External Tank and Solid Rocket Booster)
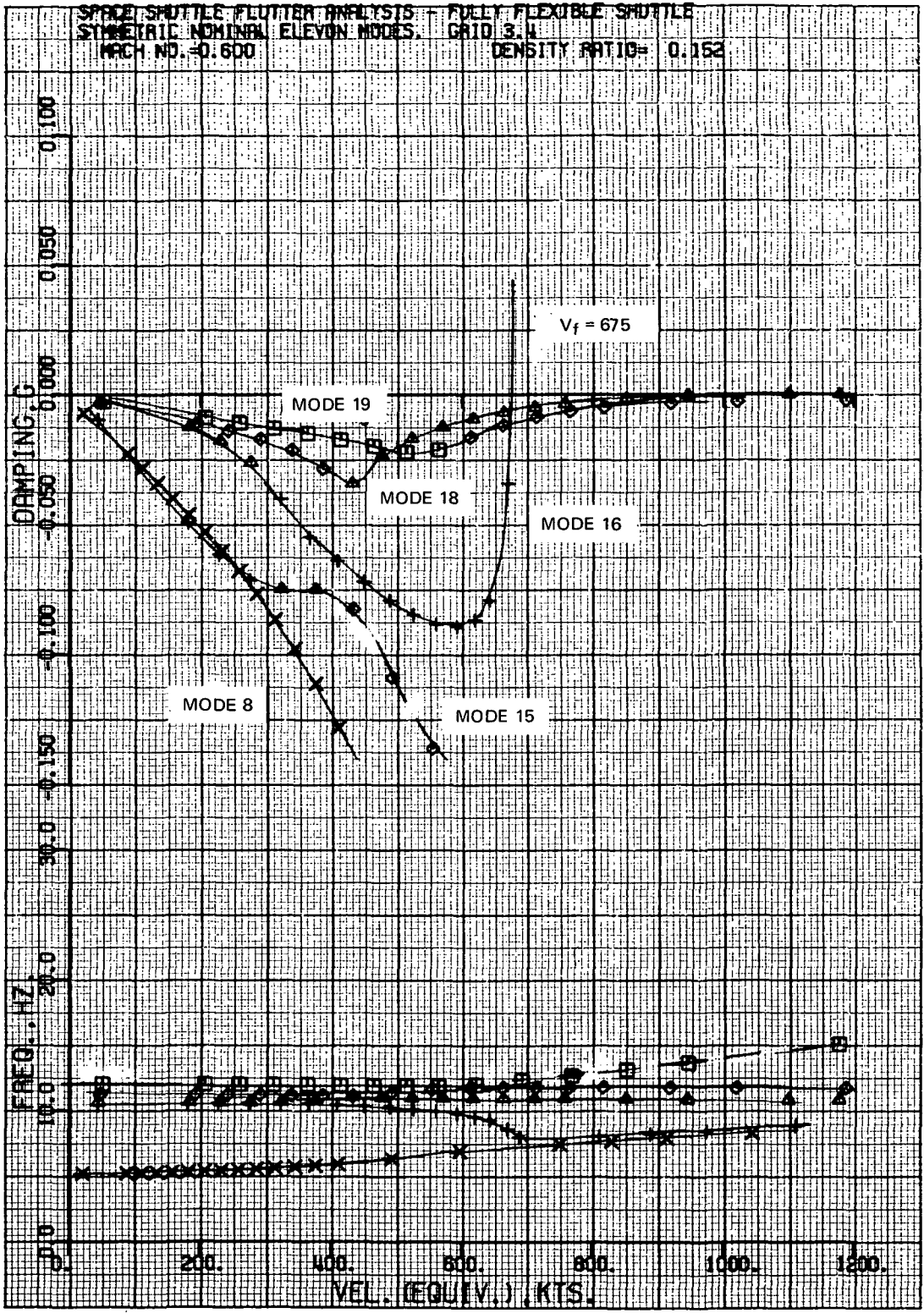
Figure 33.— Damping and Frequency as a Function of Airspeed for the Full-Scale Wing in the Presence of Other Shuttle Components (Fuselage, External Tank and Solid Rocket Booster). Only Five Modes Used

"The aeronautical and space activities of the United States shall be conducted so as to contribute . . . to the expansion of human knowledge of phenomena in the atmosphere and space. The Administration shall provide for the widest practicable and appropriate dissemination of information concerning its activities and the results thereof."
—NATIONAL AERONAUTICS AND SPACE ACT OF 1958

NASA SCIENTIFIC AND TECHNICAL PUBLICATIONS

TECHNICAL REPORTS: Scientific and technical information considered important, complete, and a lasting contribution to existing knowledge.

TECHNICAL NOTES: Information less broad in scope but nevertheless of importance as a contribution to existing knowledge.

TECHNICAL MEMORANDUMS: Information receiving limited distribution because of preliminary data, security classification, or other reasons. Also includes conference proceedings with either limited or unlimited distribution.

CONTRACTOR REPORTS: Scientific and technical information generated under a NASA contract or grant and considered an important contribution to existing knowledge.

TECHNICAL TRANSLATIONS: Information published in a foreign language considered to merit NASA distribution in English.

SPECIAL PUBLICATIONS: Information derived from or of value to NASA activities. Publications include final reports of major projects, monographs, data compilations, handbooks, sourcebooks, and special bibliographies.

TECHNOLOGY UTILIZATION PUBLICATIONS: Information on technology used by NASA that may be of particular interest in commercial and other non-aerospace applications. Publications include Tech Briefs, Technology Utilization Reports and Technology Surveys.

Details on the availability of these publications may be obtained from:

SCIENTIFIC AND TECHNICAL INFORMATION OFFICE

NATIONAL AERONAUTICS AND SPACE ADMINISTRATION

Washington, D.C. 20546